Experimental Analysis and Control of Recompression Homogeneous Charge Compression Ignition Combustion at the High Cyclic Variability Limit

by

Jacob William Larimore

A dissertation submitted in partial fulfillment
of the requirements for the degree of
Doctor of Philosophy
(Mechanical Engineering)
in The University of Michigan
2014

Doctoral Committee:
Professor Anna G. Stefanopoulou, Co-Chair
Erik Hellström, Ford Motor Company, Co-Chair
Professor André Boehman
Professor Jing Sun
Li Jiang, Robert Bosch LLC.

Dedicated to my family and friends who have never let me know anything less than never ending support.

Acknowledgments

This may be the shortest chapter in my thesis, but it is probably the most important in my opinion. There is no way I could have ever made it this far without so many people pushing me and offering me support.

First and foremost I must thank Professor Anna Stefanopoulou who not only provided me the opportunity and guidance to pursue and complete this degree but who has also given me support during the process which is above and beyond what I could have possibly expected. Despite her busy (insane) schedule, she has always made time to talk and help in any way she can. Even if it is from halfway around the world at times. Not to mention she somewhat tolerates my stubbornness from time to time.

Another huge thanks must be given to Dr. Erik Hellström. I don't think I have ever learned so much from someone in my life as I have from Erik. His willingness to help and teach is as unparalleled as his technical capabilities (and figure making prowess). I'm also happy to call him a friend. I would also like to thank my other committee members: Professor André Boehman, Professor Jing Sun and Dr. Li Jiang. I appreciate the time each one of you has spent to help me better my dissertation as well as teach me new things. A special thanks to Li who has worked with me on this project from the beginning and who has always been willing to lend a helping hand. And to Professor Boehman and Sun who taught me two of my favorite classes during my time at Michigan.

Perhaps the people who made this research most enjoyable are those that helped turn the crappy little room in the basement of the Auto Lab into a place that seemed only slightly better than a crappy little room in the basement of the Auto Lab. For all you guys in the PCL over the years, thank you. At the top of this list must be Shyam. I don't think the long hours at the dyno would have been the same without you around. I'm glad you were there to share the pain of experimental research and prototype engines with me! Shyam has always been my go to guy when I have questions about just about anything. He always seems to have the answers... even though most of the time he feeds me a line of sarcasm (read: crap) at the same time.

And then there is Pat, not only can I turn to pat for anything technical he is also my constant source of entertainment and my only use of Twitter. Even when things were crazy in the lab, Pat can always lighten the mood. I also have to thank the other guys in the PCL: Sando, Yi, and Mike, and the Autolab crew: Prasad, Vijay, Shrinath, Janardhan, Adam, Vas, Jason, and Stani. I must give a special thanks to Jason, thanks for getting fired up and coming to my side when I needed the help. Also the people at Bosch who got this project going and have helped me a lot over the years: Jeff, Julien, Jason, Nick, Oliver, and Hakan.

I have developed some great friendships with people all through college. Justin and Skyler, you guys made the weekends (and weeknights) a blast. I miss having you guys around, you should probably move back. And Brandon and Athena, I never get to see you anymore, but when we talk its like we saw each other yesterday, you all are great friends and I know we are going to be friends for life.

I have some of the best friends in the world back home. At the top of the list is Jeremy. I have known Jeremy forever, he is my best friend, my college roommate and probably the best person I know at motivating me to do things other than work. I think if we put together all the things we discuss over email and printed it out it would be about 20 times as thick as this dissertation. But it has been these discussions that have gotten me through a lot of rough times. He is always supportive of me, always there to listen, I only hope I can be half as good a friend to him as he has been to me. The same is true for Ciara and Logan. I can't tell you how much I look forward to seeing you guys every time we come back home, you all are the best friends I could hope for, thank you.

In addition to being one of my best friends, I don't think I would have been as successful at school or life as I have been without Matt Brown. I wish we could have kept track of how much time we spent together on all the late nights studying, class projects, mobile runs, working at the shop, traveling (the wrong direction through Memphis), saving the SoCo, the list goes on. Matt was there every step of the way through undergrad. I wouldn't have enjoyed it nearly as much with anyone else. Thanks Matt. I also want to thank Mr. Goodman. Of all the teachers I have had, none have influenced me as much as you have. Looking back on high school I didn't realize how special it was to have you around, how much you cared, and how much you sacrificed to help me out, teach me and prepare me for college and my career. Thank you.

And now my family. Mom and Dad, thank you is probably an insufficient phrase. You have sacrificed so much for me. When it came to anything that I needed to

succeed in life you never once hesitated to provide it for me. You have been there for everything, every football, basketball or baseball game, every Science Olympiad, every Quiz Bowl every moonbuggy trip, every concert, every band competition, the list goes on. You have always been my support, so instead of thank you, I'll just say I love you. And to Grandma and Grandpa, you have been there for me every step of the way as well. Grandma, you have always filled me with cookies and applesauce and applebutter to keep me going. Always encouraging me to push harder. Grandpa, I don't think I would be an engineer without your influence. I don't think I would love engineering as much as I do if it wasn't for building things in your garage or helping you fix the truck, or the computer or riding around in the Pontiac. You were the one who made me curious and always want to take things apart and learn. Thank you both, I love you.

And finally, my wife KiDahn. You are, without a doubt, my favorite part of life. I don't know what I would do with out you. You have been there with me every day of grad school, through all the crazy ups and downs. Throughout most of our relationship I have stayed out way too late to study and work, I always came to bed in the middle of the night, I'm was always too busy, always tired and you never complained. Instead you gave me support and encouragement. Through everything, you were my constant, the person I could turn to to make everything go away. I don't know what I did to deserve someone so special as you but I hope I can be as good of a husband to you as you have been a wife to me. I love you.

Table of Contents

List of Tables

Table

List of Figures

Figure

List of Appendices

Appendix

Abstract

The automotive industry currently faces many challenges pertaining to strict emissions and fuel consumption constraints for a sustainable society. These regulations have motivated the investigation of low temperature combustion modes such as homogeneous charge compression ignition (HCCI) as a potential solution to meet these demands. HCCI combustion is characterized by high efficiency and low engine-out emissions. However, this advanced combustion mode is limited in the speed-load operating space due to high pressure rise rates for increased loads. Often higher loads are run at later combustion phasings to reduce pressure rise rates, however high cyclic variability (CV) can also be a limiting factor for late combustion phasings. This work presents advancements in the understanding of high variability dynamics in recompression HCCI as well as methods for control of CV and load transitions which typically encounter regions of high variability.

Standard in-cylinder pressure based analysis methods are extended for use on high variability data. This includes a method of determining the trapped residual mass in real time. Determination of the residual mass is critical in recompression HCCI because of the combustion's sensitivity to the thermal energy contained within the residual charge. Trapping too much or little residuals can lead to ringing or misfires and CV, respectively.

Various levels of CV are studied using large experimental data sets to ensure statistical relevance. The cycle resolved analysis of this data has allowed for the development of a predictive model of the variability associated with lean late phasing combustion. This model is used to develop control which can suppress cyclic variability at steady state.

Knowledge about steady state control of CV and its oscillatory dynamics is further applied to the development of an adaptive controller. The adaptive controller uses a parameter estimation scheme in the feedforward component of a baseline midranging structure. The adaptive feedforward component enables the ability to correct for modeling errors and reduces parameterization effort. Experimental results demonstrate

that the control is effective at navigating through large load transients and avoids excess amounts of variability at both steady state and during the transition. Additionally, the actuators spend more time in a region of high authority when compared to non-adaptive control. This better prepares the controller for future transients.[1]

[1] mailto:larimore@umich.edu

Chapter 1

Introduction

1.1 Background

The increasingly stringent caps on internal combustion engine emissions as seen in Fig. 1.1 present many challenges to the automotive industry. Additionally, the ever increasing oil prices and the demand for more fuel efficient vehicles, as shown in [2] and Fig. 1.2, warrant the pursuit of alternative power sources and advanced combustion technologies. While there are many forms of alternative energy being researched which produce little to no emissions and do not use crude oil, their market penetration is slow. Also, they often cannot meet the full spectrum of demands from the current automotive consumer. Electric vehicles offer an enticing alternative, for instance, however their limited range restricts them to specific markets. Furthermore there is little infrastructure for support; significant upgrades to the electrical grid must be made to deal with the increase in electrical demand that would accompany them.

Replacing gasoline with other fuels, such as natural gas, is another alternative. There has been a significant increase in the production of natural gas in the United States due to newly discovered shale gas formations. The supply is substantial enough to provide fuel for a large portion of the United States energy demands, however there is once again little supporting infrastructure currently in place to deliver this to vehicles on the road.

One of the current trends in the automotive industry is downsizing and boosting with direct injection. Engines typically run more efficiently when operating close to peak power. Reducing the displacement of an engine (downsizing) for a given vehicle forces the engine to spend more time at higher relative loads [3, 4]. Additionally the engine can be augmented with a boosting device, usually a turbo charger or supercharger, which can allow the smaller engine to operate at an increased specific power. Turbo chargers have the added benefit of waste heat recovery.

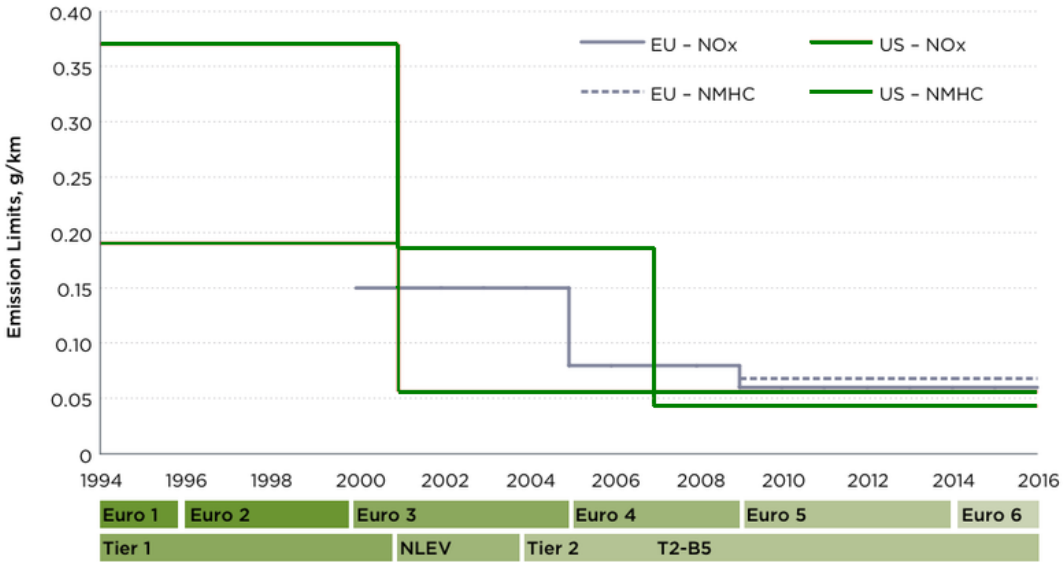

Figure 1.1: Progression of NO_x and particulate matter (PM) emissions for Europe and the United States, [1].

Technologies for improvement of fuel economy which are obtainable in the near term are essential for meeting targets as indicated by the CAFE standards in Fig. 1.2. The fleet fuel economy requirement across the globe are rising rapidly. One of the most promising prospects to meet these targets is the implementation of advanced low temperature combustion modes. Low temperature combustion offers lower emissions than typical spark ignited combustion because peak cylinder temperatures often do not reach the threshold required for NOx production. Additionally low temperature combustion modes often burn the fuel more quickly and uniformly resulting in higher combustion efficiencies and lower heat losses. Homogeneous charge compression ignition (HCCI) is one such low temperature combustion strategy. HCCI can achieve high thermal efficiency with low engine-out emissions [5, 6, 7, 8] and can be implemented into commercial vehicles [9].

1.1.1 Homogeneous Charge Compression Ignition Combustion

Homogeneous charge compression ignition (HCCI) is characterized by compression-driven near simultaneous auto-ignition events at multiple sites throughout a homogeneous mixture. Auto-ignition timing control in HCCI combustion requires careful

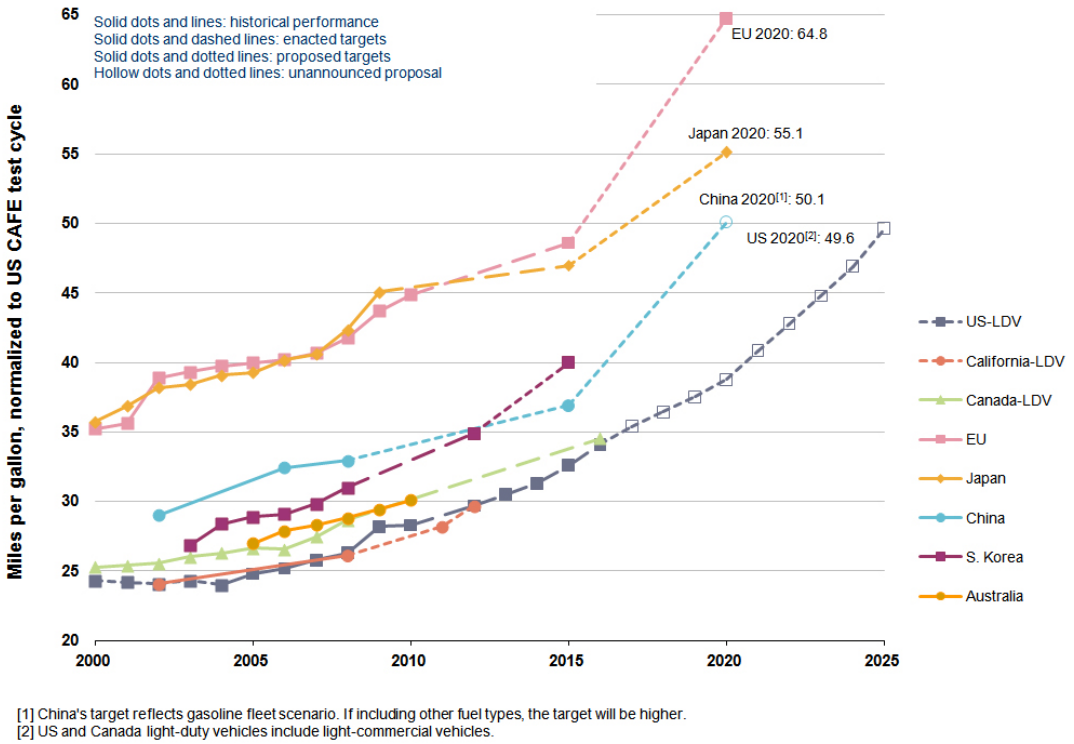

Figure 1.2: Comparison of projected and actual fuel economy targets for new vehicles throughout the world [2].

regulation of the temperature, pressure, and composition of the pre-combustion cylinder charge. This regulation of charge properties is carried out in recompression HCCI in part by retaining a large fraction of the post-combustion residual gases before they can be exhausted [10, 11]. Fuel injection timing, SOI, which is typically during the recompression period is another tool which can be utilized for charge preparation.

Challenges of HCCI Combustion

HCCI combustion is not without its challenges. It is limited at high loads and early combustion phasing by high pressure rise rates that accompany its near instantaneous auto-ignition. Additionally it can be difficult to control because it lacks a direct trigger to initiate the combustion such as the spark in spark ignited (SI) engines or the fuel injection in compression ignition (CI).

An example of the feasible operating region of HCCI is shown in Fig. 1.3. This data was obtained by finding an amount of NVO which yielded the highest range of SOI authority. At each load and NVO, SOI was swept from the ringing to the

CV limit. It is clear from this data that we face many limits in the load and combustion phasing space of HCCI. As we progress toward higher loads the combustion phasing must necessarily retard to avoid violation of pressure rise rate limits. Excessive pressure rise rates can lead to mechanical damage of the engine. Retarding the combustion allows more of the charge to burn later in the expansion processes which lowers peak pressures. However, retarding the combustion phasing too far can induce high cyclic variability because the combustion cannot be completed before the effect of expansion is dominant or the exhaust process begins. This can ultimately result in misfires and increased emissions. Misfires in HCCI can be difficult to predict and even more difficult to recover from as shown in [12, 13]. These instabilities at the edges of HCCI's operational limits make its effective operating region smaller and transients, such as large load transitions, difficult.

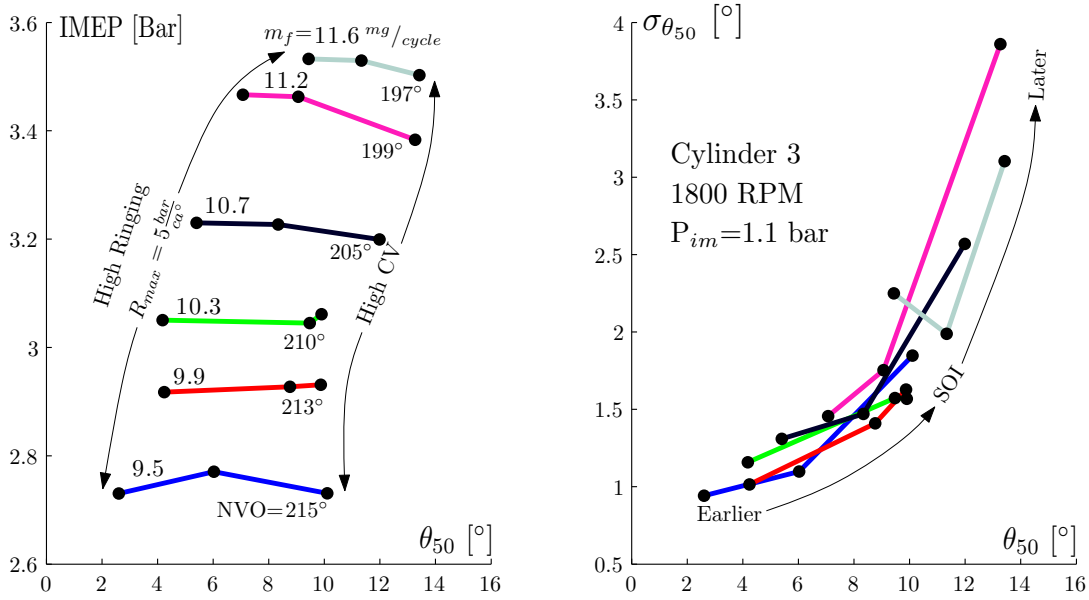

Figure 1.3: HCCI combustion is constrained by high pressure rise rates for early combustion and higher loads. Additionally, for late combustion, the phasing variability increases dramatically. Therefore HCCI combustion is limited in load because of an inability to mitigate high pressure rise rates.

Cyclic Variability in HCCI

Three modes of instability are examined in detail in this work: lean-late phasing, early phasing with thermal runaway and throttled stoichiometric HCCI. The variability of HCCI combustion, often called cyclic variability (CV), has been studied extensively

at various conditions. This is because these CV regions limit the operating space of HCCI and make transients difficult. Lean and late phasing combustion has been studied arguably the most because it places the largest restriction on the operating space, especially at low loads. The following is a short summary of advancements in the understanding of lean-late phasing combustion in HCCI. In [14], through simulations of a 1 state model, it was shown that there is a strong coupling of consecutive cycles due to recycled thermal energy. The important addition of the effects of recycled chemical energy were introduced through simulations of chemical kinetics with 31 species in [15] and reduced to an eight state model in [16]. A control oriented, 4 state, model was developed in [17] where fuel was one of the states. Experiments for lean HCCI were studied and modeled with two states in [18, 19].

The stoichiometric late phasing limit has been observed in the transition from SI to HCCI in [20, 21, 22]. It will be shown that the dynamic coupling appears to be different for lean versus stoichiometric HCCI. The unburned fuel mass that couples the cycle-to-cycle behavior is quantified in [23] which shed light on the chemical energy coupling and the dynamical patterns emerging at the limits of spark assisted HCCI stability region. Distinct patterns in combustion efficiency versus phasing provide a key non-linear characteristic that distinguishes cyclic variability at the lean and stoichiometric spark-assisted limit, [24]. Additionally it yields insights as to the contribution of spark.

Control of HCCI

The lack of a direct trigger to initiate combustion in HCCI makes the problem of closed loop control an interesting and challenging topic. The ignition timing is insensitive to spark timing due to the highly dilute nature of the charge and so proper charge preparation is imperative to avoid hitting the limits described in the previous sections. For these reasons there are typically only a handful of actuators available to control HCCI. Since HCCI is usually run lean, mass of fuel is directly correlated to the load. The load however dictates the trapped residual charge and consequently the phasing. There is a narrowly acceptable region of combustion phasings for any given load, much smaller than in SI combustion, as we observed in the previous section. Combustion phasing is usually controlled through a combination of the valve and fuel injection timing. The valve timing controls the amount of residual mass trapped. The injection timing controls the amount of fuel mixing and reformation which occurs during the recompression region. Control similar to this has been used

in [25, 26, 27, 28, 29] in both simulation and experiments. Alternatively the timing can be controlled through intake air heating as was done in [30] where duel fuel operation was studied. The use of knock sensors as a means of combustion phasing feedback to regulate phasing was explored in [31] and external EGR as a means of control was demonstrated in [32].

Model-based control of HCCI combustion has also shown good results to improve transients. This requires the development of accurate control-oriented models that can be run in real-time on embedded control hardware. Examples of HCCI control-oriented models can be found in literature [33, 34, 35, 36, 37, 38, 39]. The combustion phasing prediction accuracy of these models is especially crucial when they are used in model-based predictive control strategies, for example [39, 40, 41, 42] so that operating region constraints are not violated. The work presented here will use a model-based midranging control architecture to navigate load transients.

Midranging control is a method used primarily in process control applications [43, 44], however it has been utilized successfully for combustion control where similar coarse and fine trim actuators are often available, [45, 46]. The midranging controller uses model-based feedforward to help speed up load transitions and better regulate combustion phasing. This has been demonstrated for a multicylinder HCCI engine in [38, 39, 47].

Another method of control used to prevent misfires and CV involves slowing down the transient in a manner which prevents actuator saturation. This is commonly referred to as a reference governor [48, 49, 50, 51, 52, 53, 54]. This concept has been applied to engine and gas turbine control in [55, 56, 57] and to HCCI combustion on a multicylinder engine in [39, 47, 58].

1.2 Dissertation Contributions

This dissertation is comprised of three main topics which present novel contributions to the field of HCCI combustion analysis and control. The first key element is a method of determining the trapped residual mass in a recompression HCCI engine which is capable of being implemented online. Knowledge of the trapped residual mass is helpful for understanding HCCI dynamics. However there does not exist an effective way to measure this quantity in real time.

The second focal point of the dissertation is a study of the dynamics associated with various modes of cyclic variability in HCCI combustion. These experimental

results are used to develop a model of lean late phasing combustion. Additionally, experimental results are provided which show effective reduction of cyclic variability using model based control.

Finally, a method of implementing an adaptive parameter estimation scheme in the model presented in [38, 39]. The model requires time intensive and non-trivial parameterization which is eased by the use of the adaptive estimation. The adaptive model is ultimately used to modify the feedforward component of the controller from [38, 39, 47] to regulate combustion phasing during load transitions. The contributions of the dissertation are summarized in the following:

1. Online Residual Mass Estimation:
   The algorithm is developed from mass and energy balance equations and is of sufficient simplicity to run in real-time on embedded control hardware. Real-time estimation of residual gas fraction for use on data with high cyclic variability has not been demonstrated previously in literature. Analysis of the algorithm is presented and demonstrates stability and convergence. Experimental results show the equation's performance for various actuator conditions and steps. Additionally the transient ability of the approach is tested for high CV data.
2. Cyclic Variability Analysis, Modeling and Control:
   Experiments are performed to study the dynamics of HCCI combustion at the limits of stability. Specifically three modes are explored: Throttled Stoichiometric, Thermal Runaway and Lean-Late Phasing combustion. Using insights from the experimental results a model is developed for lean-late phasing combustion. This model is validated against experimental results and is used to develop controllers to suppress the observed variability. It is demonstrated experimentally that simple control can effectively reduce the variability while maintaining a late combustion phasing.
3. Adaptive Model and Control:
   Adaptive parameter estimation is used to modify model-based feedforward control in an effort to mitigate modeling errors and increase control accuracy. In-cylinder pressure measurements are used to calculated combustion phasing which is compared with the prediction of an online non-linear engine model to drive the parameter estimation. The controller is evaluated for internal stability through analytical analysis and simulations and it is demonstrated through experiments that a single adaptive parameter can reduce parameterization effort. The adaptive control allows load transitions to be performed while maintaining the actuators in a region of high authority.

The work presented in this dissertation was performed as part of the ACCESS (Advanced Combustion Concepts – Enabling Systems and Solutions) project. The project, funded in part by the Department of Energy, was intended to develop methods and control strategies to enable the use of advanced combustion modes in

light-duty vehicles. Specifically to aid in the implementation of multiple combustion modes into a single engine configuration. The target of the project was to develop a downsized, multi-mode, turbocharged gasoline engine which demonstrates a 25% reduction in fuel consumption while meeting super ultra low emissions vehicle (SULEV) emissions requirements and maintaining baseline performance.

1.3 Chapter Descriptions

In Chapter 2 the experimental setup is presented. Additionally a description of the control actuators available for use is provided and a description of performance metrics. Chapter 3 introduces methods to modify in-cylinder pressure analysis tools such that they can be used on a cycle-by-cycle basis to study transients and highly variable data. This includes air mass determination, residual mass estimation, heat release analysis, combustion efficiency, residual fuel mass and combustion phasing.

Chapter 4 presents a method of determining the trapped residual mass in real time. A dynamic analysis of the resulting equation is provided which demonstrates its stability, convergence and sensitivity properties. Experimental results show how the equation performs online for various operating conditions and actuator steps. The residual estimation is also run on highly variable data to show its capabilities to deal with cyclic variations.

In Chapter 5, the analysis techniques provided in Chapter 3 are applied to data at the operational limits of HCCI combustion. Specifically, the onset of instability is observed through large data sets at three dynamically different operating conditions. Observing the CV for long periods allows one to study the statistical properties of the combustion in detail and understand the important dynamics more clearly. The experiments here contain an order of magnitude more cycles than is typically observed in literature. A model for late phasing CV is also presented. In Chapter 6 two different controllers are developed based on the model from Chapter 5. These controllers are implemented on the engine and tested in real time. The result of their effectiveness is demonstrated.

Chapter 7 employs the residual estimation technique from Chapter 4 as an additional state for a control oriented combustion model. It is augmented with an adaptive parameter estimation scheme to continuously improve model prediction and make the system more robust to disturbances and modeling errors. Chapter 8 uses this adaptive technique to modify the feedforward component of a mid-ranging controller in

real-time. An analysis of the controller is performed analytically and in simulation to show internal stability. Experiments are performed to demonstrate the adaptive control's ability to regulate combustion phasing during load transitions. Improvements in the control are observed over the non-adaptive case. The adaptive control is more effective at keeping the actuators in their region of greatest authority. Finally Chapter 9 presents conclusions and guidelines for possible future work. A flow diagram of the dissertation is provided in Fig. 1.4.

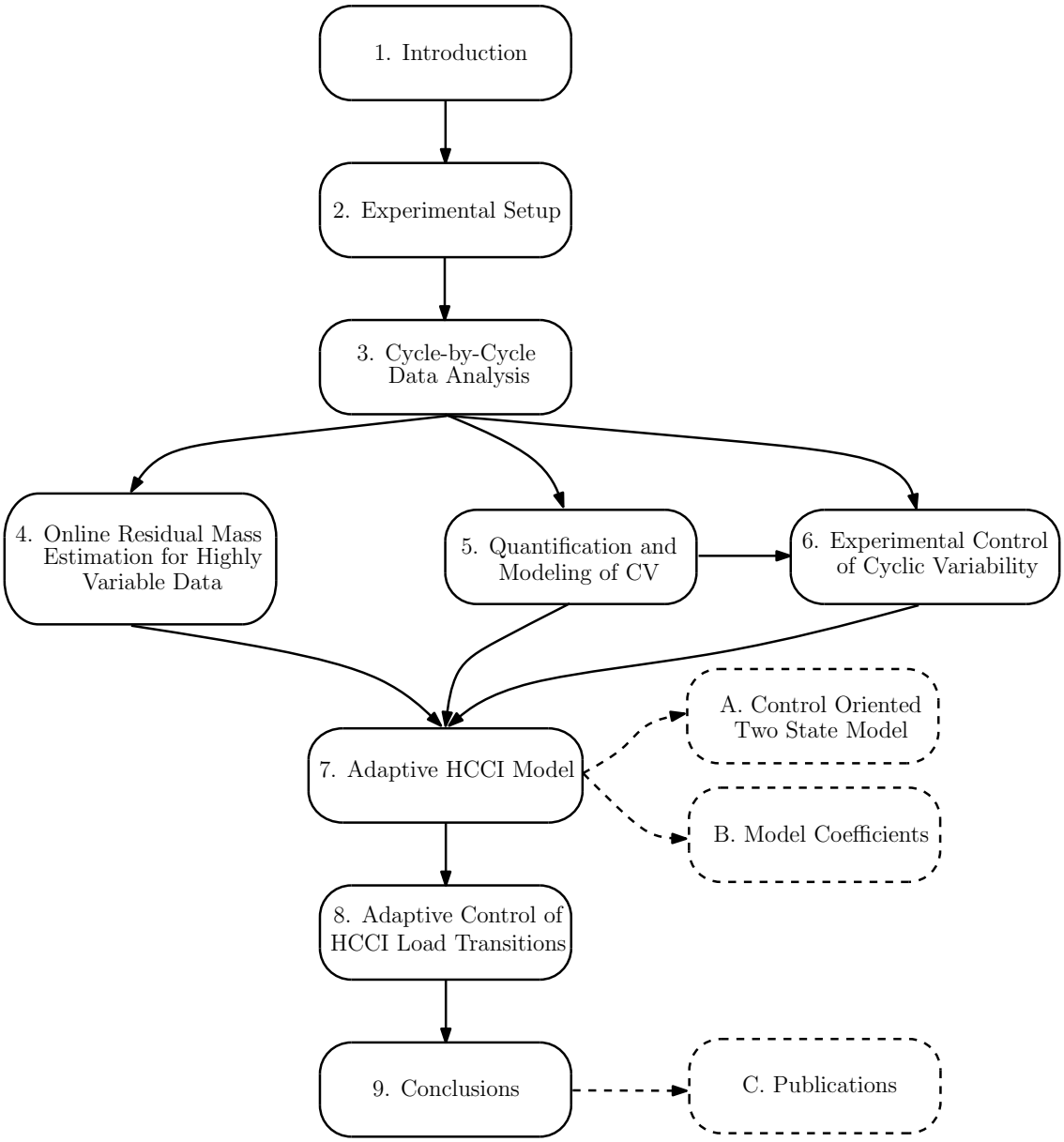

Figure 1.4: Flow diagram of the dissertation. Lines indicate how chapters are connected. Dotted lines indicate appendices.

Chapter 2

Experimental Setup

Auto-ignition of a homogeneous mixture of gasoline and air is not easily achieved in a normal normal gasoline direct injection engine. This is because HCCI combustion is a thermally dominated chemical kinetic process [59]. As such, it is necessary to raise the thermal energy of the charge such that autoignition can be realized near top dead center (TDC). There are several methods available to do this including intake air heating [7], increased or variable compression ratio [60, 61], lower octane fuel or trapping hot residual charge mass in the cylinder, to name a few.

This work uses the combination of a recompression HCCI engine and increased compression ratio to achieve high levels of dilution and the thermal energy necessary for HCCI combustion. The availability of variable valve timing and lift valve trains enables recompression as an effective strategy to quickly regulate the pre-combustion charge temperature and composition in a reciprocating engine [11, 62]. It is achieved by an early exhaust valve closing (EVC) and a late intake valve opening (IVO) when compared to the valve timings of a typical spark ignited engine (SI) engine. The result is a period of the cycle referred to as negative valve overlap (NVO) which can be seen in the typical recompression HCCI in-cylinder pressure trace in Fig. 2.1 as the second pressure rise. Because the exhaust valve is closed early a large fraction of the exhaust gases are trapped in the cylinder for the next cycle. The gases are hot and have a profound impact on the charge temperature and composition in the subsequent cycle. Additionally, the NVO region enables the use of direct fuel injection as an actuator suitable for cycle-by-cycle control. The hot residual gases trapped in NVO work as a catalyst for fuel break down. Injecting the fuel earlier or later in the NVO region can make the charge auto-ignite earlier or later, respectively.

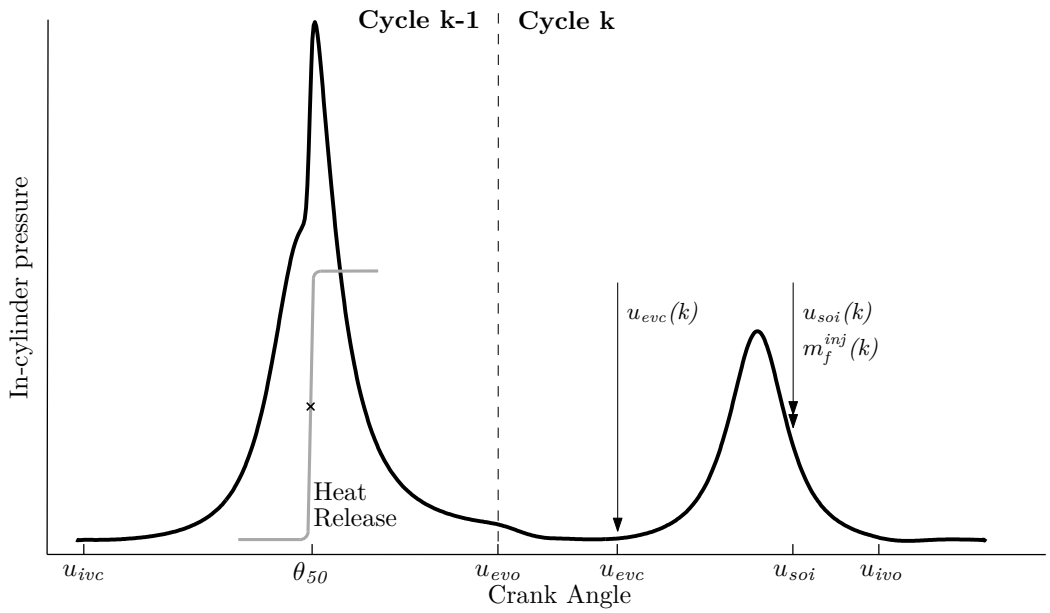

Figure 2.1: Typical in-cylinder pressure trace for a recompression HCCI engine. The control inputs are shown along with the cycle definition which are described in detail in Sec. 2.2.

2.1 Experimental Setup

A four cylinder 2 Liter GM LNF Ecotec engine with direct injection is used as the baseline platform, Fig. 2.2. Premium grade indolene was used for all tests. To accommodate HCCI combustion the compression ratio was raised to 11.25:1 and camshafts with shorter duration and lower lift were used to allow for unthrottled operation. A small supercharger (Eaton M24) was added to the air path in series with the stock turbocharger to provide additional boosting capabilities at low loads. Engine coolant temperature was controlled to a set-point of 90°C for all tests. The spark was left on, but at a position of 40° after top dead center for most experiments. When the mixture is lean and highly diluted with residuals the spark will have little influence on the combustion, having the spark on late only helps to prevent the spark plug from fouling. The only tests where spark was utilized in this work is in Chapter 5 where a study of the cyclic variability associated with throttled stoichiometric combustion is presented.

Cylinder pressures were sampled at a resolution of 0.1° cad for offline pressure analysis, however real-time estimation of combustion features were done at a resolution of 1° cad. The combustion phasing used in feedback and for the adaptive algorithm, Chapters 7 and 8, was estimated with a Bosch Motronic MED 17 engine control unit (ECU). The control strategies were implemented using a combination

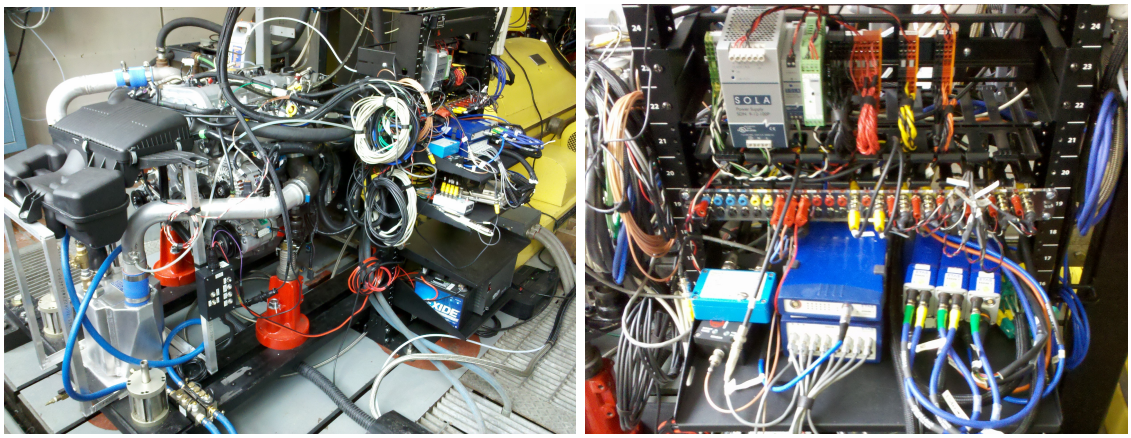

Figure 2.2: Multicylinder recompression HCCI engine used for testing along with all rapid prototyping hardware and instrumentation.

of C and Matlab code, and were tested in real-time using an ETAS ES910 rapid prototyping module. The module uses an 800 MHz Freescale™ PowerQUICC III MPC8548 processor with double precision floating point arithmetic and 512 MB of RAM. A diagram of the rapid prototyping hardware, engine and software interfacing is provided in Fig. 2.3.

2.2 Performance Outputs

Due to HCCI's sensitivity to high CV and its tendency to push the mechanical limit of an engine due to high pressure rise rates, one of the most important performance outputs is the combustion phasing. This is referred to as θ_{50} and is quantified by the crank angle degree associated with 50% of the charge burned. The determination of this value is relatively insensitive to disturbances and errors because it is typically associated with the highest burn rates during combustion. Therefore it is a reliable metric for HCCI combustion. Combustion phasing determined from a gross heat release analysis is typically computed offline. However, fast methods have been developed which require little computation power or memory and are capable of running online [63].

Engine torque is another important output, here this will be referred to as the net indicated mean effective pressure (IMEP). This is the total pressure-volume work integrated over an engine cycle (720°) and nomalized by the displacement volume. The net IMEP is defined as:

$$\text{IMEP} = \oint P \frac{dV}{V_d} \tag{2.1}$$

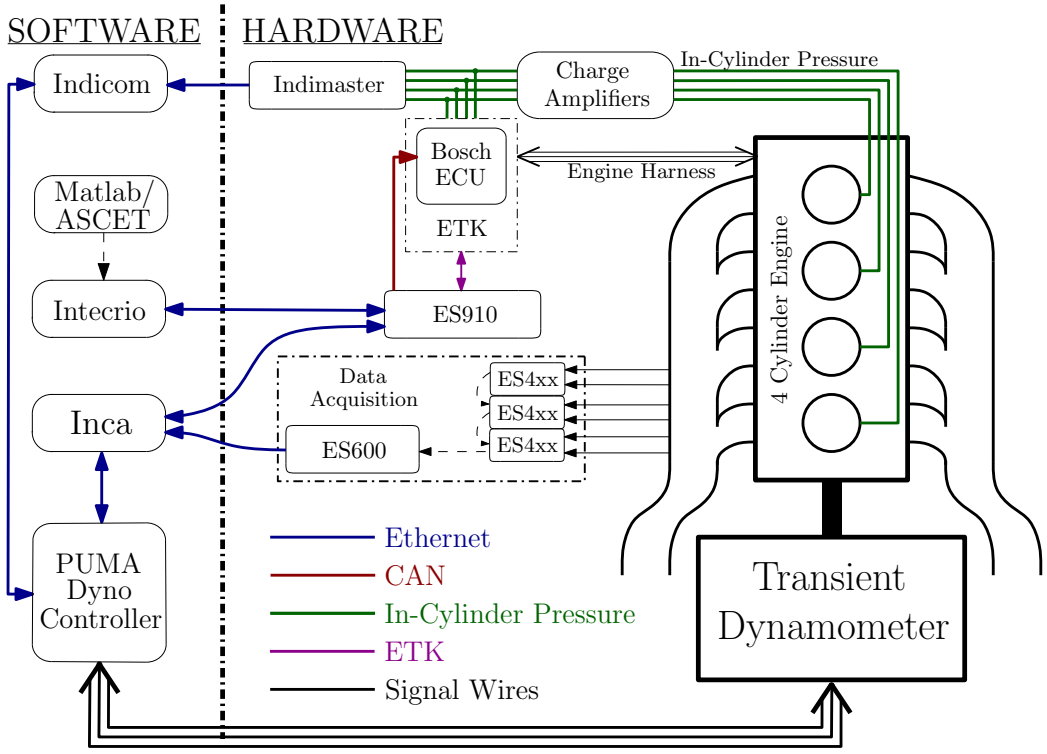

Figure 2.3: Hardware/software interfacing for experimental setup.

where P is the incylinder pressure, V is the in-cylinder volume and V_d is the displacement volume.

2.3 Control Actuators

As indicated in Fig. 2.1, there are three main actuators available for control. The exhaust valve closing time, the fuel injection timing and the mass of injected fuel (u_{evc}, u_{soi} and m_f^{inj} respectively). Each actuator has pros and cons associated with it, whether it be detrimental effects on performance or limitations on authority and speed. For instance, injection timing provides a fast method of controlling combustion phasing, however injecting too early can increase pumping work. It is necessary to understand all of these limitations and use the actuators in unison to accomplish HCCI control.

2.3.1 Valve Timing

The valve train uses cam shafts and phasers to actuate the valves. For these reasons it is not fully flexible, lift and duration are constant. However the hydraulic phasers allow for control of the timing and therefore the retention of trapped residual gas by increasing or decreasing the NVO recompression region. The valve timing can have significant authority over the combustion phasing, however the phasers are slow (approximately 100° per second) and the timing is the same for all 4 cylinders. Therefore, the valve timing cannot be used for control on a cycle-by-cycle basis or cylinder-to-cylinder. Its main purpose is for large transients, moving from one operating condition to another.

2.3.2 Injection Timing

The recompression period provides a time for the injection of fuel, u_{soi}. Injecting during the recompression period allows for significant mixing time and the formation of a homogeneous mixture. Injecting in NVO has complex thermal and chemical effects [64]. Large fuel molecules may breakdown into smaller chains which permit easier auto-ignition through the formation of radicals. These reactions may even lead to heat release and pyrolysis. Ultimately, earlier injection produces earlier auto-ignition. The timing of the injection can be changed on a per-cycle basis, it is therefore a good candidate for a control actuator [37]. The actuator is limited in authority however, its effect of combustion phasing saturates for very early and very late injections. Additionally, too early of an injection can cause ringing depending on the operating condition. It can also have a negative effect on the pumping work and emissions [65]. The fuel injection timing can be controlled on a cylinder-to-cylinder and cycle-to-cycle basis, it is very useful for fast, but small, load transitions and cylinder-to-cylinder balancing.

2.3.3 Fuel Quantity

The quantity of fuel injected in HCCI is used primarily to control the load. This is contrary to SI engines where it is used to regulate the air-fuel ratio to stoichiometric conditions. HCCI is not required to run at stoichiometry because its peak combustion temperatures are typically below the threshold for NO_x production. Additionally, the mass of fuel can have a large impact on the combustion phasing. Increasing the load

increases the temperature of the trapped residual gases which can lead to earlier auto-ignition if not compensated for using the previously described actuators. The mass of fuel can be controlled on a cylinder and cycle basis, making it useful for transients.

2.3.4 Other Actuators

Additional inputs include the intake valve timing, supercharger by-pass valve, spark timing and the engine speed. The intake cam timing is coupled strongly to the air flow into the cylinder. It is usually desired to optimize the air flow in an engine, the timing is therefore fixed at a position given by a supervisory controller based on engine speed and load. The supercharger bypass was used to regulate the intake manifold pressure. It was adjust to maintain slightly boosted conditions, approximately 1.1bar for the tests presented here. Engine speed is externally specified and regulated by the engine dynamometer.

Chapter 3
Cycle-by-Cycle Data Analysis

3.1 Introduction

To better understand the dynamics associated with HCCI combustion and cyclic variability, data from engine experiments must be processed on a cycle-by-cycle basis to determine important features of the combustion process. Standard pressure based heat release analysis methods are extended here to run on a cycle basis and are additionally applied to the NVO region to capture effects of potential unburned fuel, which is an enabler to the onset of CV.

Inputs to the analysis include the in-cylinder pressure, exhaust lambda and temperature, mass of injected fuel and injection timing, valve timings, and engine speed. The analysis outputs a crank angle resolved cylinder temperature, heat release and ratio of specific heats as well as the combustion efficiency, residual gas fraction, the amount of unburned fuel and combustion phasing. The method is iterative and a flow diagram of the analysis can be found in Fig. 3.1.

3.2 Air Mass Determination

Cycle-by-cycle air mass determination is a challenging topic on a multicylinder engine due to pressure wave and flow phenomenon and limited measurement capabilities. For the purpose of offline analysis a method of using a cycle resolved exhaust lambda measurement will be used to determine the fresh air mass inducted into the cylinder on a per-cycle basis. The exhaust lambda sensor is typically located downstream of the engine and so there is a delay between its measurements and the actual in-cylinder response.

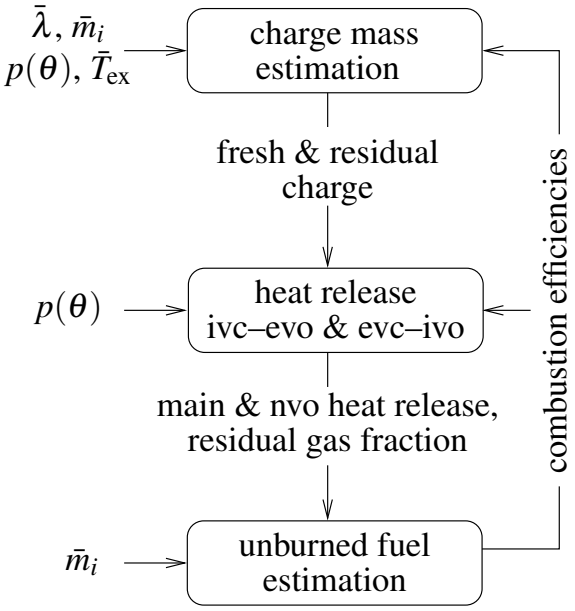

Figure 3.1: Flow diagram of the iterative cycle-by-cycle data analysis tool.

3.2.1 Lambda Sensor Delay

The quantification of the delayed response of the exhaust lambda sensor is dependent on the engine flow rate which is a function of the engine speed ω. Specifically, the transport delay time of the exhaust gases from the cylinder port to the sensor for a given exhaust configuration, and the sensor response time. The transport delay was quantified by performing open loop fuel steps on the engine. By commanding an instantaneous fuel step (direct injection) we can observe the time required to see the response in the lambda sensor for a particular engine speed. The response of the sensor is relatively fast in comparison to the transport delay and so it will be included in the transport delay. The overall lambda sensor response time is then given as $\tau_\lambda = f(\omega)$ where τ_λ is a number of engine cycles. The cycle shifted lambda signal is given by $\lambda(k) = \lambda_m(k - \tau_\lambda)$ where λ_m is the measured lambda signal and λ is the air fuel ratio to be used in the analysis.

3.2.2 Air Mass Response to Open Loop Steps

Once the response is shifted properly the air mass can be determined based on the stoichiometric air-fuel ratio of the fuel (AFR_s) the lambda measurement and the fuel in the cylinder m_f as in Eq. (3.1). The fuel in the cylinder is $m_f(k) = m_f^{inj}(k) + m_u(k)$ where the injected fuel mass is m_f^{inj} and m_u is the amount of unburned fuel from the

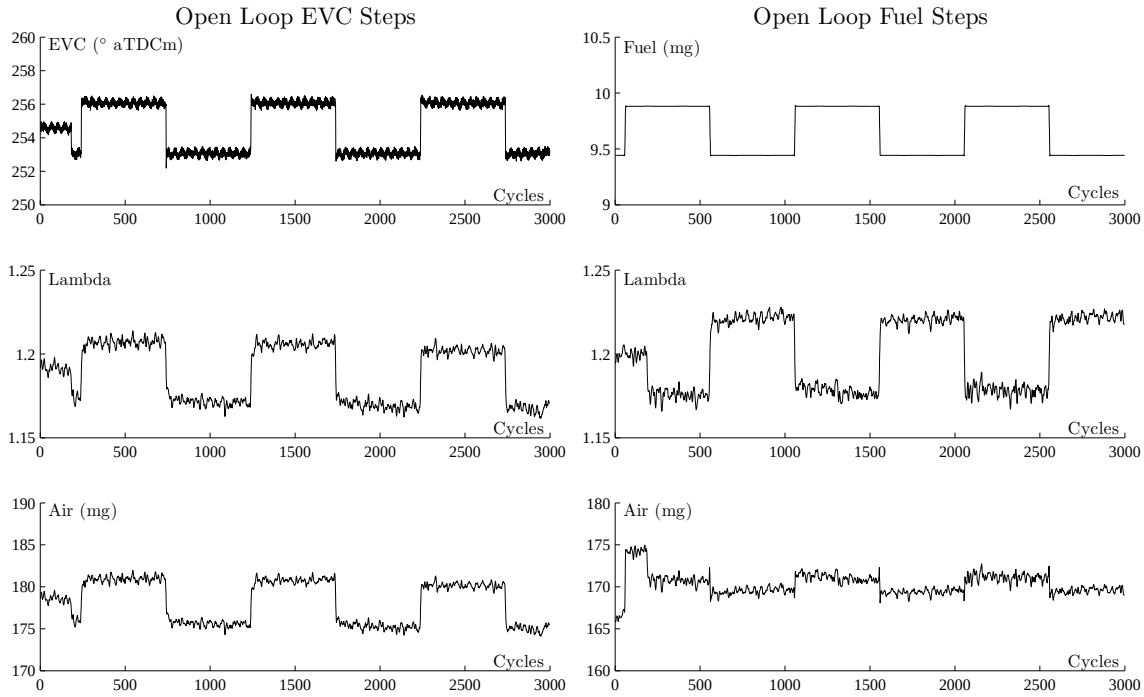

Figure 3.2: Calculated air mass based on cycle resolved lambda measurement for open loop steps in EVC (left) and fuel mass (right).

previous cycle. This value is determined later in the analysis however as an initial guess it assumed to be zero.

$$m_{air}(k) = m_f(k)\lambda_m(k - \tau_\lambda)AFR_s \tag{3.1}$$

Figure 3.2 shows the response of the the lambda sensor and the calculated air mass to open loop steps in mass of fuel and EVC. These two actuators affect the lambda sensor in similar ways, but the affect on air mass is different. A change in fuel mass does little to change the inducted air mass, however a change in the EVC position changes the total trapped residual mass, leaving more or less room for inducted air mass. This behavior is clearly captured in these results.

3.3 Residual Mass Estimation

Crucial to combustion analysis in HCCI is the determination of the mass of residuals carried from one cycle to the next. This can be defined as the mass of charge at EVC as given by the ideal gas law, $m_{res} = P_{evc}V_{evc}/RT_{evc}$, where m_{res} is the mass of residuals. The in-cylinder pressure is measured and the volume, V, is known. The

gas constant, R, is for burned gas composition and is assumed constant. Therefore to determine m_{res} we must find T_{evc}. To do so a system of equations is developed from which T_{evc}, and consequently m_{res}, may be solved.

In steady state conditions the mass flowing out of the cylinder is equal to mass of fresh air and fuel inducted into the cylinder within a given cycle. The mass that leaves through the exhaust process can therefore be described as

$$m_{out} = \frac{P_{evo}V_{evo}}{RT_{evo}} - \frac{P_{evc}V_{evc}}{RT_{evc}} = m_{air} + m_f = m_{in}, \tag{3.2}$$

where the pressures at the valve events are measured, as is the mass of fresh air, m_{air}, and the mass of injected fuel, m_f. This equation has two unknowns, T_{evo} & T_{evc}, therefore additional relations are needed.

In addition to conservation of mass in Eq. (3.2), the exhaust process can be approximated by an ideal gas undergoing a reversible process. The heat loss per unit mass during exhaust (EVO→EVC) is given by

$$q_1 = \int_{T_{evo}}^{T_{ref}} c_p dT - R \int_{P_{evo}}^{P_{ref}} \frac{T}{P} dP \tag{3.3}$$

$$q_2 = \int_{T_{ref}}^{T_{evc}} c_p dT - R \int_{P_{ref}}^{P_{evc}} \frac{T}{P} dP \tag{3.4}$$

where c_p is the specific heat of the exhaust gas which is assumed constant and known. Here it should be noted that the exhaust process has been split into two parts, q_1 a blowdown phase and q_2 a compression phase. The point used to split the exhaust process in two, defining the integration limits, will be referred to as the reference point. In [64] it is taken as the point at which the exhaust runner pressure is equal to 1 atm. To ascertain that there always is a reference point, even for boosted conditions, one could instead use the point of minimum pressure as in [19]. However, in highly variable conditions the minimum could occur close to the valve events. For example, it was observed that the minimum may be at EVO following a misfire, see Fig. 3.3. To avoid this scenario, the reference point is chosen to be fixed at the middle of the valve open period, $ref = \frac{\text{EVO+EVC}}{2}$.

The ratio of the heat losses during the two portions of the exhaust phase is given by

$$r_{ex} \equiv q_1/q_2 \ . \tag{3.5}$$

By combining equations (3.3), (3.4) and (3.5), with simplifications from [64], we arrive

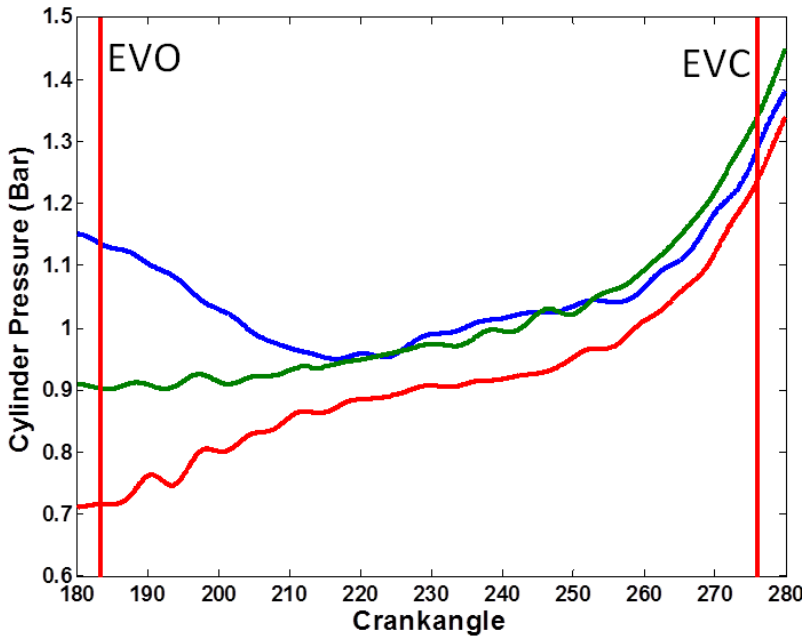

Figure 3.3: The minimum in the in-cylinder pressure trace can be see to occur at EVO for cycles which are a misfire (green and red) rather than in the middle for a normal cylce (blue). These cycles are consecutive in the order green, blue, red.

at the equation:

$$\gamma T_{evo} + r_{ex}\zeta T_{evc} = T_{ex}\left\{ -c_p(1-r_{ex}) + \frac{R}{2}\left(\ln\left(\frac{P_{ref}}{P_{evo}}\right) - r_{ex}\ln\left(\frac{P_{evc}}{P_{ref}}\right)\right)\right\} \quad (3.6)$$

$$\text{where: } \gamma = -c_p - \frac{R}{2}\ln\left(\frac{P_{ref}}{P_{evo}}\right), \quad \zeta = -c_p + \frac{R}{2}\ln\left(\frac{P_{evc}}{P_{ref}}\right).$$

The variable T_{ref} is the exhaust gas temperature at the reference point. This is taken to be the measured exhaust runner temperature, while P_{ref} is the measured cylinder pressure at the reference point. It is recognized that there may be a difference between the measured and actual temperature of the exhaust gas due to cooling of the thermocouple during the valve closed periods of the cycle. However analysis in [66, 67] has shown that an offset of $\pm 50\,\mathrm{K}$ has an approximate 2% effect on the resulting residual gas fraction. Based on this we approximate the measured value as the actual gas temperature.

The heat loss ratio r_{ex} is estimated by convective heat transfer to the walls as governed by

$$r_{ex} = \frac{\int_{evo}^{ref} h_c(\theta)A(\theta)(T_{cyl}(\theta) - T_w)d\theta}{\int_{ref}^{evc} h_c(\theta)A(\theta)(T_{cyl}(\theta) - T_w)d\theta}. \quad (3.7)$$

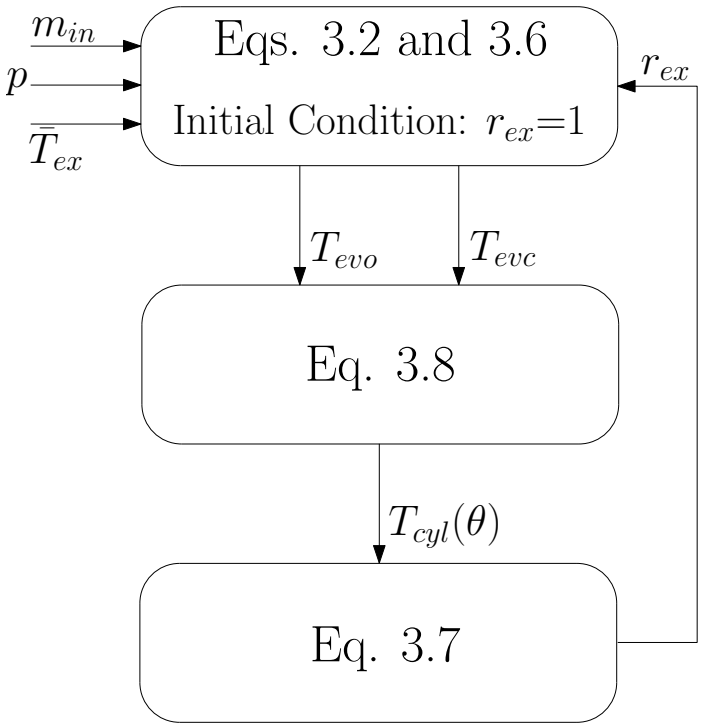

Figure 3.4: Flow diagram of the iterative process required to solve for the residual mass. Note the initial condition of the heat loss ratio.

The heat transfer coefficient, h_c, is determined using the Woschni method as in [68] as is the cylinder area, A. A constant wall temperature, T_w, is assumed. The in-cylinder temperature, T_{cyl}, is obtained from a polytropic assumption

$$T_{cyl}(\theta) = T_{ref}\left(\frac{P(\theta)}{P_{ref}}\right)^n, \tag{3.8}$$

$$\text{where } n = \begin{cases} ln\frac{T_{evo}}{T_{ref}}/ln\frac{P_{evo}}{P_{ref}}, & \text{Blowdown} \\ ln\frac{T_{evc}}{T_{ref}}/ln\frac{P_{evc}}{P_{ref}}, & \text{Compression.} \end{cases}$$

In summary, Eqs. (3.2), (3.6) and (3.7) are three equations with three unknowns T_{evo}, T_{evc} and r_{ex} which can be solved iteratively. A diagram of this iterative procedure can be found in Fig. 3.4.

With the solution (r_{ex}, T_{evo}, T_{evc}), the mass of residuals may be found with the ideal gas law. The residual gas fraction is then determined by:

$$x_r = m_{res}/(m_{air} + m_f + m_{res}) = \frac{P_{evc}V_{evc}T_{evo}}{P_{evo}V_{evo}T_{evc}}. \tag{3.9}$$

In most data sets the iterative routine requires less that 5 iterations to converge.

3.4 Heat Release Analysis

Gross heat release is determined for both main combustion and NVO using the first law of thermodynamics $Q(\theta) = Q_{net}(\theta) + Q_{ht}(\theta)$ as defined by Eqs. (3.10) (3.11) which are the heat release due to combustion and heat transfer respectively. The accumulated heat release for the main combustion event (θ =IVC→EVO) is defined as Q_m and the heat release for the NVO region (θ = EVC→IVO) is Q_n.

$$\frac{dQ_{net}}{d\theta} = \frac{1}{\gamma(\xi(\theta)) - 1} V dP + \frac{\gamma(\xi(\theta))}{\gamma(\xi(\theta)) - 1} P dV \tag{3.10}$$

$$\frac{dQ_{ht}}{d\theta} = A(\theta) h_c(\theta)(T_{cyl}(\theta) - T_w) \tag{3.11}$$

The heat transfer coefficient is determined using the modified Woschni correlation presented in [69] and a constant wall temperature was assumed. The value of γ is calculated on a crank angle basis as determined by the composition of the mixture:

$$\xi(\theta) = (1 - x_b(\theta))\xi_u + x_b(\theta)\xi_b(\theta), \tag{3.12}$$

and by the mass fraction burned

$$x_b(\theta) = \eta(k) Q(\theta) / \max Q(\theta). \tag{3.13}$$

The composition of burned and unburned gases are $\xi_b(\theta)$ and $\xi_u(\theta)$ respectively. The burned gas composition is computed from chemical equilibrium at $P(\theta)$ and $T(\theta)$. The value of $\eta(k)$ is the combustion efficiency which is assumed to be a constant of 95% for the first iteration of the heat release analysis and is updated in subsequent iterations by the equations in Sec. 3.7. The initial unburned fuel mass is zero, which contradicts the 95% efficiency. This is because that despite the fact combustion is never 100% efficient, the amount of unburned fuel which will make it through NVO and into the next cycle is nearly zero for a normal operating point. Therefore the initial unburned fuel mass is zero, convergence from initial conditions occurs quickly.

3.5 NVO Heat Release

The preceding heat release analysis is also applied during the recompression region (EVC→IVO) in the same manner that it was applied to the main combustion. During NVO, the charge mass is equal to the trapped residual mass and the composition

is assumed to be entirely burned gases. If there is a prediction of unburned fuel from the main combustion, this is taken into account through a change in composition as determined from chemical equilibrium. The composition is computed at each crankangle for a measured pressure and calculated temperature.

Application of the heat release analysis during NVO is critical to the understanding of cycle-by-cycle trends in high CV HCCI. This is because it allows one to quantify the fluctuation in the residual gas temperature as a consequence of unburned fuel, the driving factor behind high CV.

3.6 Cylinder Temperature

The in-cylinder temperature can be determined using the ideal gas law:

$$T_{cyl}(\theta) = \frac{P(\theta)V(\theta)}{m_x R(\theta)}, \text{ where } m_x = \begin{cases} m_{in} + m_{res} & \text{for } \theta = \text{IVC} \rightarrow \text{EVO} \\ m_{res} & \text{for } \theta = \text{EVC} \rightarrow \text{IVO}. \end{cases} \tag{3.14}$$

The mass, m_x, is dependent if the calculation is in the main compression or NVO region. The gas constant is dependent on the composition of the charge as determined by Eq. (3.12), $R(\theta) = f(\xi(\theta))$.

3.7 Combustion Efficiency

To determine the combustion efficiency of the main and NVO ($\eta_m(k)$, $\eta_n(k)$) compression regions, Eqs. (3.15) and (3.16) are used. Here the value of $Q_{m,max}$ and $Q_{n,max}$ are the maximum accumulated heat release for the main and nvo regions respectively. The value of x_r is given by Eq. (3.9) and q_{lhv} is the lower heating value of the fuel.

$$\eta_m(k) = \frac{Q_{m,max}(k)/q_{lhv}}{m_f(k)}, \tag{3.15}$$

$$\eta_n(k) = \frac{Q_{n,max}(k)/q_{lhv}}{x_r(k)(m_f(k) - Q_{m,max}(k)/q_{lhv})}. \tag{3.16}$$

The mass of fuel is defined as $m_f(k) = m_f^{inj}(k) + m_u(k)$ where m_u is the mass of unburned fuel carried over from the previous cycle as discussed in Sec. 3.8, as an initial condition $m_u(0) = 0$. These efficiencies are used in the next iteration of heat release and x_r estimation as described by Fig. 3.1, iterations continue until the change in both

efficiencies and the unburned fuel is sufficiently small. These efficiencies are prone to error because of uncertainties in the inputs and largely unknown heat transfer properties. However the results are still useful because they tell us crucial information about the presence of unburned fuel in the recompression region and couple this value with poor burns during the main combustion as will be discussed in Chap. 5.

3.8 Residual Fuel

Data with high variability can have cycles with incomplete burns. When this occurs a portion of the fuel is left unburned and carried over to the next cycle, through NVO. This residual fuel has a major impact on behavior of the engine and it is therefore important to quantify it. To do so, the mass of unburned fuel is computed from the difference equation derived in [19],

$$m_u(k+1) = x_r(k)\left(\bar{m}_f^{inj} + m_u(k) - \frac{Q_{m,max}(k)}{q_{lhv}}\right) - \frac{Q_{n,max}(k)}{q_{lhv}}, \tag{3.17}$$

which is dependent on an initial unburned fuel mass, $m_u(0) = 0$. An analysis of this equation in [70] shows that it will converge to the correct value given any initial guess within a small number of iterations, convergence is typically achieved in less than 10 cycles.

3.9 Iteration

The results of the residual fuel and combustion efficiency estimation are carried over to the next iteration of the combustion analysis for a particular cycle starting with Sec. 3.2 as indicated in Fig. 3.1. This iterative procedure is repeated until the change in residual fuel and combustion efficiency is sufficiently small from one iteration to the next. At the conclusion of the iterations the analysis can progress to the next cycle.

3.10 Combustion Phasing

Upon completion of the iterative heat release analysis for a given cycle, the combustion phasing for that cycle can be determined. The combustion phasing is taken as

the point at which 50% of the charge mass has burned according to the gross heat release analysis. This is found by normalizing the heat release during main combustion by the maximum heat release:

$$x_b(\theta) = \frac{Q_m(\theta)}{max_\theta Q_m}. \tag{3.18}$$

This will yield the mass fraction burned curve $x_b(\theta)$ from which the angle of 50% burned can be extracted by simple interpolation. The mass fraction burned curve is typically only calculated for the main combustion event. The combustion phasing is defined as:

$$x_b(\theta_{50}) \equiv 0.5. \tag{3.19}$$

3.11 Summary

The methods for cycle-by-cycle data analysis presented in this chapter are heavily dependent on the quality of the input signals used. Special care must be take to ensure that all signals are correctly synchronized, and filtered if needed. This is especially important for air mass determination as this can cause large errors in the heat release analysis. This analysis could benefit from the addition of a cylinder filling model which could more accurately determine mass flow changes on a cycle basis.

These analysis tools are used in Chapter 5 to study highly variable data. For this type of analysis the determination of the residual fuel in Sec. 3.8 is paramount since there can be very poor burns on one cycle followed by excessive combustion on the next. The quantification of this fluctuation in energy is important for understanding the cyclic variability, this will be the focus of Chapter 5.

In Chapter 4 the method of determining the residual gas fraction from Sec. 3.3 is treated in more detail. Specifically, modifications to the analysis are made to allow for online implementation of the algorithm. An analysis is also done to evaluate the algorithms ability to predict cycle-by-cycle trends for high CV data.

Chapter 4

Online Residual Mass Estimation for Highly Variable Data

4.1 Motivation

Autoignition timing control in HCCI combustion requires careful regulation of the temperature, pressure and composition of the pre-combustion cylinder charge. The regulation of charge properties is carried out in recompression HCCI by retaining a large fraction of the post-combustion residual gases before they can be exhausted [10, 11], in addition to control of the fuel injection timing. Accurate modeling of the residual gas fraction is important for a control oriented model due to HCCI's high sensitivity to the thermal energy associated with the residual gases. If too much residual mass is trapped the combustion can occur very early causing potential engine damage and a loss in efficiency. If too little mass is trapped the combustion can become highly oscillatory [18, 70] and misfires may occur resulting in torque fluctuations.

As such it is desirable to have a method for estimating the residual gas fraction online. This can prove useful for understanding the cycle-by-cycle trends of HCCI and could also be used to improve the accuracy of control oriented models. While there have been several methods described in literature for estimating the residual mass [64, 66, 71, 72], none provide an algorithm capable of online implementation without the use of a steady-state assumption. The following section will present a method of estimating the trapped residual mass which is simple enough to be implemented on embedded hardware while still maintaining a physical basis and alleviating the need of a steady state assumption. The algorithm is based on the cycle resolved data analysis of Sec. 3.3. The result is a model for the dynamics of the trapped residual mass.

4.2 Derivation of Difference Equation

The following derivation will employ mass and energy balance equations during the exhaust portion of the cycle (EVO→EVC) as well as several measurements to determine the trapped residual mass. This method is only valid for recompression combustion methods meaning that the exhaust valve must closed before TDC.

In Sec. 3.3 the amount of heat lost per unit mass through the exhaust process was found iteratively by Eqs. (3.2), (3.6) and (3.7). For online implementation we utilize only Eq. (3.6) repeated here for reference:

$$\gamma T_{evo} + r_{ex}\zeta T_{evc} = T_{ex}\left\{ -c_p(1-r_{ex}) + \frac{R}{2}\left(\ln\left(\frac{P_{ref}}{P_{evo}}\right) - r_{ex}\ln\left(\frac{P_{evc}}{P_{ref}}\right)\right)\right\} \tag{4.1}$$

$$\text{Where: } \gamma = -c_p - \frac{R}{2}\ln\left(\frac{P_{ref}}{P_{evo}}\right), \quad \zeta = -c_p + \frac{R}{2}\ln\left(\frac{P_{evc}}{P_{ref}}\right).$$

Equation (4.1) on its own has three unknowns T_{evo}, T_{evc} and r_{ex} as well as other variables which are either known or can be measured as described by Sec. 3.3.

In Sec. 3.3 steady state was assumed through conservation of mass in Eq. (3.2), if we instead define the unknown temperatures with the ideal gas law:

$$T_{evo} = \frac{P_{evo}V_{evo}}{m_{evo}R}, \tag{4.2}$$

$$T_{evc} = \frac{P_{evc}V_{evc}}{m_{evc}R}, \tag{4.3}$$

and define the masses as follows:

$$m_{evo} = m_{in}(k) + m_{res}(k), \quad m_{evc} = m_{res}(k+1),$$

where the value of $m_{in}(k) = m_{air}(k) + m_f(k)$. Then Eq. (3.6), (4.2) and (4.3) can be combined and written as

$$\frac{\gamma P_{evo}V_{evo}}{(m_{in}(k)+m_{res}(k))R} + \frac{r_{ex}\zeta P_{evc}V_{evc}}{m_{res}(k+1)R} = T_{ex}\left\{ -c_p(1-r_{ex}) + \frac{R}{2}\left(\ln\frac{P_{ref}}{P_{evo}} - r_{ex}\ln\frac{P_{evc}}{P_{ref}}\right)\right\} \tag{4.4}$$

This equation has two remaining unknowns m_{res} and r_{ex}. We can hypothesize that the value of r_{ex} will be greater than or equal to one. This can be physically justified by the fact that blowdown occurs in the first part of the exhaust process. Blowdown

is a process in which much of the heat, and therefore mass, is lost due a rapid equalization of pressure between the exhaust manifold and cylinder. Since we have defined the two portions to be of equal length, this suggests that there will be more heat loss in q_1 than q_2 in most circumstances. The exact value of this ratio is unknown without the iterative process from Sec. 3.3 however the offline analysis supports this claim where the average value across multiple operating conditions is $r_{ex} = 1.5$. The effect of r_{ex} on the final result is small, as will be shown later. It could therefore be delegated as a tuning factor, for this analysis it is assumed a known constant.

Equation (4.4) can be written more compactly by grouping terms and lumping constant coefficients:

$$m_{res}(k+1) = \frac{\alpha(k) + \beta(k) m_{res}(k)}{A(k) + m_{res}(k)} \tag{4.5}$$

where:

$$\alpha(k) = \left(\frac{-2r_{ex}c_p + r_{ex}R\ln\frac{P_{evc}}{P_{ref}}}{-2c_p(1+r_{ex}) + R\left(\ln\frac{P_{ref}}{P_{evo}} - r_{ex}\ln\frac{P_{evc}}{P_{ref}}\right)} \right) \left(\frac{P_{evc}V_{evc}}{RT_{ex}} \right) m_{in}(k)$$

$$\beta(k) = \left(\frac{-2r_{ex}c_p + r_{ex}R\ln\frac{P_{evc}}{P_{ref}}}{-2c_p(1+r_{ex}) + R\left(\ln\frac{P_{ref}}{P_{evo}} - r_{ex}\ln\frac{P_{evc}}{P_{ref}}\right)} \right) \left(\frac{P_{evc}V_{evc}}{RT_{ex}} \right)$$

$$A(k) = \left(\frac{2c_p + R\ln\frac{P_{ref}}{P_{evo}}}{-2c_p(1+r_{ex}) + R\left(\ln\frac{P_{ref}}{P_{evo}} - r_{ex}\ln\frac{P_{evc}}{P_{ref}}\right)} \right) \left(\frac{P_{evo}V_{evo}}{RT_{ex}} \right) + m_{in}(k)$$

The values of P_x, T_x and V_x are all from the $k+1$ cycle. Equation (4.5) predicts the amount of residual mass in cycle $k+1$ based on previous measured data and the value of the residual mass on the previous cycle. Therefore the only unknown is the initial guess of $m_{res}(0)$. It will be shown in the following sections that regardless of the initial guess, the difference equation will converge relatively quickly to a stable equilibrium. A limitation of the algorithm is that it requires a transient air mass as an input. Figure 4.1 provides a visual representation of this algorithm and its inputs relative to the cycle definition at EVO.

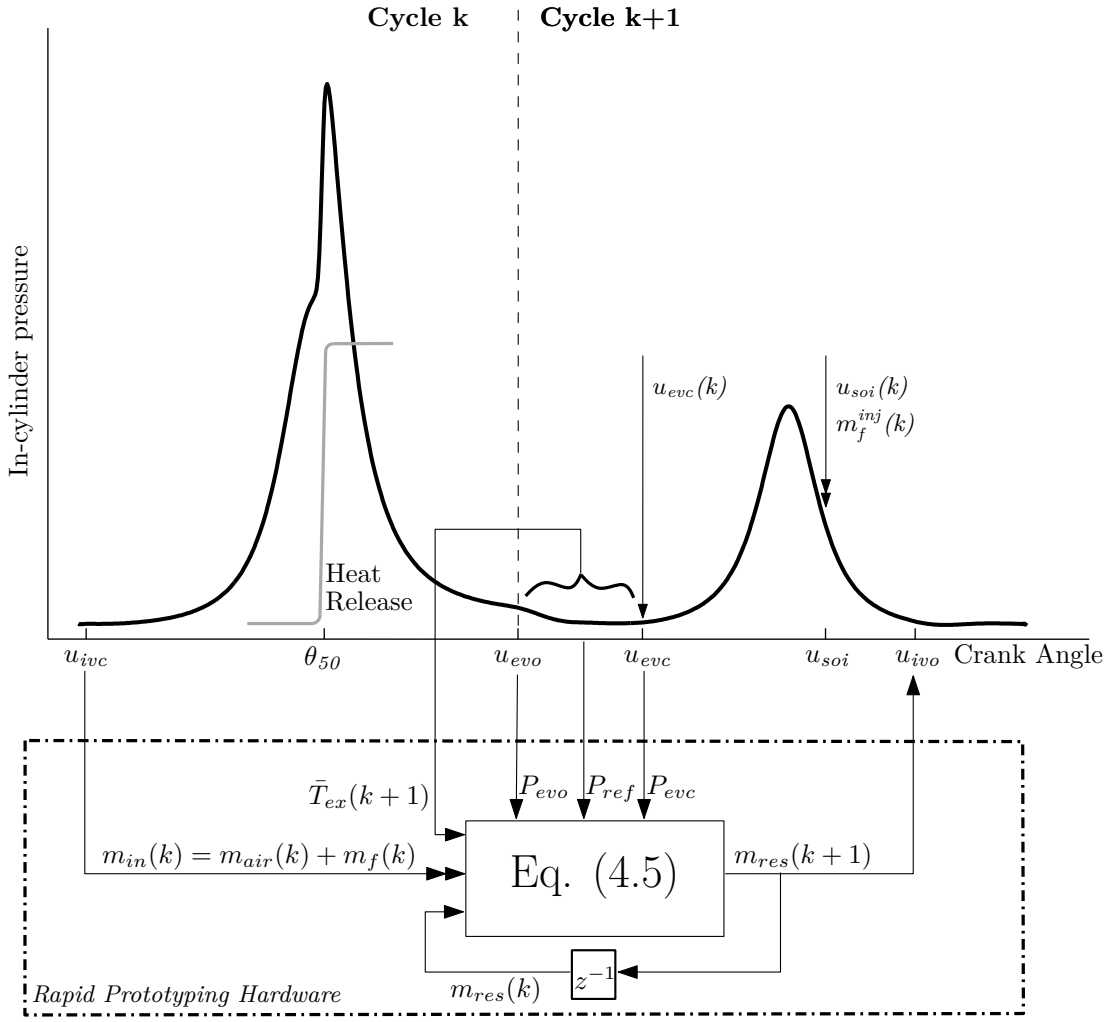

Figure 4.1: A block diagram representation of the inputs and outputs of the online residual mass estimation.

4.3 Possible Numerical Issues

Due to the fact that Eq. (4.5) is rational, there are sets of constants (α, β, A) for which the difference equation is undefined, namely when division by zero occurs. It is important that we consider these possibilities to understand any numerical issues that may arise. For the following analysis, r_{ex} is assumed to be equal to 1 for mathematical simplicity. Division by zero occurs when:

$$A + m_{res}(k) = 0 \rightarrow m_{res}(k) = -A.$$

It is unlikely that division by zero will occur because the coefficients are noisy and therefore an exact division by zero is improbable however small numbers could also cause numerical issues. Additionally, this implies that m_{res} would have to be negative for this to occur. This scenario is obviously unphysical and can be avoided by picking a positive initial guess of residual mass as discussed further in Sec. 4.4.1.

Another possible numerical issue occurs when $\alpha = \beta A$. This causes a single solution for all cycles:

$$m_{res}(k+1) = \frac{\beta A + \beta m_{res}(k)}{A + m_{res}(k)} = \beta \; \forall \; k \geq 0.$$

Essentially, the algorithm could become "stuck" on this solution if there were no change in the coefficients. This is once again improbable since the coefficients are noisy and, if we evaluate the term $\alpha - \beta A = 0$ we see that for this to be true:

$$\left(\frac{2c_p + R \ln\left(\frac{P_{ref}}{P_{evo}}\right)}{-4c_p + R \ln\left(\frac{P_{ref}^2}{P_{evo} P_{evc}}\right)} \right) \left(\frac{P_{evo} V_{evo}}{R T_{ex}} \right) = 0.$$

Since we know the ratio inside the natural log is always close to 1 then the value of the logarithm is close to zero. Additionally, $P_{evo}V_{evo}$ can never equal zero and the value of $2c_p$ is always positive so it is unlikely this expression is ever true.

4.4 Proof of the Existence of Two Real Solutions

Equation (4.5) can have multiple solutions as shown in [73] where an equation of this form is known as the Riccati Difference Equation. It is important to understand what these solutions are for a given set of input data and the stability of each solution.

The coefficients α, β and A in [73] are treated as constants, for this analysis they are also assumed to constant. This is a reasonable assumption as for a given operating condition the coefficients will not change much from cycle to cycle. The coefficients for this analysis were determined from experimental data.

Since the equation is rational and of second order, it can have at most two solutions; these solutions can be real or imaginary. To find the two solutions we impose a change of variables such that:

$$m_{res}(k) = (\beta + A)w(k) - A \;\; \forall \; k \geq 0,$$

and substitute this into Eq. (4.5) we then have the difference equation:

$$w(k+1) = 1 - \frac{Q}{w(k)} \;\; \text{where} \;\; Q = \frac{\beta A - \alpha}{(\beta + A)^2}. \tag{4.6}$$

At steady state, $w(k+1) = w(k) = w$, the expression can be written as $w^2 - w + Q = 0$. This is an easily solved quadratic equation which yields the two possible solutions:

$$w_- = \frac{1 - \sqrt{1 - 4Q}}{2} \text{ and } w_+ = \frac{1 + \sqrt{1 - 4Q}}{2}. \tag{4.7}$$

If $Q < \frac{1}{4}$ then Eq. (4.6) has two real solutions. If $Q > \frac{1}{4}$ then there are two imaginary solutions and if $Q = \frac{1}{4}$ then the solutions are $w_- = w_+ = \frac{1}{2}$.

To prove this equation always has these two solutions we can show the value of Q is less than $\frac{1}{4}$ and is negative for any physically reasonable set of pressure data. To do this we examine the sign of Q. We may first exclude the denominator because it is squared and will always be positive. Therefore the sign of Q is dictated by the sign of the numerator alone. The numerator, $\beta A - \alpha$, can be rearranged as $\beta(A - m_{in}(k))$ which can be evaluated in detail as:

$$\beta(A - m_{in}(k)) = \left(\frac{\left(-2c_p + R\ln\left(\frac{P_{evc}}{P_{ref}}\right)\right)\left(2c_p + R\ln\left(\frac{P_{ref}}{P_{evo}}\right)\right)}{\left(-4c_p + R\ln\left(\frac{P_{ref}^2}{P_{evo}P_{evc}}\right)\right)^2} \right) \left(\frac{P_{evc}V_{evc}P_{evo}V_{evo}}{R^2T_{ex}^2} \right)$$

From this we can see that the sign of Q is determined by:

$$\left(-2c_p + R\ln\left(\frac{P_{evc}}{P_{ref}}\right)\right)\left(2c_p + R\ln\left(\frac{P_{ref}}{P_{evo}}\right)\right),$$

since $(P_{evc}V_{evc}P_{evo}V_{evo})$ is always positive. Expansion of terms yields:

$$-4c_p^2 + 2c_pR\ln\left(\frac{P_{evc}P_{evo}}{P_{ref}^2}\right) + R^2\ln\left(\frac{P_{evc}}{P_{ref}}\right)\ln\left(\frac{P_{ref}}{P_{evo}}\right). \tag{4.8}$$

The sign of this term dictates the sign of Q. To find the sign of this term we must apply some constraints on the pressures. We know during the exhaust process $P_{evo},\ P_{evc},\ P_{ref}$ are all very close to one another, therefore

$$\frac{P_{evc}P_{evo}}{P_{ref}^2} \approx \frac{P_{evc}}{P_{ref}} \approx \frac{P_{ref}}{P_{evo}} \approx 1.$$

Because of this, the last two terms of Eq. (4.8) are very close to zero and are small by comparison to the first term, which is always negative. In fact, for Eq. (4.8) to become positive the pressure ratios inside the natural logs would all have to be greater than 20. Since exhaust pressures are usually around 1 bar and not more than 5 bar for most applications, pressure ratios of this magnitude are not feasible. We can therefore conclude the sign of Q is always negative for physically reasonable data and there will always be two solutions, $w_-,\ w_+$, given by Eq. (4.7). Using this same argument we can support the claim in Sec. 4.3 that $\alpha - \beta A$ is not equal to zero. The preceding argument shows $\beta A - \alpha$ is always less than zero. If this is true then $\alpha - \beta A$ must always be greater than zero and it can therefore not be equal to zero.

4.4.1 Convergence

The result found in Eq. (4.5) predicts the amount of residual mass in cycle $k+1$ based on measured data and the value of the residual mass in the previous cycle. Therefore, the only unknown is the initial guess of $m_{res}(0)$. Since we know the equation has two fixed point solutions for a given set of coefficients, as shown in Sec. 4.4, it is desirable to know how the equation converges to these solutions and if the solutions are stable.

If typical values of α, β and A are used in the residual mass estimation and held constant, the change from one cycle to the next can be determined from the discrete derivative of Eq. (4.5).

An example of this is shown in Fig. 4.2 for initial conditions ranging from -1000 to 1000mg. Here the equation has equilibria at -94.4 and 220.9mg. Clearly the negative solution is non-physical as we cannot have a negative mass. If we linearize the function at each one of the equilibria, we find that the slope at the negative solution

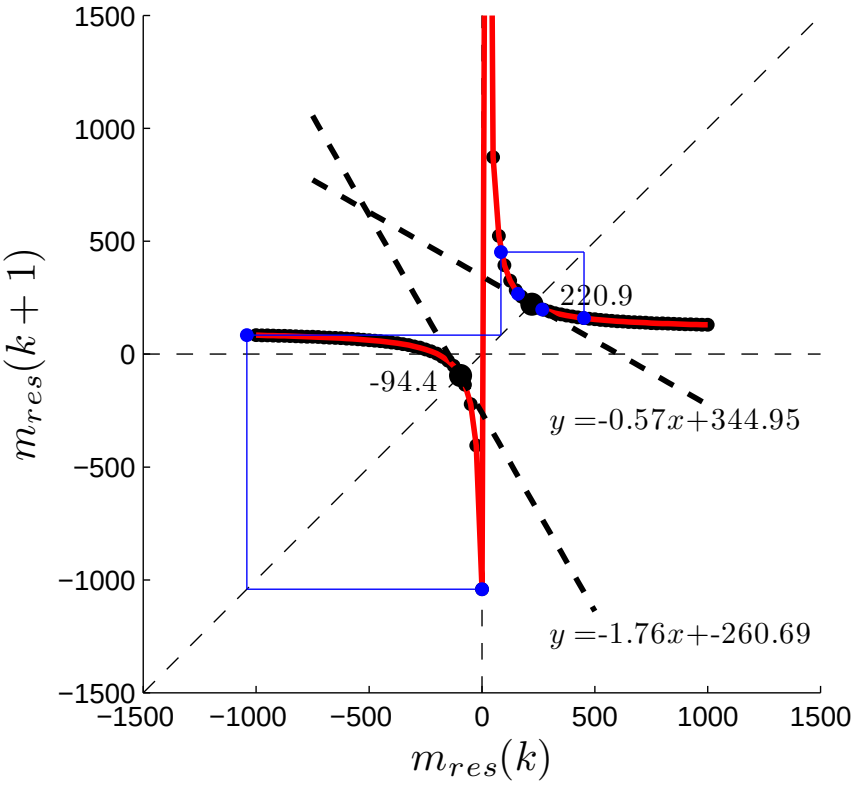

Figure 4.2: Change in the value of the estimated m_{res}, in milligrams, from one cycle to the next. Two fix point solutions are shown and the slope at each point indicates the solutions stability.

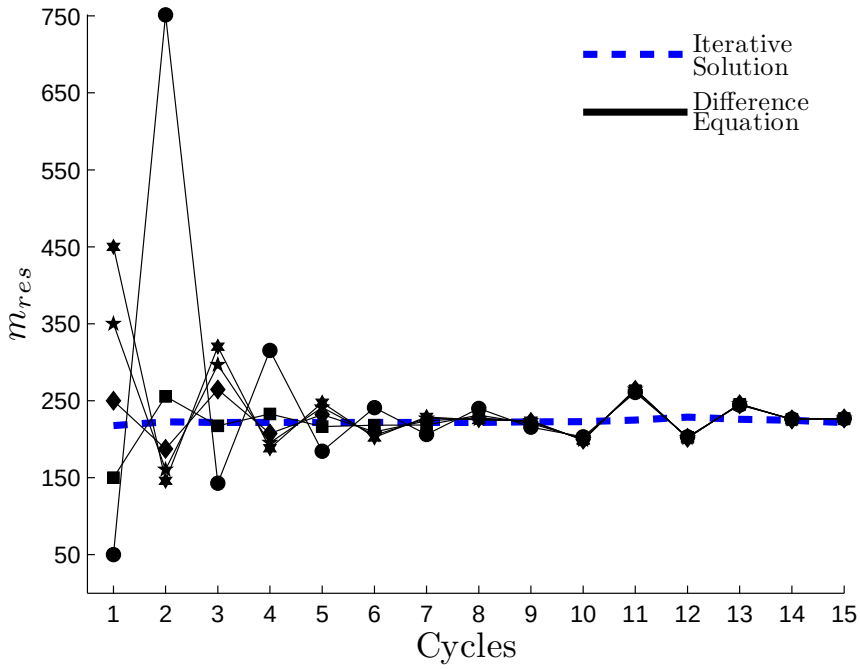

Figure 4.3: Convergence of the state m_{res}, in milligrams, from various initial guesses. Simulation was run at 1800 rpm and 3 bar IMEP.

is outside the criteria for a stable equilibrium. Specifically, if the solution were stable the slope at the solution would be $-1 < m < 1$, where m is the slope of the function at the particular point. The slope at the positive equilibria is however stable, although oscillatory. As such an initial condition which is close to stable equilibria will converge to the positive solution for this set of coefficients. The figure shows how an initial guess of $m_{res}(0) = 0$ would converge to the stable equilibrium in blue.

Convergence from various positive initial guesses is shown in Fig. 4.3. It can be seen here that the equation converges to the same solution within a small number of cycles. Additionally it converges to approximately the same value as a higher fidelity offline analysis tool [64]. Further stability properties of the Riccati Difference Equation can be found in [73, 74, 75].

4.4.2 Sensitivity

In the preceding analysis the heat loss ratio r_{ex} was assumed to be 1 for mathematical simplicity. However, it will most likely always be greater than 1. To better understand the effect that this parameter has on the residual mass estimate, an analysis was done in which the state was allowed to converge to steady state for an guess of

$m_{res}(0) = 250mg$ and for values of r_{ex} ranging from 0.75 to 2. The result can be found in Fig. 4.4. Here it can be seen that the positive solution (w_+) is mostly insensitive for values of r_{ex} greater than one. A change of approximately 1mg is observed from $r_{ex} = 1 \rightarrow 2$. Therefore, due to the insensitivity, it is a valid assumption to allow this parameter to stay constant. It could also be tuned to offline data analysis results. For the data presented in Fig. 4.5 the average value from offline analysis was found to be $r_{ex} = 1.5$.

Also shown in Fig. 4.4 is the sensitivity of the unphysical solution (w_-) to the heat loss ratio. This solution does have a high sensitivity, however as r_{ex} is increased the solution become more negative. It can also be seen how the slope of the function changes at these two equilibrium. For the positive solution the slope remains stable. The unphysical solution is persistently unstable.

Since the residual estimation state depends on measurements of the exhaust gas temperature and fresh air mass, it is important to determine the sensitivity of the equation to these parameters. Figure 4.4 also shows how the residual mass changes as a function of an error in the measurement of exhaust gas temperature and fresh air mass. The effect of these errors is approximately affine and relatively flat, indicating low sensitivity. The result is more linear for a heat loss ratio greater than 1.

4.5 Experimental Results

The residual estimation routine was implemented on the rapid prototyping hardware as described in Chapter 2. The engine was run in open loop for these tests except for closed loop control of the engines coolant, oil temperature and speed.

4.5.1 Comparison to Steady State Data

To validate the online residual estimation's accuracy, it was compared to the results from the offline analysis presented in Sec. 3.3. The dataset used spans multiple speeds, loads and actuator settings and is therefore representative of the range of inputs that the equation would receive when operating online. The results in Fig. 4.5 show that for values of $r_{ex} = 1$ the fit is good with the exception of a few outliers. The outliers correspond to higher load points. For these, the pressure in the cylinder at the point of EVO was high due to higher peak pressures. The result is a larger blowdown event which would make the value of r_{ex} necessarily greater than 1. The results are better

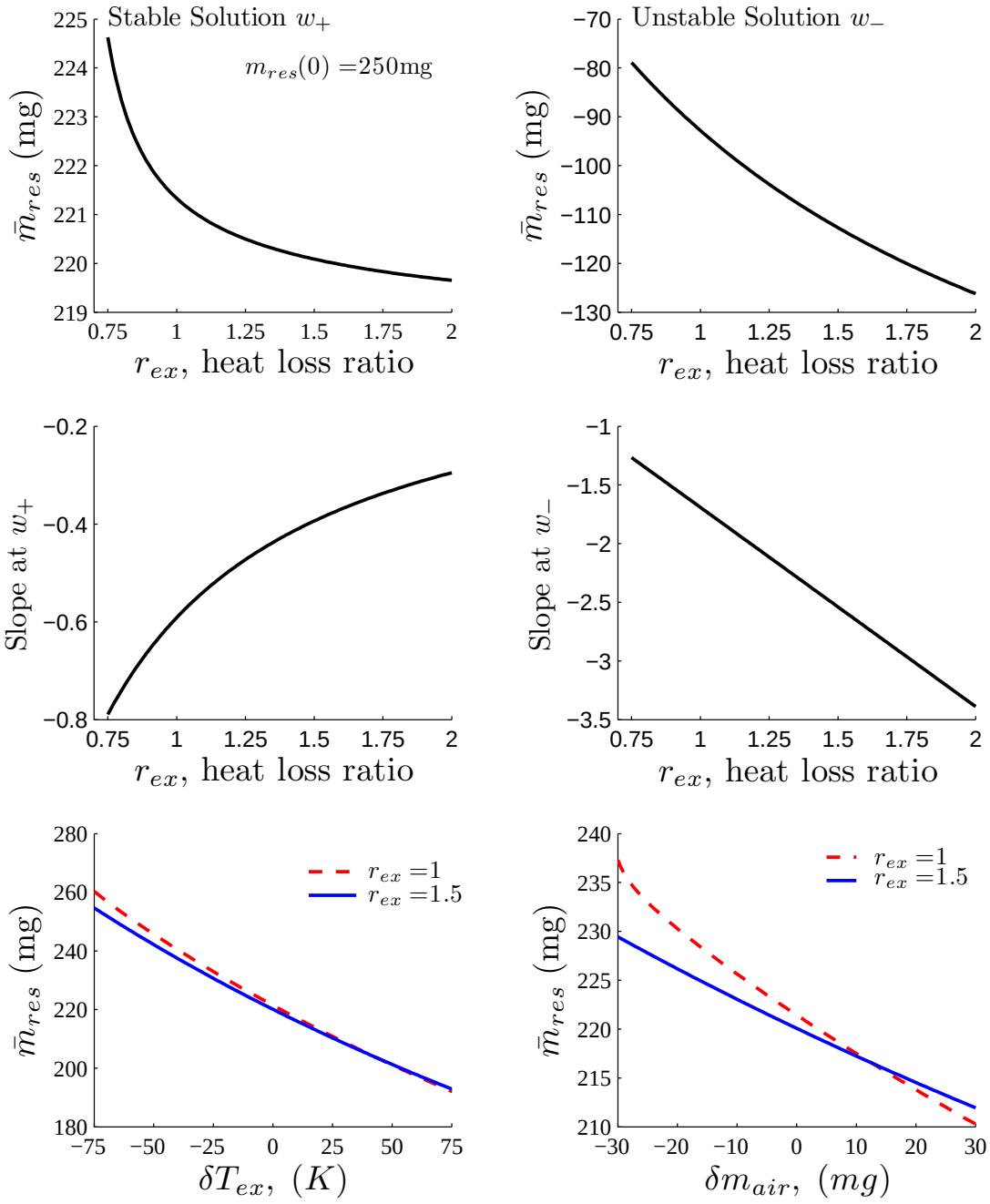

Figure 4.4: The effect of various heat loss ratios on the solutions of Eq. (4.5) as well as the stability of each solution are shown in the top four plots. Sensitivity of the residual mass to errors in the measured exhaust gas temperature for two heat loss ratios are shown in the bottom two plots.

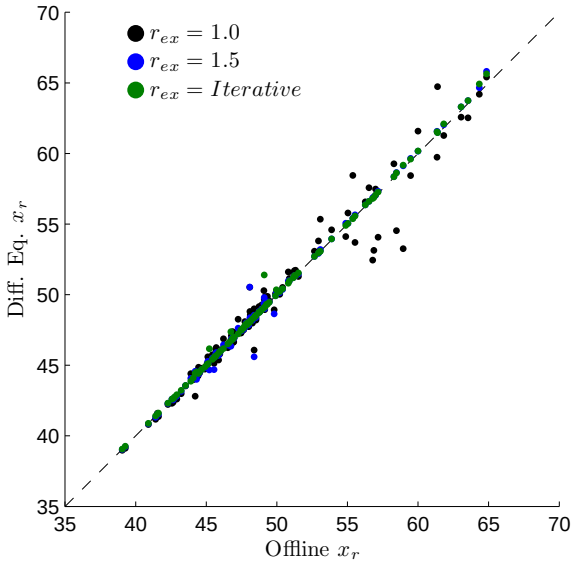

Figure 4.5: Comparison of the online residual estimation with that of an iterative offline analysis tool from Chapter 3

when a heat loss ratio greater than 1 is used and nearly identical to the offline analysis when the value of r_{ex} from the iterative method is used.

4.5.2 Cycle-by-Cycle Trends

Since the residual mass trapped in the cylinder can change quickly on a cycle-by-cycle basis it is important to quantify how well the algorithm can capture these fluctuations. Figure 4.6 shows the result of the online difference equation and offline analysis for a highly variable dataset. This data was made variable by reducing the amount of negative valve overlap and therefore trapped residual mass such that the combustion phasing became sufficiently late to induces oscillations in the combustion phasing [70].

Figure 4.6 shows that the online estimation well approximates the offline result in terms of direction of change from one cycle to the next. The standard deviation of the online result is higher than that of the offline. This is due to the oscillatory convergence of the online estimation. When a heat loss ratio greater than 1 is used the amplitude of oscillations are reduced. This is the same result deduced from Fig. 4.4 where we see that the slope of the function at the physical solution is approaching zero as the heat loss ratio is increased. This slope is analogous to the eigenvalue of the system. In discrete time an eigenvalue on the left-half plane and inside the unit circle is stable but oscillatory. As we move the eigenvalue closer to positive values

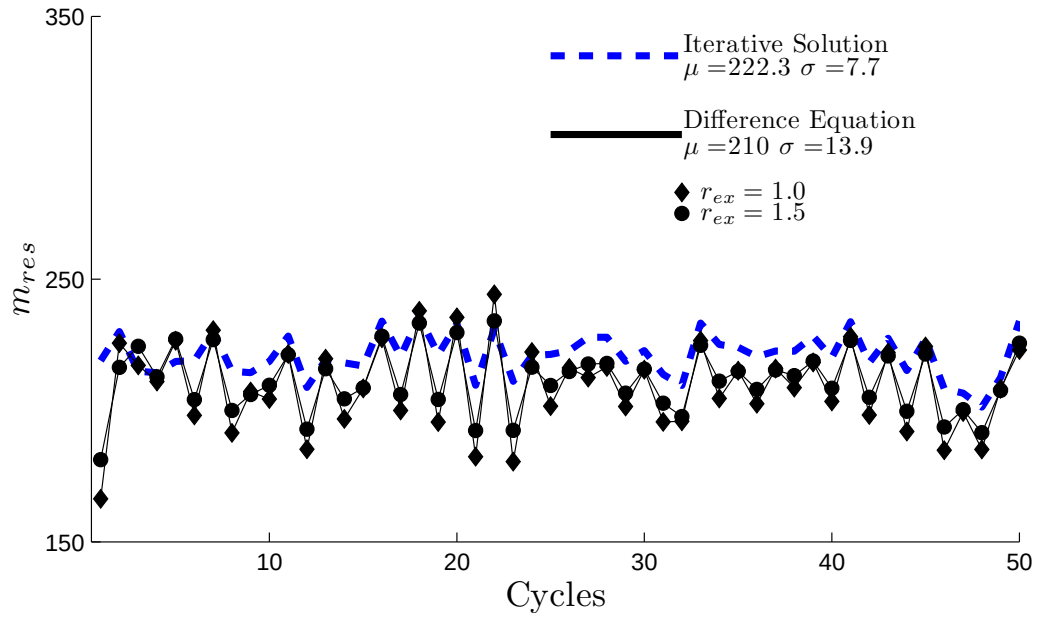

Figure 4.6: Cycle resolved resutls of residual mass for different values of r_{ex}. Despite the data's high variability the algorithm captures cycle-by-cycle trends well. The increased value of r_{ex} dampens oscillations.

the dampening of the system increases.

To further check the statistical properties of the algorithm we consider the full test from Fig. 4.6 which is 3000 cycles long. The results are presented in Fig. 4.7 with return maps and normal probability plots. A return map shows the relationship between consecutive cycles which provides insight on the dynamic behavior of the CV, this tool is explained in further detail in Sec. 5.2.2. Here the return map is the plot of the residual mass in cycle k versus the residual mass in cycle $k+1$. When comparing the online and offline results we can see that the online analysis results are stretched slightly perpendicular to the diagonal indicating oscillatory behavior. This is most likely caused by the heat loss ratio being tuned slightly low as previous results would indicate. The results for both cases are mostly Gaussian as indicated by the normal probability plots.

Even though the residual gas fraction data in Fig. 4.7 appears to have fairly low variability, the effect on the combustion is actually significant. This is made clear by the return maps of combustion phasing and heat release in Fig. 4.8.

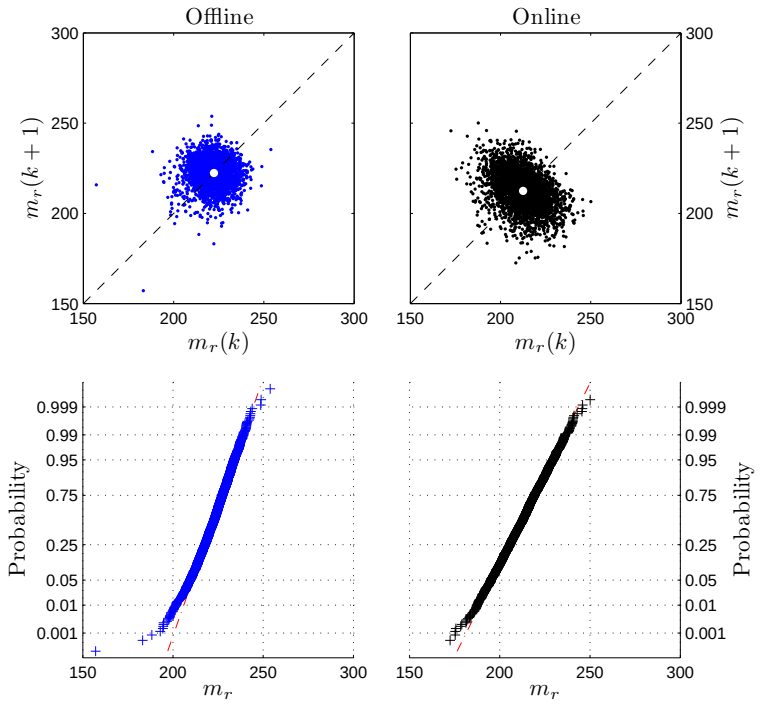

Figure 4.7: Return maps and normal probability plots of the online and offline residual estimation for a highly variable data set.

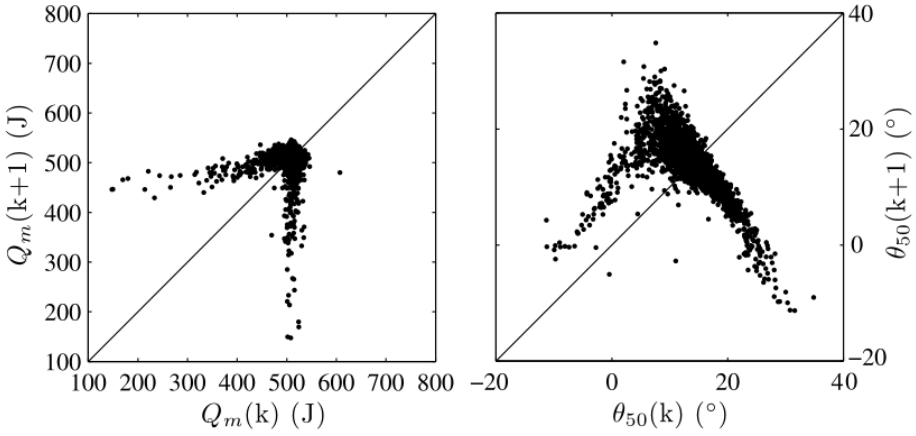

Figure 4.8: Return maps of heat release and combustion phasing for the data presented in Fig. 4.7. Here is can be seen that despite the low variability in the return maps of residual gas fraction, the combustion is erratic in terms of θ_{50} and heat release.

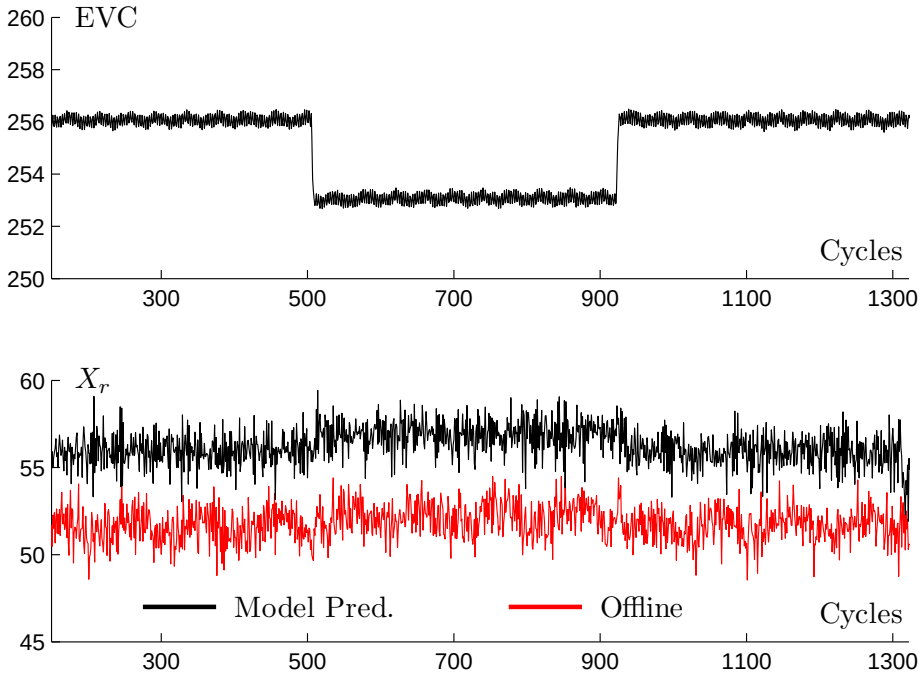

Figure 4.9: An EVC step for cylinder 1. The online residual gas fraction prediction (black) is compared against the offline prediction (red). The cycle-by-cycle predictions are good throughout the test however there is an offset in the mean value most likely caused by the exhaust gas temperature sensor.

4.5.3 Actuator Steps

To evaluate the effectiveness of the residual gas fraction estimation in transients, actuator steps of the model inputs were performed in open loop. Sensor measurements were obtained in real time from the engine and used by the model for real time prediction of x_r. A step in EVC is shown in Fig. 4.9 for cylinder 1. The step is from 256 to 253°$aTDC$ (degrees after top dead center) and back again and causes the amount of NVO to increase momentarily as a result. Intuitively, the amount of residual mass trapped in the cylinder should also increase, this is reflected in the prediction of the residual gas fraction. Also shown is the result of the offline analysis of the residual gas fraction from Chapter 3. While the absolute difference between the two results is slightly different, the magnitude and direction of the transient response is similar.

The model's response to steps in SOI and mass of fuel can be found in Figs. 4.10 and 4.11. These actuators have little effect on the residual gas fraction however the magnitude and direction of the transient response is once again similar when compared to the offline analysis. The mean value of the residual gas fraction is off for all three of these tests. This is most likely due to the measurement of the

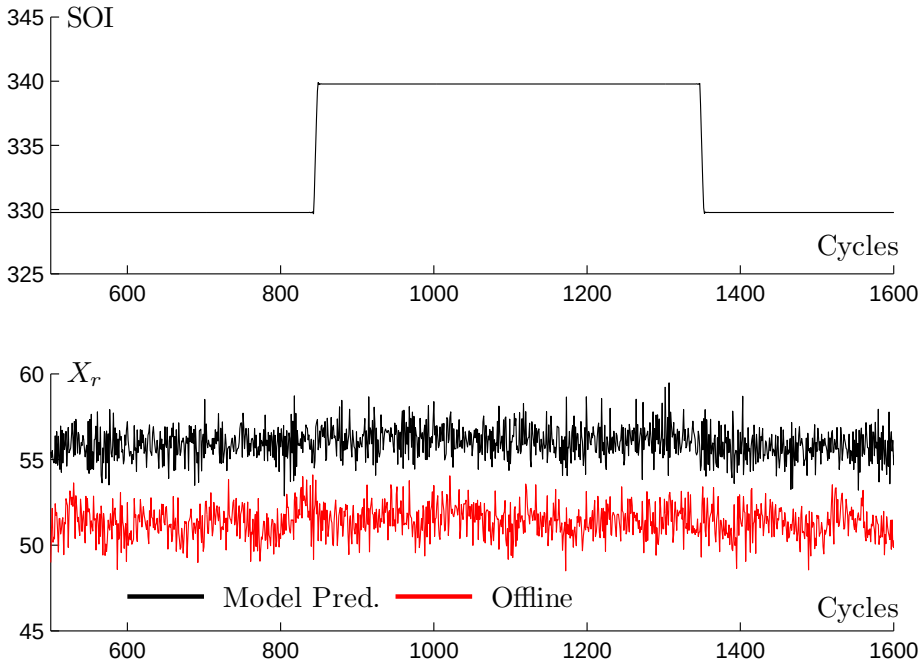

Figure 4.10: An SOI step for cylinder 1. The online residual gas fraction prediction (black) is compared against the offline prediction (red). The cycle-by-cycle predictions are good throughout the test however there is an offset in the mean value most likely caused by the exhaust gas temperature sensor.

exhaust gas temperature being inaccurate. This problem can be reduced by using a model of the exhaust gas temperature as is done in Sec. 7.2.

4.6 Summary

A physics-based method of estimating the trapped residual mass in a recompression engine using in-cylinder pressure and exhaust temperature measurements has been developed and evaluated through dynamic analysis and experiments. The algorithm is viable for real-time implementation on embedded hardware and can be used across a wide range of engine operating conditions with minimal losses in accuracy over offline analysis.

An accurate estimation of residual mass is important to understand and control HCCI dynamics due to its sensitivity to thermal properties of the charge mass. It has been shown that the estimation is effective at capturing the cyclic trends of highly variable data sets. Furthermore, an analysis has been done to show sensitivity properties to measurement errors and a tuning parameter.

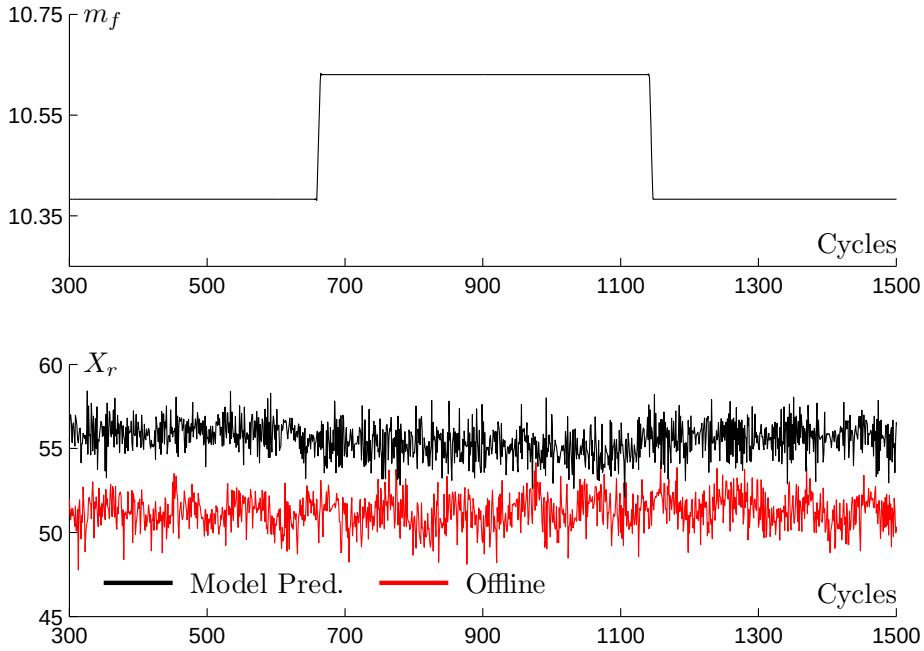

Figure 4.11: A fuel mass step for cylinder 1. The online residual gas fraction prediction (black) is compared against the offline prediction (red). The cycle-by-cycle predictions are good throughout the test however there is an offset in the mean value most likely caused by the exhaust gas temperature sensor.

A limitation of the algorithm is that it requires a transient air mass as an input. In the experiments presented here the air mass was found using a manifold filling dynamics and cylinder filling model on the Bosch Motronic ECU. The results from the residual estimation are most sensitive to errors in this input as indicated by Fig. 4.4 and so it is imperative that a well parameterized model is used. In Chapter 7 a model of the exhaust gas temperature is used in place of the measurement, this creates a three state model for the determination of both the residual gas fraction and the combustion phasing. An adaptive parameter estimation scheme is also used to correct for modeling and measurement errors.

Chapter 5

Quantification and Modeling of Cyclic Variability

5.1 Introduction

HCCI faces difficulties in the form of instability at the edges of its operational limits. This makes its effective operating region smaller and transients, such as load transitions, difficult. An example of the suitable operating region of HCCI is given in Fig. 5.1. The data in this plot is achieved through an SOI sweep at several loads. EVC was adjusted at each point to obtain the region of SOI with maximum authority. The figure shows that the acceptable load and combustion phasing region are severely limited in HCCI. Specifically as we progress upwards in load the onset of CV creates a boundary on combustion phasing on one side while while high pressure rise rates and excessive ringing limit the other. These boundaries eventually converge creating a high load limit. These same limits can be seen through the return map in Fig. 5.1. This figure shows the progression of combustion behavior from high CV in blue to high ringing in red. This was achieved by sweeping the EVC position such that progressively more and more residual mass is trapped, this advances the mean combustion phasing. Additionally, the same data from the return map in Fig. 5.1 is provided in Fig. 5.2. The effect of the onset of CV due combustion phasing is profound. As the mean combustion phasing retards the dispersion of efficiencies increases and lowers, on average, for sufficiently late combustion.

Three modes of instability will be considered in the following sections through experimental observations and analysis. The first is referred to as a throttled stoichiometric transition. This type of CV can be encountered when making as switch between SI and HCCI, which is one method for extending the operating region of the engine as demonstrated in [76]. The second mode is referred to as thermal run-away which is a phenomenon that is characterized by progressively earlier combustion over

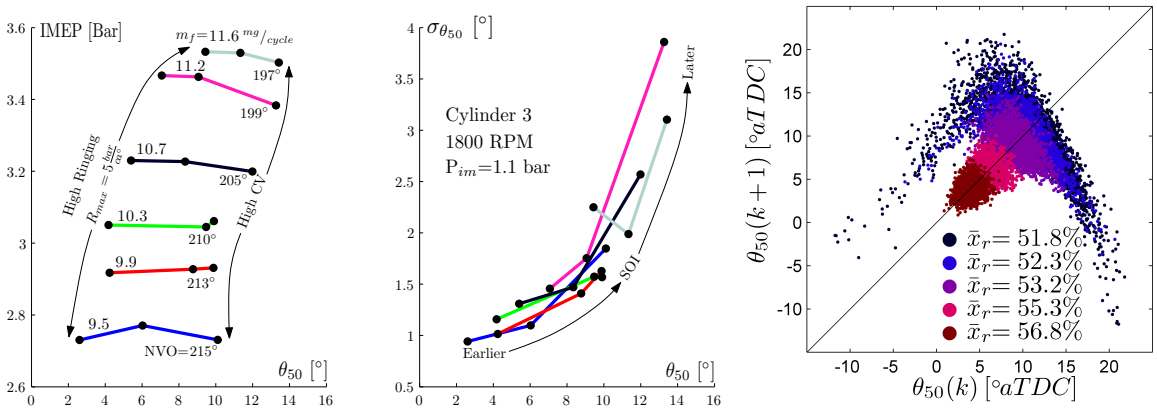

Figure 5.1: Limits of the HCCI combustion operating region (left) are shown through sweeps of SOI at several loads. The combustion is limited by late phasing variability. The onset of combustion phasing variability is also seen (right) through the use of a return map. The cycles progress from late phasing CV in dark blue to high ringing variability in red. The data was achieved through a sweep of EVC.

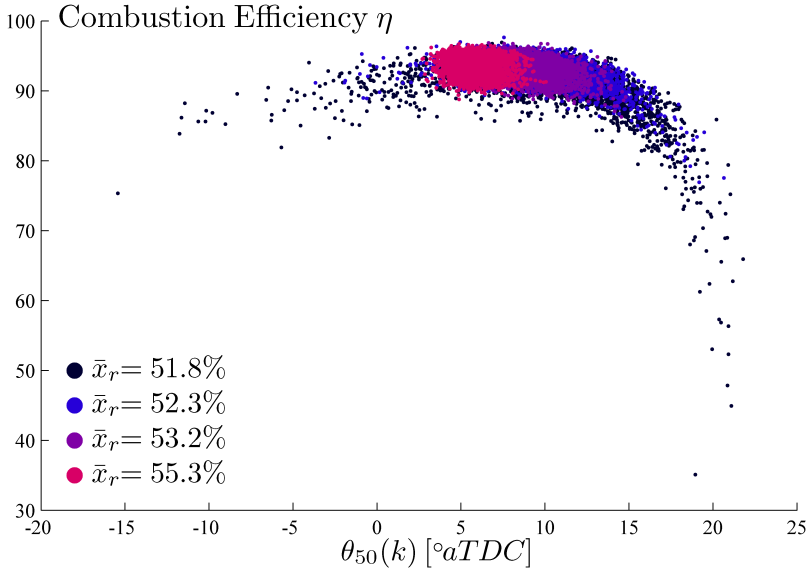

Figure 5.2: Effect of different level of CV on combustion efficiency. The progression is achieved through a change in the average residual gas fraction. It is observed that the combustion efficiency falls off sharply for late combustion.

the course of many cycles. The last mode occurs when operating lean and at late combustion phasings. This is a method that could be used to extend the load range of HCCI by running higher loads at later phasings to avoid pressure rise rate limits. This is a similar idea to work done in [77, 78] where extension of the low load limit was the focus. While running higher loads at later phasings is a viable solution to the problem, oscillatory behavior is introduced at these conditions as shown in [14, 79].

Each mode has different dynamic behavior associated with it and it will be shown that these dynamics have dominating deterministic features. This is an important realization to make as it indicates that the dynamics can be modeled as will be shown in Sec. 5.5 for lean-late phasing combustion. For all tests presented here, large data sets were used, usually consisting of 3000 engine cycles per test. This is done to ensure statistical relevance in the data since some patterns only become evident over long periods of time.

5.2 Throttled Stoichiometric

Throttled Stoichiometric HCCI combustion can be encountered during mode transitions between HCCI and SI combustion. A smooth transition from HCCI, with lean mixture, to SI, with stoichiometric mixture, requires maintaining torque with low variability while reducing the air-fuel ratio. The dynamics in the air path are slower than the combustion process and it is therefore desirable to, in a transient, operate HCCI combustion throttled and closer to stoichiometry than in the normal operating range. Moreover, the reduction in air mass when closing the throttle can be counteracted by reducing the NVO. Reduction of the residual gas fraction lowers the temperature at intake valve closing and retards the combustion phasing which can induce variability as shown in [19, 18]. This type of transition would be necessary for implementation of the HCCI combustion mode into production vehicles because HCCI alone can not satisfy the the load range associated with modern driving cycles. Because HCCI and SI combustion are inherently different, the transition can be highly variable as demonstrated in [20, 21, 80].

To explore this limit of operation, the throttle angle was gradually reduced while maintaining stoichiometry, as indicated by the exhaust lambda sensor, by compensating through reduced NVO. When the variability, in terms of coefficient of variation (CoV) of IMEP, passed the acceptable limit of 5% all actuators were held constant and the measurements were recorded. The engine was run in open-loop except for

regulation of engine speed and coolant. This level of CoV corresponded to a 25% throttle angle and an NVO of 144°, the result of which is a residual gas fraction of approximately 44%. Boost pressure before the throttle was 1.39 bar while the intake and exhaust manifold pressure were at 1.05 and 1.44 bar, respectively.

Observations from these experiments and the analysis of the results collectively show that unburned fuel carries over to the NVO period and to the next cycle. The effects are heat release during NVO and higher than normal heat release during main combustion. The analysis quantifies these effects by estimating the unburned fuel amount and the combustion efficiencies. The pressure data for 3000 cycles in two op-

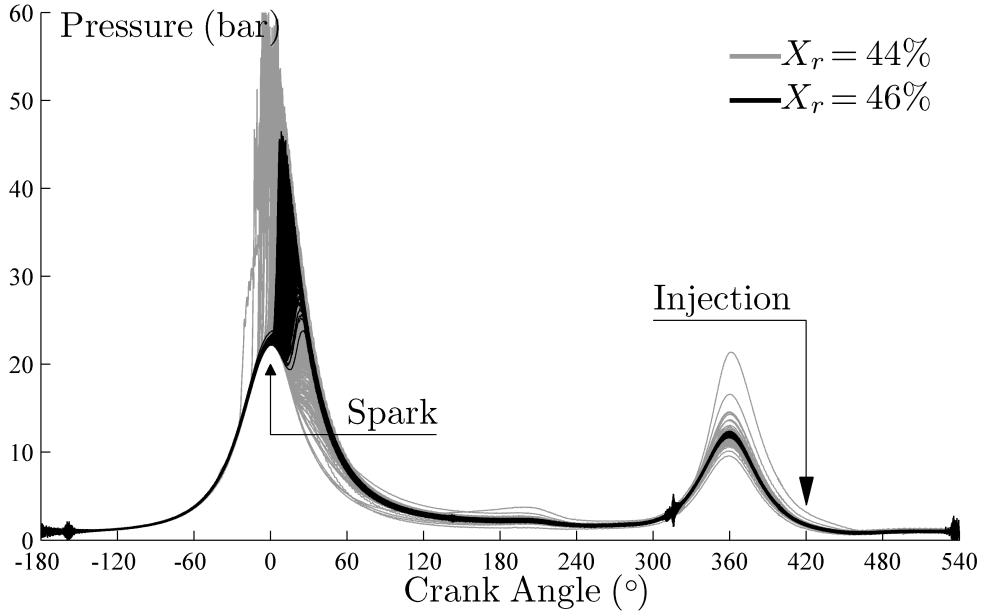

Figure 5.3: Raw pressure data. The large difference in variation from cycles in black to those in gray is due to a small change in x_r. There are large pressure rises during the NVO which occur before the injection of fuel. This indicates the presence of unburned fuel.

erating points is shown in Fig. 5.3. The operating conditions in Fig. 5.3 are different with respect to x_r. This difference arises from a change in throttle and NVO. The points in black are throttled to 30% while gray are at 25%. As the throttle percentage is increased the NVO also increases to maintain stoichiometry and as a result x_r is raised. Cycles in black have a slightly higher x_r than those in gray and are considered normal burns. As can be seen in Fig. 5.3 when x_r is lowered slightly the data becomes highly variable. In addition, for some cycles in gray, a significant pressure rise during NVO can be observed. The cycles in gray will be the focus of this section.

In conjunction, Fig. 5.4 shows the gross heat release and cylinder temperatures

for the two different levels of x_r. It can be seen that cycles which have low burns during main combustion tend to have a noticeable heat release during NVO. The corresponding temperatures are also high.

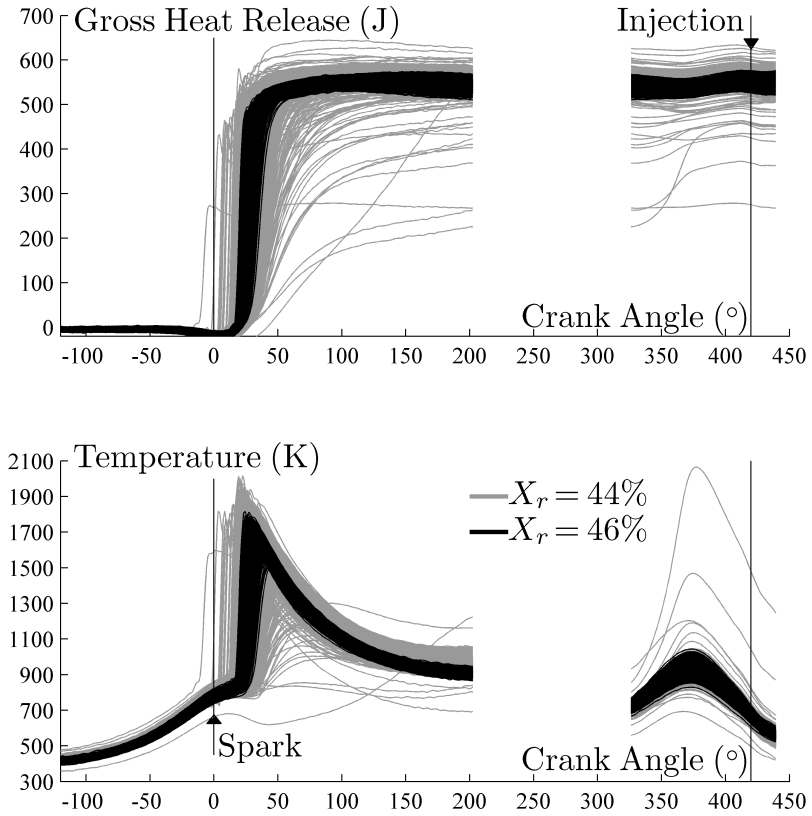

Figure 5.4: Variation in heat release (top) and in-cyolinder temperature (bottom) due to a small change in x_r. As the residual gas fraction is reduced the combustion becomes highly variable as indicated by the cycles in grey.

5.2.1 Cycle-to-cycle dynamics

To understand the cycle-to-cycle behavior further, 16 cycles are observed in detail through an illustrative progression in Figs. 5.5–5.9. First, Fig. 5.5 shows both the evolution of cylinder pressure and temperature. The cycles highlighted in black, corresponding to cycles 4 and 11, are points with low heat release. Leading up to these cycles the peak pressures drop as do the temperatures. Consequently, cycles 4 and 11 exhibit a large temperature and pressure rise during the NVO period. It will be shown that this is result of unburned fuel. These cycles can be observed in Fig. 5.6 through a plot of combustion phasing versus efficiency. Cycles 1–3 maintain a relatively constant efficiency while phasing retards. This is followed by a rapid decline

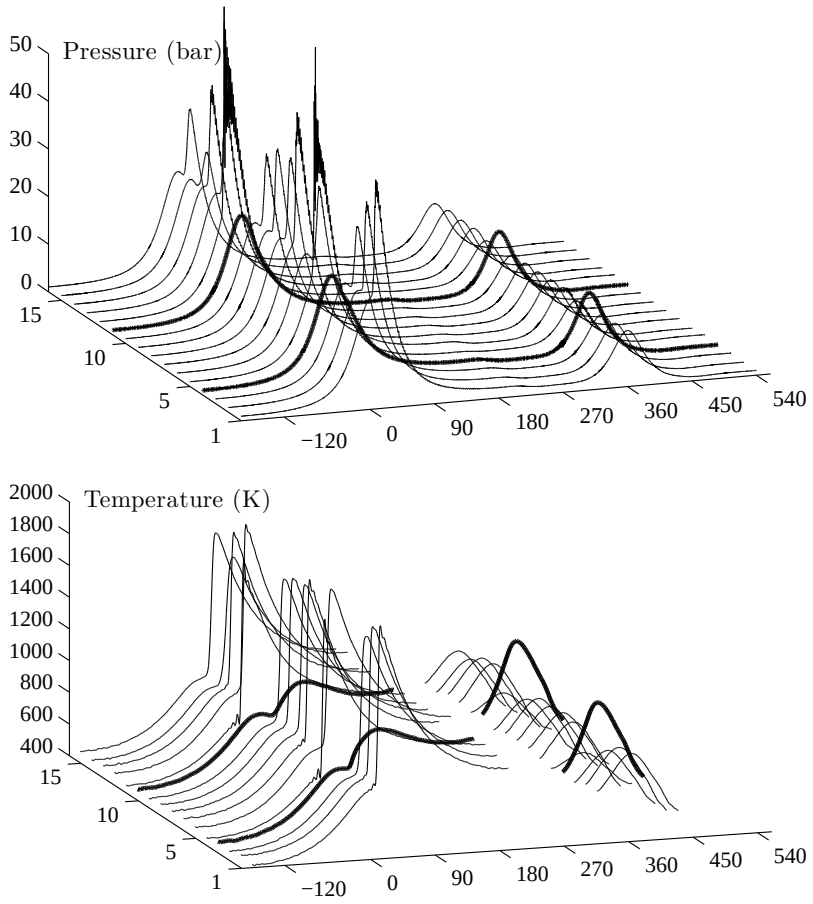

Figure 5.5: Pressure (top) and temperature (bottom) for a sequence of cycles. The drop in peak pressure can be seen proceeding the bolded cycle which is close to a misfire. The sequence of cycles then recovers and repeats.

in efficiency in cycle 4 and then a moderately low efficiency in cycle 5 which has a 50% burn angle before TDC. The system then exhibits a very large burn and high efficiency at cycle 6 and returns to normal combustion in cycle 7. The rest of the cycles in this series are shown in light gray. An operating point with the same actuator settings, but with spark at 25° aTDC, is in dark gray.

It should be noted that cycles with low efficiencies on the left hand side of Fig. 5.6 are preceded by the cycles with the latest combustion phasing on the right hand side of the return map in Fig. 5.9. This shows that the heat release during NVO is affecting the temperature and pressure at IVC in the next cycle. Additionally it is possible that heat transfer is higher at these early phasings due to high ringing and turbulence. As a result these cycles may have a slightly higher efficiency than indicated in Fig. 5.6 due to underrepresented heat losses in the analysis. However,

the last cycle in these sequences, see cycle 6 and 13 in Fig. 5.7, has a higher than average heat release indicating unburned fuel from previous cycles.

When phasing is later the efficiency curve drops once again. This is explored in detail in [81, 82] where lean HCCI without the presence of spark is the topic of interest. However, when a comparison of the efficiencies is made between that of [82] and Fig. 5.6 one can notice that the spark improves the combustion efficiency of the cycles with late phasing by making their burns more complete. Figure 5.6 further demonstrates this for stoichiometric conditions. When the spark is advanced, as represented by the data in dark gray, there is a smaller variability and the peak efficiency is lower than that of the data with spark at TDC, shown in light gray. The progression of

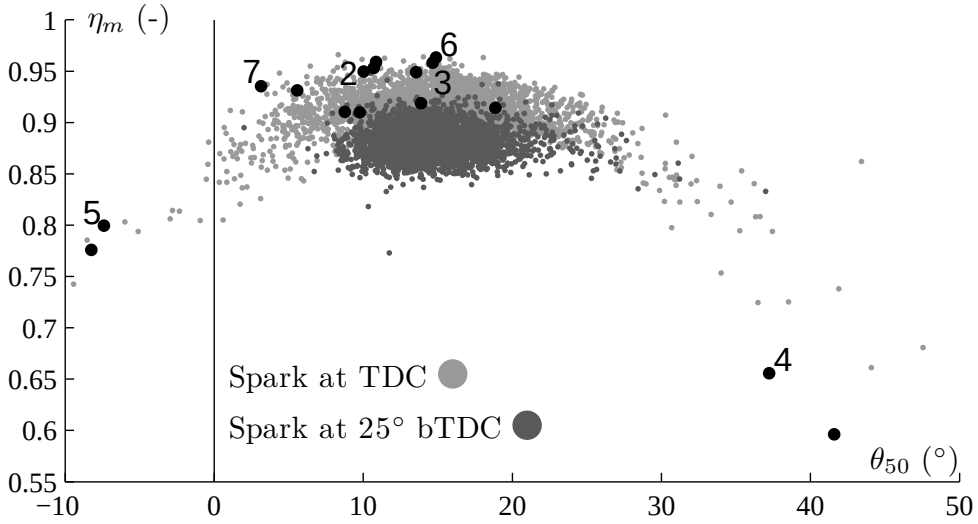

Figure 5.6: Estimated efficiency for main combustion for operation with spark at TDC and 25° bTDC. The marked cycles corresponding with the cycles of Fig. 5.5–5.8.

events is more clearly revealed in the consecutive heat releases of Fig. 5.7 and the trends of combustion phasing, IMEP and unburned fuel in Fig. 5.8. It should be noted that the amount of unburned fuel in Fig. 5.8 is the amount of extra fuel present at the beginning of each cycle. Here we see that cycles 1–3 maintain a relatively constant IMEP however combustion phasing gradually shifts later until cycle 4 which is so late that the burn is very slow and little heat is released. This is most likely caused by the spark igniting the mixture rather than pure auto-ignition. Because cycle 4 is so poor a significant portion of the fuel is left unburned through main and NVO heat release, it is then carried over to cycle 5. This extra fuel accompanied by a high temperature at IVC, caused by the heat release during NVO of the previous cycle (4), results in a very rapid, and early, auto-ignition with a low combustion efficiency as indicated

by Fig. 5.6 and a high ringing index as can be seen by the very large pressure spike, followed by oscillations, in Fig. 5.5. In addition, cycle 5's combustion appears to stop and is followed by a slow burn, initiated after the spark at TDC. Because of the low efficiency of this burn even more fuel is left unburned, as seen in Fig. 5.8, and carried over to the next cycle (6). However, cycle 5's conditions were not sufficient for NVO heat release, in fact there was very little temperature rise during NVO as seen in Fig. 5.5. As a result, cycle 6 once again behaves like normal HCCI combustion, however the build up of unburned fuel from the previous two cycles causes it to have a higher than normal heat release. Finally the system returns to HCCI combustion with the expected release of energy in cycle 7. Cycles 8 through 16 exhibit a similar sequence of events.

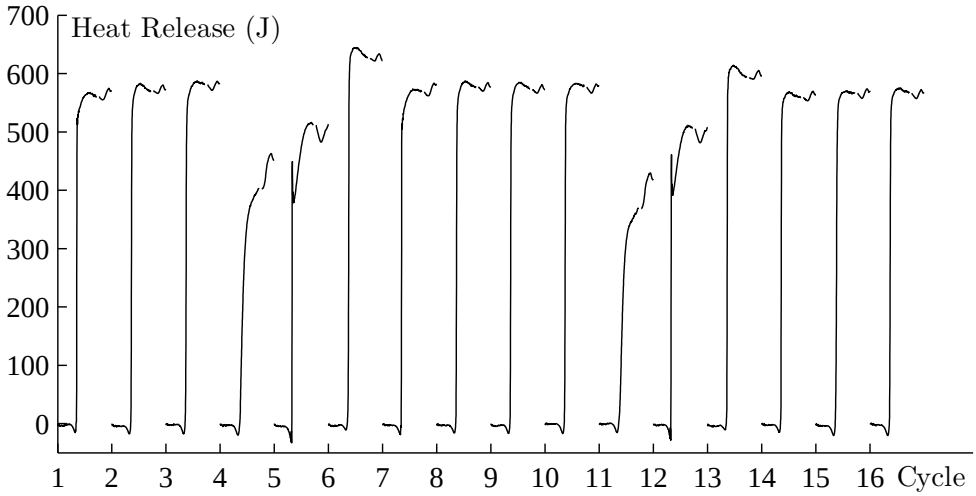

Figure 5.7: Progression of abnormal cycles as seen by the variation in consecutive heat release during main and NVO.

5.2.2 Return Maps

To understand the cycle-to-cycle dynamics further the data set can be viewed from the perspective of return maps. Such maps show the relationships between consecutive cycles and give insights about the dynamical coupling between cycles [83]. For example, in combustion with low variability the combustion phasing θ_{50} in cycle k and $k+1$ do not differ significantly from each other, the value of θ_{50} always returns to a similar value, and the points in the return map remain close to the diagonal. Figure 5.9 contains the return maps of heat release and combustion phasing as deter-

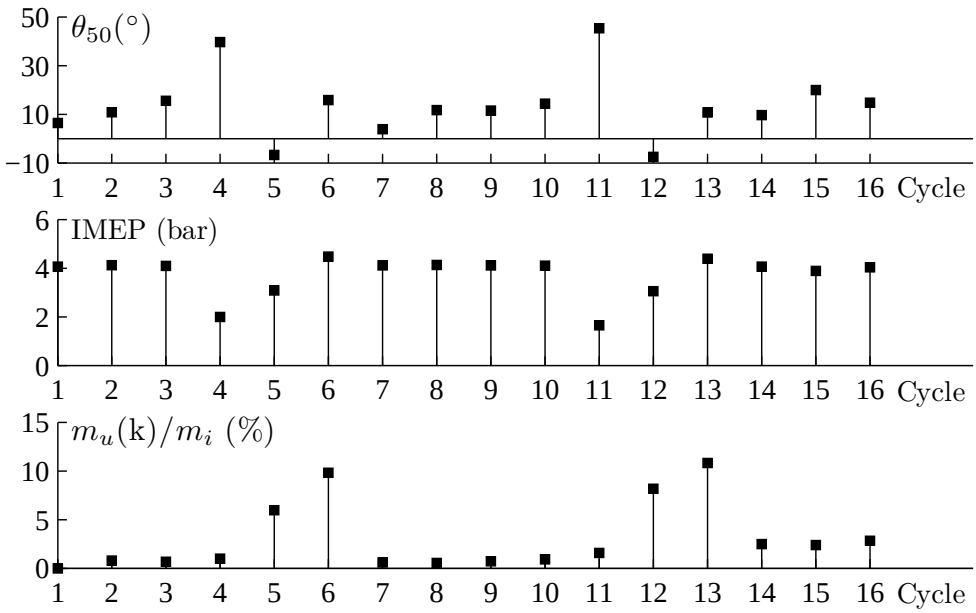

Figure 5.8: Progression of abnormal cycles in terms of combustion phasing (top), IMEP (middle) and residual fuel (bottom).

mined from the data analysis. Clear patterns emerge in the form of legs indicating a deterministic coupling between cycles. The vertical legs here correspond to an instability; they show that an average value for cycle (k) can result in an abnormal value in cycle (k+1). For example, if a cycle has a low heat release, a series of cycles which follow the dynamic behavior described by the orientation of the legs in the return maps is the result. Since the engine is operating close to the stability limit small perturbations in the system can cause such a scenario to occur.

Figure 5.9 shows the cycles as they progress through the return map legs. One can see in the map of combustion phasing that as we move from 1–2–3 the phasing walks up the diagonal becoming later and later. However, when following these same cycles in Fig. 5.6 we see that the efficiency remains at nearly the same level. As this phasing becomes later the charge temperature at IVC drops, causing the combustion to enter a region where oscillatory behavior is possible and can be induced by random perturbations to the system. The third cycles' late phasing and high efficiency lead to cycle 4 which is extremely retarded and with very little heat released. The following cycles are a recovery from this poor burn. It is this series of cycles which defines the deterministic shapes of the return maps.

The heat release patterns that emerge from Fig. 5.9 share many resemblances with those presented in [80, 21, 22] where a single cylinder engine was used. These

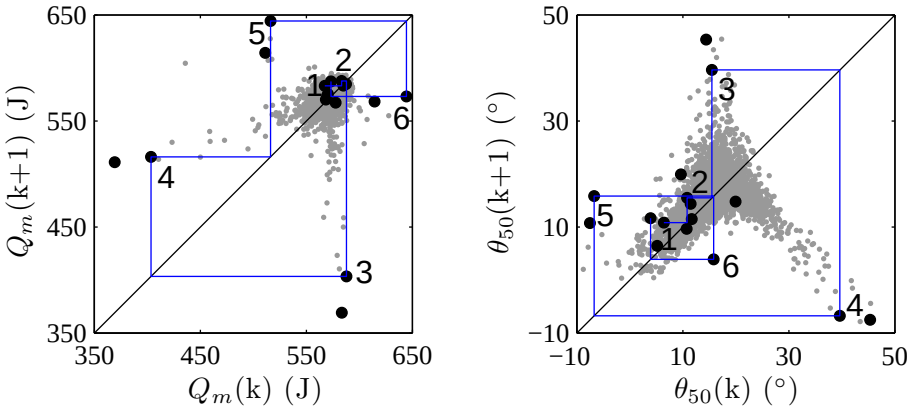

Figure 5.9: Return maps of heat release (left) and combustion phasing (right). Consecutive cycles shown correspond to those of Fig. 5.8

experiments were also run at stoichiometry and with NVO. Despite a change in the engine platform, the deterministic patterns are similar. However, when a comparison is made with results for lean operation in [19, 18] one can see that the shapes do not resemble those of Fig. 5.9 indicating a different non-linear behavior for lean versus stoichiometric HCCI.

5.3 Thermal Runaway

The other limiting factor on the speed-load operation map of HCCI is the ringing limit. This occurs when the pressure rise rate due to combustion is so high that the mechanical limits of the engine may be exceeded. This is often referred to as ringing and has similar detrimental effects to knocking in an SI engine.

At specific conditions associated with ringing, namely high-speed high-load, HCCI exhibits a particularly interesting phenomenon which will be referred to as a thermal runaway event. While this phenomenon is a relatively new area of study, an attempt will be made here to explain what this process is and how it works qualitatively. Thermal runaway tends to occur when operating at the load limit of HCCI combustion where, as stated previously, pressure rise rates are high. It is therefore desired to retard the combustion phasing to lower the stress on the cylinder. When the combustion phasing is made progressively later at high load and speed the onset of thermal runaway occurs.

To study this behavior, the engine was pushed to the load limit for a particular operating condition and the amount of NVO was reduced to retard the combustion

phasing. The result of this process can be seen in the time series combustion phasing data in Fig. 5.10. In the first 1500 cycles the combustion is mostly noise, and some early autoignition events can be seen but they tend to be erratic. However, after 1500 cycles, when the amount of NVO is reduced, it is obvious that the behavior changes.

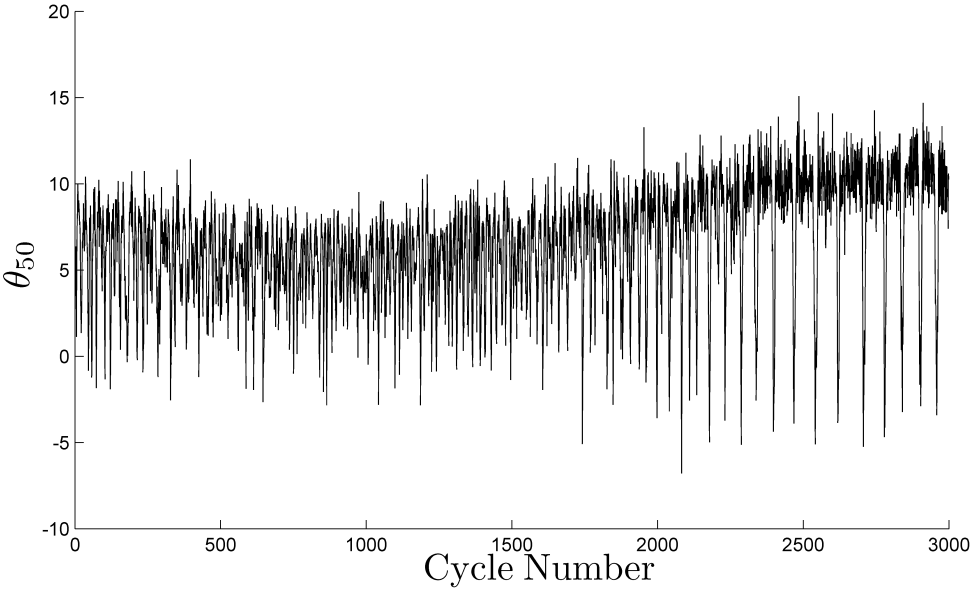

Figure 5.10: Time series data showing the onset of thermal runaway behavior after 1500 cycles. Note the change in mean combustion phasing.

In Fig. 5.11 we have the return maps of combustion phasing and heat release. As opposed to the other CV cases studied in this paper, where there are extensions perpendicular to the diagonal ($x(k) = x(k+1)$), this process exhibits dynamics that stretch the return map of combustion phasing down the diagonal. In contrast, the return map for heat release reveals no deterministic features at all. In the figure a sequence of cycles is highlighted which correspond to one of the large spikes in combustion phasing which occurred after 1500 cycles in Fig. 5.10. It is interesting to note the number of cycles which make up these thermal events, on average it takes 20 cycles to reach the earliest phasing and return to normal combustion. The normal combustion then continues for approximately 50 cycles and then another thermal event is encountered.

While it is not clear how exactly this process evolves there is a hypothesis. Because the combustion is pushed later to avoid excessive pressure rise rates, it is possible that the combustion efficiency also declines as can be seen in Fig. 5.16. This, in conjunction with the strong internal feedback of the trapped residuals, could lead to the build up of unburned fuel in the cylinder due to incomplete combustion. This hypothesis is

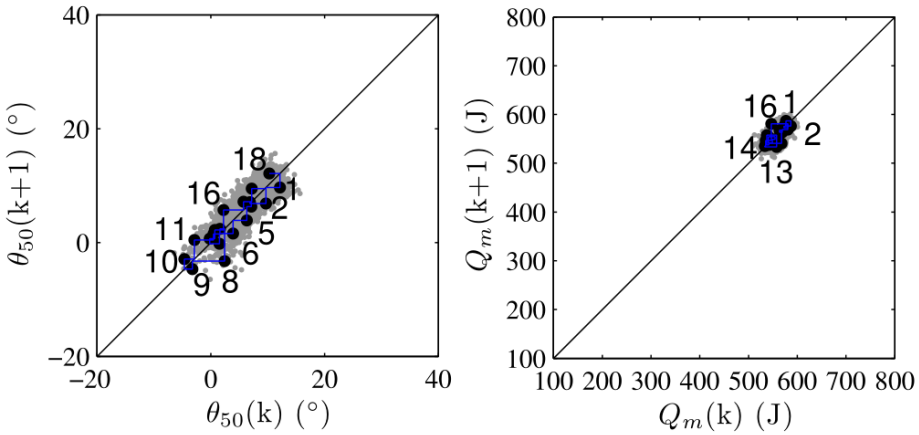

Figure 5.11: Return maps of combustion phasing (top) and gross heat release (bottom) showing the progression of a thermal runaway event.

supported through the results in Fig. 5.12. Here we examine the last 250 cycles of the data in Fig. 5.10 in more detail. The progressions of 4 thermal runaway events are highlighted here and it can be seen that the combustion has an uncharacteristically low efficiency. Based on the analysis in the previous sections this tells us that there should be residual fuel building up in the cylinder or that it is burning during NVO. While the results are noisy, one can notice that the peak temperatures in NVO do tend to increase for the runaway events, during this time the nominal residual fuel depletes even though the efficiency also appears to go down (this may be due to increased heat transfer associated with the ringing). There are also obvious fluctuations in the torque as seen by the IMEP. The excess fuel could be partially burning during NVO causing the pressure and temperature to rise at IVC which results in progressively earlier and earlier combustion. The fact that it returns to normal phasing in a similar manner (over several cycles) is somewhat puzzling however. The long time constant of the run away event points to slower dynamical phenomenon dominating the behavior once it begins, for instance changes is intake air or coolant temperature or heat transfer.

Another unknown about this process is what initiates it. Hypotheses include crossing an energy threshold, possibly temperature in NVO, which allows the unburned fuel to burn. Or it could be oil droplets causing hot spots in the combustion chamber, this could also be true for coke or soot flaking off, similar to many leading justifications for superknock. This is an area of research which requires more effort to develop a full understanding. Perhaps imaging of the process could be helpful to develop a better understanding.

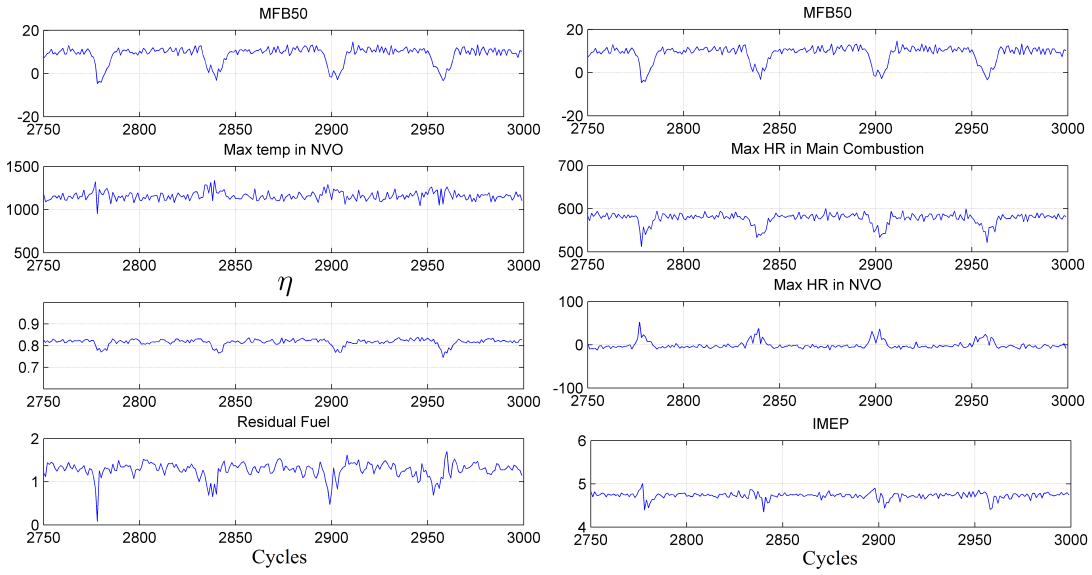

Figure 5.12: The response of combustion phasing, maximum temperature in NVO, the combustion phasing, residual fuel and torque (top to bottom,respectively) to several thermal runaway events.

5.4 Lean–Late Phasing

In lean HCCI there are two main limits of operation in the speed-load map, the ringing limit and the late phasing variability limit as shown in Fig. 5.1. This section focuses on the late phasing limit which has been explored previously by several groups working on HCCI combustion through both simulation and experiments. Specifically, in [14] simulation showed that there is a strong coupling of consecutive cycles due to recycled thermal energy. The important addition of the effects of recycled chemical energy was introduced through simulations of chemical kinetics with 31 species in [15] and reduced to an eight state model in [16]. A control oriented, 4 state, model was developed in [17] where fuel was one of the states. Experiments for lean HCCI were studied and modeled with two states in [18, 19]. One of the states in these works is the unburned fuel mass that couples the cycle-to-cycle behavior. This state sheds light on the chemical energy coupling and the dynamical patterns emerging in both the main and recompression events at the limits of the HCCI stability region.

To explore the late phasing variability limit, experiments were performed at a constant speed of 1800 rpm and a load of 3.25bar net IMEP. By varying the amount of NVO, and consequently the trapped residual mass, it was possible to observe its effect on the onset of CV. Two operating conditions (two NVO/x_r amounts) were studied to demonstrate the onset of lean-late phasing combustion variability. The

cycle evolution is analyzed using return maps, as was used to study the throttled stoichiometric and thermal runaway, as well as symbol statistics. These mathematical tools provide a systematic method to discover dynamic interactions and reveal unstable behavior in phasing and heat release.

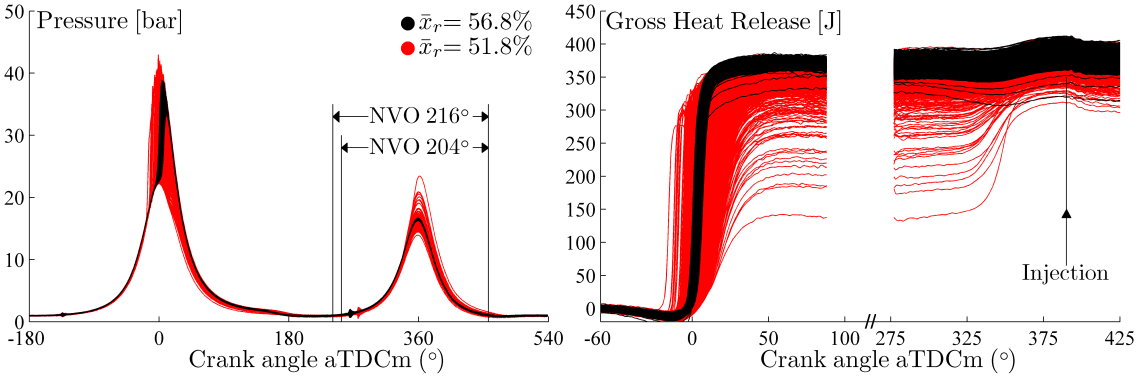

Figure 5.13: Pressure and gross heat release traces for high (red) and low CV (black). The operating conditions differ only by a slight change in the residual gas fraction, however the change in combustion stability is very large.

The first operating condition, seen in Fig. 5.13, has an NVO of 216° and acceptable CV while the second condition has an NVO of 204° and high CV. These operating conditions correspond to the data in Figs. 5.1 and 5.2. With the smaller NVO the residual gas fraction decreases 5% for all cylinders and λ, measured with one sensor in the exhaust, increases. The standard deviation $\sigma_{\theta_{50}^m}$ and the CoV of IMEP increase notably. It is obvious that reducing the NVO increases the CV. The increased variability can be seen in the spread of the observed peak pressures and pressure rise rates during main combustion. In the NVO period there are significant cumulative heat releases for cycles which have poor burns during main combustion. Specifically, cycles with a low accumulated heat release during main combustion are followed by a noticeable heat release during re-compression with a relatively slow burn rate. These observations suggest that there is unburned fuel that produces heat release during recompression and also that unburned fuel may carry over and release heat in the next main combustion event. The level of CV differs between the cylinders however to study the effects of CV and the cyclic coupling of unburned fuel in detail, the third cylinder, with the highest $\sigma_{\theta_{50}^m}$, is studied in the remaining sections.

5.4.1 Return Maps

When the data in red from Fig. 5.13 is viewed through the return maps of combustion phasing and heat release in Fig. 5.14 it becomes clear that deterministic features are present in late phasing HCCI as the patterns that emerge are pronounced with high CV. The main characteristics of the return map of combustion phasing are described by a cluster of cycles stretching out perpendicular to the diagonal and another part bending to the left and extending down parallel to the diagonal. This asymmetric pattern implies that the evolution of θ_{50}^m could be due to nonlinear dynamics, non-Gaussian noise or a combination of both. The perpendicular part indicates an unstable behavior in the form of oscillations where θ_{50}^m alternates between early and late phasing. The oscillations can have a large amplitude as shown by the dispersion and magnitude of the leg perpendicular to the diagonal. This portion of the map together with the left leg shows that there is a limit for the amplitude of oscillations. When the amplitude is sufficiently large the combustion recovers to a phasing closer to the average. This is however only a temporary recovery as a slight perturbation after the recovery will push the system back into an oscillatory regime. A sequence of cycles is marked in Fig. 5.14 as 0-6 and is an example of an increasing amplitude oscillation followed by a recovery to a nominal phasing. This sequence of cycles will be studied in further detail in Sec. 5.4.2.

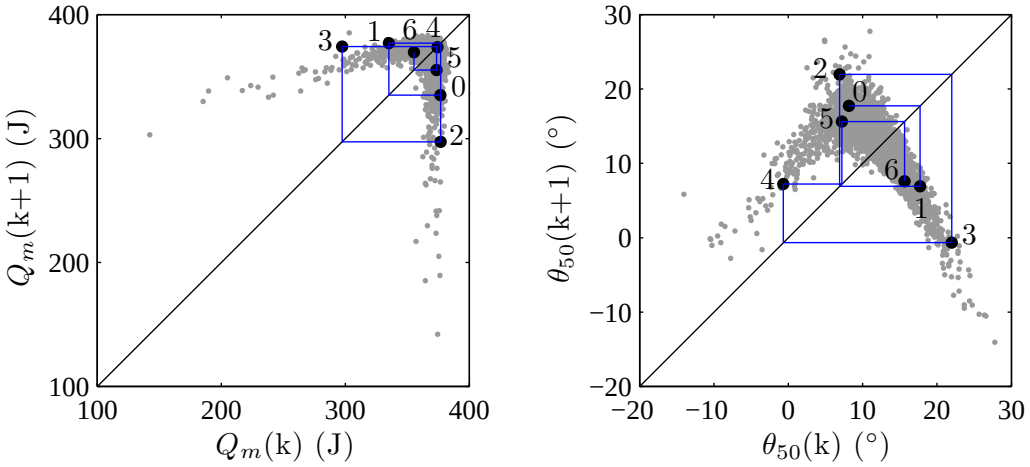

Figure 5.14: Return maps of heat release (left) and combustion phasing (right) for lean-late phasing combustion. The legs stretching out perpendicular to the diagonal in the combustion phasing plot indicate oscillatory dynamics. The progression of a sequence of cycles is highlighted in blue.

5.4.2 Cycle-to-Cycle Dynamics

Figure 5.15 shows a number of variables versus the combustion phasing during main compression, $\theta_{50}^{m}(k)$, these correlation plots allow us to see the trends which characterize the late phasing combustion. The first column shows the cumulative heat release during the main and NVO compression. Here we see opposite trends for the two plots, when combustion phasing is late there is less heat release in the main combustion but significantly more during NVO. Similarly, the second column shows that as combustion phasing becomes later, the exhaust temperature increases. This is the normal trend as the burned gases undergo less expansion and therefore less cooling before EVO for later combustion, however at a certain point this trend reverses and the exhaust temperatures fall rapidly due to incomplete combustion and lower peak cylinder temperatures. In concert, the temperature at IVO for late combustion increases due to the extra heat release during NVO. Finally the last column shows the return map of combustion phasing which was discussed in detail in Sec. 5.4.1 and the mass of unburned fuel as determined by Eq. (3.17). For later combustion the unburned fuel mass is increasing as expected based on the previous plots. Additionally, the unburned fuel is increasing for earlier combustion however this is most like due to underestimated heat release from an increase in turbulence when combustion is near TDC. The estimates of the unburned fuel mass suggest that not all of the remaining fuel is necessarily consumed during NVO and a fraction of it may carry over to the next cycle.

The labeled cycles in Fig. 5.14 are also marked in Fig. 5.15. This group of cycles is an example of the typical progression of events in lean late HCCI combustion. Cycle 0 starts at a normal combustion phasing however due to a random perturbation in the residual gas fraction the next cycle is late, marked by cycle number 1. This cycle lands on the the leg perpendicular to the diagonal indicating that we are in a region of oscillatory dynamics. Since cycle 1 is late we can see that the combustion efficiency is also low as shown in Fig. 5.16, which shows the main combustion efficiency η_m versus the main combustion phasing θ_{50}^{m}, and that the heat release during main combustion is low as well indicating that some fuel was left unburned. This is also reflected in the bottom right plot of Fig. 5.15. This figure shows the mass of fuel which is left unburned and carried over to the NVO region in light grey and the fuel that is left unburned for the next cycle in dark grey. It is clear that most of the fuel which is left unburned during main combustion is consumed during the NVO period. This causes an increase in the T_{ivo} temperature and cycle 2 to once again be early. Early combustion, as discussed earlier, however leaves more time for expansion and the

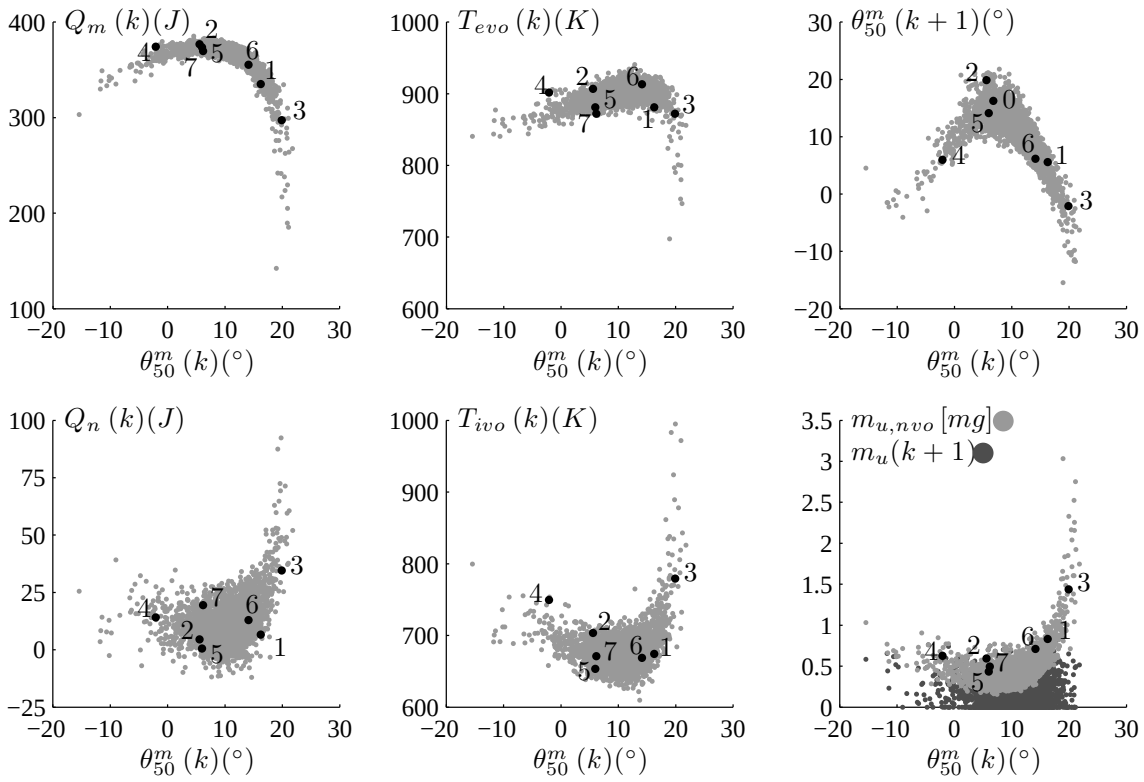

Figure 5.15: Combustion phasing during the main combustion event versus (left to right, top to bottom): Heat release during the main combustion, $Q_m(k)$, temperature at EVO, $T_{evo}(k)$, combustion phasing, $\theta_{50}^m(k+1)$, heat release during the NVO period, $Q_n(k)$, temperature at IVO, $T_{ivo}(k)$ and unburned fuel, $m_u(k+1)$ normalized by injected fuel.

intake temperature is once again low for cycle number 3. This cycle is very late and has a poor burn which leaves significant amounts of unburned fuel and consequently a large heat release in the NVO region, the end result is that the combustion of cycle 4 is early once again.

If the system had pure oscillatory dynamics this process would continue to repeat. However the engine would eventually misfire if it got to the point that no fuel burned during main combustion. This can sometimes be the case for operating points with excessive variability. However in this dataset the combustion recovers, this could be due to multiple effects such as engine inertia and torque output from other cylinders. The rise in the residual gas temperature from cycle 3 that caused the early combustion in cycle 4 is sufficiently large enough to be carried over to the next cycle. This is clear in the trend of T_{ivo} in Fig. 5.17 where it can be observed that the temperature in cycle 4 is significantly higher that cycles 0-2 but less than cycle 3. Additionally it can be seen that there was almost no heat release during NVO of cycle 4 and so

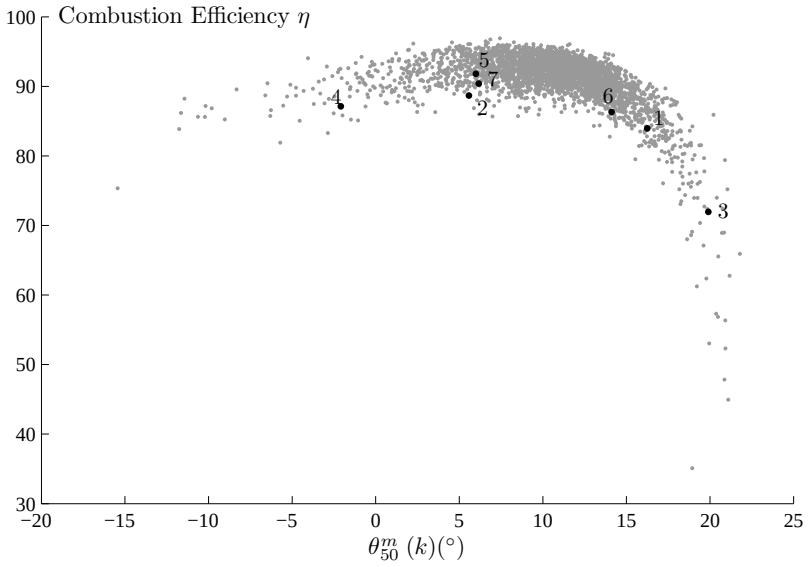

Figure 5.16: Combustion efficiency versus phasing for high CV. A significant drop off in efficiency is observed for late combustion.

the temperature rise of this magnitude cannot possibly come from NVO burn in this cycle alone. This increase in temperature at the start of cycle 5 allows the combustion phasing to be normal for a cycle which otherwise would have most likely been a misfire.

It should be noted that the efficiency η_m in Fig. 5.16 is computed from Eq. (3.15). The efficiency η_m decreases for both early and late combustion. As stated the low efficiency at early combustion phasings is most likely an artifact of insufficient heat transfer due to an increase in turbulence and ringing intensity which is not captured in the heat transfer model, which is the modified Woschni from [69]. The sharp drop in efficiency at very late phasing shows that the sensitivity with respect to phasing increases dramatically. Thus, the efficiency curve, which determines the unburned fuel mass after main combustion, is an important nonlinear relation for accurately describing the coupling between cycles.

5.5 Model for Late Phasing CV

A model for the lean-late phasing combustion variability has been developed based on the experimental observations in the preceding sections, specifically the evolution of the temperature and unburned fuel dynamics are of utmost importance. Additionally the model has been validated against experimental results.

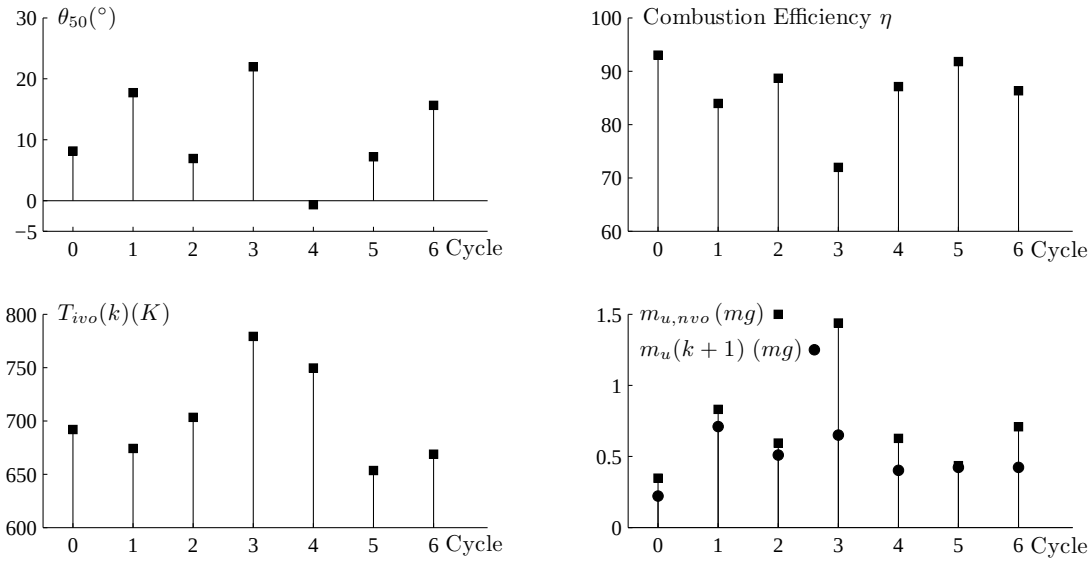

Figure 5.17: Time series data of combustion phasing, and efficiency (top row) as well as the residual gas temperature and mass of unburned fuel (bottom row)for highly variable data.

5.5.1 Model Derivation

The model is discrete time and has three states: the temperature at intake valve closing, $T_{ivc}(k)$, the mass of fuel, $m_f(k)$ which effectively capture the recycling of both thermal and chemical energy through re-compression of residual gases and an Arrhenius integral state to predict start of combustion. The output of the model is combustion angle of 50% burned, $\theta_{50}(k)$, while residual gas fraction, x_r, and mass of injected fuel, m_i, are inputs. Fuel injection timing is a controlled input, $u(k)$.

The complete model is given by:

$$\begin{cases} T_{ivc}(k+1) & = f_1(x(k), x_r(k)) \\ m_f(k+1) & = f_2(x(k), x_r(k), m_i(k)) \\ A(k+1) & = f_3(u(k)) \end{cases} \tag{5.1}$$

where $x(k)$ and $u(k)$ are the state vector and controlled input respectively. The model is explained in detail in [84] however derivations of the model equations are provided here.

Fuel Dynamics

The fuel mass at IVC on a particular cycle is composed of both the injected fuel quantity from the nvo period of the previous cycle and the mass of residual unburned fuel:

$$m_f(k) = m_f^{inj}(k-1) + m_u(k), \tag{5.2}$$

where m_u is the unburned fuel mass after both the main combustion and recompression periods. During the main combustion a fraction $\eta_m(k)$ of the charge is consumed by autoignition and then a portion of this charge is exhausted. The charge that is retained in the cylinder is $x_r(k)$, the trapped residual gas fraction. The amount of unburned fuel present at the start of the NVO region is then

$$m_f(k)(1-\eta_m(k))x_r(k), \tag{5.3}$$

where $m_f(k)$ is from Eq. 5.2. During the NVO period a fraction of the charge η_n is further consumed by some for of combustion if excess fuel is present. This efficiency is assumed to be a constant. Therefore the total mass of fuel carried over to the next cycle is given by

$$m_f(k+1) = m_f^{inj}(k) + x_r(k)(1-\eta_m(k))(1-\eta_n)m_f(k). \tag{5.4}$$

Combustion

The timing of the main combustion event is given by an Arrhenius integral expression:

$$\kappa(\theta_{soc}) = \int_{\theta_{ivc}}^{\theta_{soc}} \frac{d\theta}{Ap(\theta)^n exp(B/T(\theta))\omega} \tag{5.5}$$

where the parameters A, B and n are tuned based on steady state data. The values of $T(\theta)$ and $p(\theta)$ are provided by polytropic processes in the following sections. The engine speed is denoted by ω.

The end of combustion, θ_m, is dependent upon the start of combustion, θ_{soc}, and assumes an exponential burn duration

$$\begin{aligned} \theta_m(k) &= \theta_{soc}(k) + \Delta\theta(k) \\ &= \theta_{soc}(k) + d_0 \exp\left(\frac{\theta_{soc}(k) - d_1}{d_2}\right), \end{aligned} \tag{5.6}$$

where d_1 and d_2 are constants determined from data regressions. The burn duration differs from that presented in [84] where a linear relationship is used. The combustion phasing of 50% burned is then given by the relationship:

$$\theta_{50} = \theta_{soc} + \Delta\theta/2. \tag{5.7}$$

The temperature rise associated with burns during main and recompression are assumed to be instantaneous and occur at the end of combustion, $\theta_m(k)$ and $\theta_n(k)$, they are summarized by

$$\Delta T_m = \frac{Q_m}{c_v m_t}, \quad \Delta T_n = \frac{Q_n}{c_v m_t x_r} \tag{5.8}$$

where the total charge mass is m_t. The heat release during main combustion is

$$Q_n = m_f \eta_m(\theta_m) q_{lhv}(1-\epsilon). \tag{5.9}$$

The mass of fuel is as defined in Eq. (5.2) and the lower heating value of the fuel, q_{lhv}, is scaled by some heat loss ϵ. The combustion efficiency η_m is modeled by the sigmoid function

$$\eta_m(\theta_m) = e_1 \left(1 + \exp \frac{\theta_m - e_2}{e_3}\right)^{-1}. \tag{5.10}$$

This function effectively captures the key non-linearity of efficiency as a function of combustion phasing as in Fig. 5.16. Similarly the heat release during recompression is

$$Q_n = m_f(1 - \eta_m(\theta_m)) x_r \eta_n q_{lhv}(1-\epsilon) \tag{5.11}$$

where the combustion efficiency η_n is a constant.

Temperature Dynamics

At the time of IVO the residual mass mixes with the fresh air inducted during the intake stroke, if an adiabatic process is assumed the temperature at the end this mixing process can be written as

$$T_{ivc}(k+1) = (1 - x_r(k)) T_{im} + x_r(k) T_r(k) \tag{5.12}$$

where T_{im} is the temperature of the air in the intake manifold, this assumed to be constant for simplicity. The temperature of the residual gas T_r derived in the following section.

The temperature and pressure can be described by polytropic compression and expansion with the appropriate slope γ, the value of of p_x, T_x and V_x are the value of pressure temperature and volume respectively at a particular crank angle event θ_x. The temperature and pressure ($T_{am},\ p_{am}$) immediately after combustion can be defined by

$$T_{am} = T(\theta_m) + \Delta T_m, \quad p_{am} = p(\theta_m)\frac{T_{am}}{T(\theta_m)}, \tag{5.13}$$

where ΔT_m is given in Eq. (5.8). This temperature and pressure then follow a polytropic expansion down to EVO where an instantaneous blowdown process occurs and further expansion is applied down to the exhaust manifold pressure. The temperature after blowdown is

$$T_{bd} = T_{evo}\left(\frac{p_{em}}{p(\theta_{evo})}\right)^{1-1/\gamma}, \tag{5.14}$$

where p_{em} is the exhaust manifold pressure. To account for some heat loss of the residual the blowdown temperature is scaled by a constant c_e to give the temperature of the residuals at EVC,

$$T_{evc} = T_{bd}c_e. \tag{5.15}$$

Similarly the temperature rise to potential heat release during the recompression period can be modeled based on the result from Eq. (5.8). The temperature and pressure immediately following recompression combustion (θ_n) are

$$T_{an} = T(\theta_n) + \Delta T_n, \quad p_{an} = p(\theta_n)\frac{T_{an}}{T(\theta_n)}, \tag{5.16}$$

where $T(\theta_n)$ is found from a polytropic compression of T_{evc} up to θ_n. The residual gas temperature at IVO can then be found from polytropic expansion

$$T_r = T_{ivo} = T_{an}\left(\frac{V(\theta_n)}{V_{ivo}}\right)^{\gamma-1}. \tag{5.17}$$

To simplify the progression of expressions in this section, we can replace the charge mass with the ideal gas law,

$$m_t = \frac{p_{ivc}V_{ivc}}{RT_{ivc}}, \tag{5.18}$$

and and introduce the following parameters which lump constants and known param-

eters for a given operating condition:

$$\alpha = c_e \left(\frac{p_{em}}{p_{ivc}}\right)^{\frac{\gamma-1}{\gamma}} \left(\frac{V_{evc}}{V_{ivo}}\right)^{\gamma-1} \tag{5.19}$$

$$\beta = \frac{q_{lhv}(1-\epsilon)(\gamma-1)}{p_{ivc}V_{ivc}^{\gamma}} \tag{5.20}$$

$$\zeta = \frac{q_{lhv}\eta_n(1-\epsilon)(\gamma-1)}{p_{ivc}V_{ivc}V_{ivo}^{\gamma-1}} V(\theta_n)^{\gamma-1}. \tag{5.21}$$

The residual gas temperature at IVC can then be written as

$$T_r(k) = \left\{\alpha\left[1+\beta\eta_m(\theta_m)m_f(k)V(\theta_m)^{\gamma-1}\right]^{\frac{1}{\gamma}} + \zeta m_f(k)(1-\eta_m(\theta_m))\right\}T_{ivc}(k). \tag{5.22}$$

The parameters α is related to the engine breathing and the parameters β and ζ are correlated to the heat release due to combustion in the main and recompression events respectively.

Residual Gas Fraction

The average value of residual gas fraction $\bar{x}_r$ is directly controlled by the amount of NVO for a given operating point. However noise, disturbances and phenomenon such as turbulent flow create an experimentally observed distribution around the mean. The distribution is close to normally distributed with a standard deviation of about 0.8% and as such there is little correlation from one cycle to the next. Therefore the residual gas fraction is modeled as a constant $\bar{x}_r$ with Gaussian white noise,

$$x_r(k) = \bar{x}_r + e(k), \quad e(k) \in N(0,\sigma), \tag{5.23}$$

where $e(k)$ is a normally distributed signal with zero mean and variance σ^2.

5.5.2 Model Validation

Figure 5.18 provides an overview of the mode's structure, inputs and outputs as well as some experimental validation [18]. The results shown in this figure are for the same data presented in the preceding sections. The input to the model x_r shows the random dispersion from on cycle to the next for both high and low CV combustion. Model simulations are performed based on a mean residual gas fraction perturbed

by Guassian noise. The model predictions match the experiments well for both late and normal phasing conditions as seen by the figure on the bottom right hand side of Fig. 5.18. To the bottom left is the model output for a range of residual gas fractions with no noise. The result is a set of cascading period doubling bifurcations which eventually result in apparent chaos. In an actual engine this would simply be a misfire.

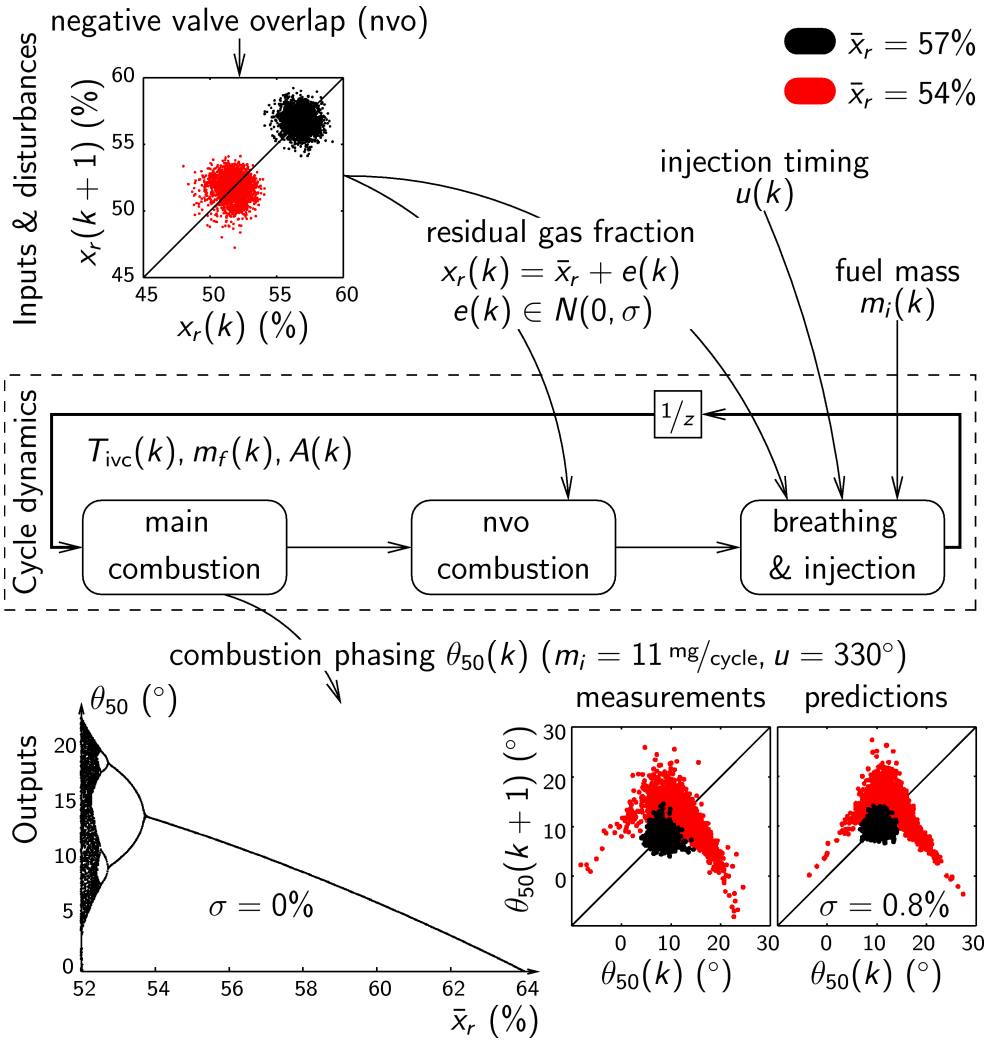

Figure 5.18: Model structure with inputs and outputs for lean late phasing HCCI combustion. Additionally, validation of the model predictions to experimental data are shown.

A pseudo root locus of the open loop model is provided in Fig. 5.19. The locus shows the location of the model's eigenvalues with respect to changes in the average residual gas fraction. Here we see that for low residual gas fraction there is an eigenvalue on the real axis in the left half plane, this indicates oscillatory dynamics. For

Table 5.1: Locations of eigenvalues μ for the linearized model.

$\bar{x}_r$	49%	53%	54%	55%
μ_1	-4.1	-1.3	-0.87	-0.48
μ_2	-0.071	-0.067	-0.074	-0.098

lower residual gas fractions this eigenvalue would eventually cross the unit circle resulting in unstable behavior. For higher residual gas fractions it can be seen that the poles cross over to the right half plane and one eigenvalue approaches an integrator, this would be representative of the thermal runaway behavior. The exact location of the eigenvalues in Fig. 5.19 is given in Tab. 5.1.

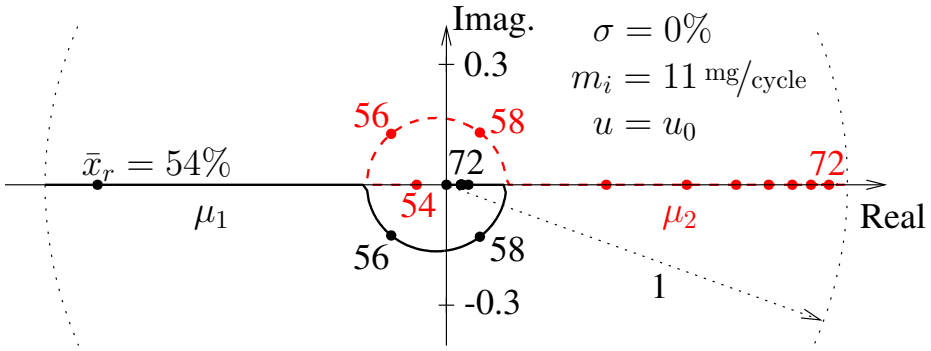

Figure 5.19: Location of the model's open loop eigenvalues for various levels of residual gas fraction. It is clear that for low residual gas fractions the model has oscillatory dynamics.

5.6 Summary

This chapter has provided insights to the dynamics of several modes of cyclic variability in HCCI through experimental results. The experiments consist of large data sets, an order of magnitude longer than is typically collected in literature, in order to study the trends of CV using statistical properties. It can be seen that deterministic pasterns emerge in these high variability cases, much of which has previously been considered seemingly chaotic. A common theme in all three modes is the presence of unburned fuel and the relationship between combustion phasing and efficiency. Quantification of these values has led to the formation of a model for lean-late phasing combustion.

The lean-late phasing model is simple (three states) and physics based. One of the states is that of the unburned fuel mass. This is a critical component as it adds the

dimension of recycled chemical energy to the understanding of HCCI dynamics. This state coupled with the recycled thermal energy and parameterized with engine data proves to be capable of reproducing the dynamics observed in high CV experiments. The model is validated by providing a mean residual gas fraction perturbed with Gaussian noise and observing the outputs of combustion phasing. As progressively lower residual gas fractions are input to the model the onset of CV is observed. The shape and distribution of combustion phasing return maps is captured well.

In the following chapter the model developed and validated here is used to design controllers to suppress the variability at the late phasing limit. The control is tuned based on the model prediction and the placement of closed loop poles. The control is then implemented on the engine for validation.

Chapter 6

Experimental Control of Cyclic Variability

6.1 Introduction

In order to demonstrate that the CV in HCCI combustion can be reduced to increase its usable operating map the model and control concepts developed in [18, 70, 84, 85] for lean, late phasing, high CV HCCI combustion with negative valve overlap (NVO) are applied through experiments on a four cylinder engine. The model captures both the recycled thermal and chemical energy through the residual gas fraction from one cycle to the next and has been shown to work on both single and multicylinder engines. Specifically, start of injection (SOI) timing is utilized as the control input to the system with combustion phasing for feedback. The use of SOI for combustion phasing control has been applied through experiments previously in [76, 86] where the objective was mode transitions and load extension respectively. In addition, the use of SOI to reduce CV was presented in [87] while control of CV using valve timings on a cycle-to-cycle basis with a fully flexible valve train was performed in [88, 89].

A key objective is to use SOI control to reduce the CV without shifting the mean phasing of the combustion. By maintaining the mean combustion phasing we enable the engine to run later and to better handle transients. To do so the controllers presented here are augmented with an integrator to ensure that they were operating at the same mean combustion phasing as open loop. The injection timing is a suitable actuator for this task because it offers good authority to control combustion phasing and can be easily manipulated on a cycle-by-cycle basis.

Two controllers were developed to the reduces the CV at late phasing based on simulations using the model in the previous section. One controller is a simple proportional controller while the other is an optimal Linear Quadratic Gaussian regulator (LQG). Both controllers were augmented with slow integral control so that the open

and closed loop conditions could be matched to draw a fair comparison. The design of the controllers is omitted but can be found in [90]. To test the effectiveness of the controllers described in the preceding sections they were implemented through rapid prototyping hardware coupled with the engine instrumentation, actuators and its engine control unit (ECU). The ECU calculated combustion phasing in real time based on net heat release analysis from the cylinder pressure transducers. This was then used for feedback.

The objectives of the tests were to demonstrate reduction of CV and to make comparison of the effectiveness of different control schemes on various levels of CV. To minimize variations in experiments due to environmental conditions the tests presented here were performed consecutively allowing a fair comparison of the results to be drawn. However, similar relative improvements were observed when repeating the tests on a day to day basis. The tests were run in open loop for approximately the first 1500 cycles while controllers were active for the remaining 1500 cycles.

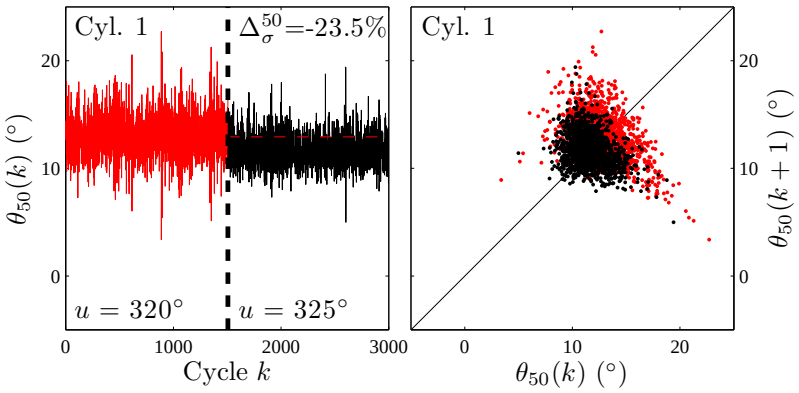

Figure 6.1: An earlier injection timing is an open loop solution to reducing combustion phasing variability as seen when comparing the data in red (high CV) to that in black (low CV). However the mean combustion phasing is not maintained and so this may not be a viable solution to mitigate CV in transients.

6.2 Proportional–Integral (PI) Control

Proportional control has been proposed to reduce oscillations in nonlinear systems with stochastic perturbations in the parameters [91]. For the system studied here, the nonlinear dynamics in (5.1) are governed by the thermal and the chemical coupling between cycles and there are random variations of the residual gas fraction [92]. The

proportional controller is

$$\delta u(k) = K_p(\theta_{50}(k) - \theta_{50}^*) \tag{6.1}$$

where θ_{50}^* is the desired reference combustion phasing. To find K_p, the eigenvalues of the linearized closed-loop model, given by Eq. (5.1) and (6.1), are studied for a range of K_p [84]. From the root locus of eigenvalues the gain $K_p = 1.0$ was chosen in order to stabilize the system and minimize oscillatory behavior. Integral action is introduced by adding the term

$$K_i \sum_k (\theta_{50}(k) - \theta_{50}^*)T(k) \tag{6.2}$$

to the controller (6.1) where $T(k) = 120/N(k)$ is the time for one engine cycle at the speed N rpm. The gain K_i is chosen to slowly reach steady state with a time constant of circa 100 cycles while not changing the transient response.

The performance for varying average residual gas fraction $\bar{x}_r$ is evaluated by computing the closed loop eigenvalues of the linearized model, Fig. 6.2 shows the result for cylinder 1. The value of θ_{50}^* is set corresponding to the nominal point for the open loop model. For $\bar{x}_r$ between 49% and 55%, the closed loop dynamics are oscillatory but (marginally) stable. Outside this range, the authority of SOI saturates and θ_{50}^* is not reached. The loci of the other cylinders suggests similar behavior.

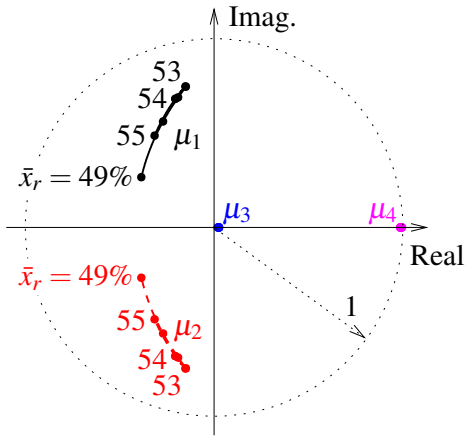

Figure 6.2: The root locus with proportional and integral control shows oscillatory but stable closed loop dynamics for a range of residual gas fraction $\bar{x}_r$. The open-loop eigenvalues in this range are shown in Tab. 5.1.

6.3 Linear Quadratic (LQ) Control

To improve the transient response over proportional control, an LQG design was performed based on the linearized model. The Kalman filter is designed by setting the noise variance to 1 and the state covariance matrix diagonal with the elements 100, 1, and 10. For the regulator, the criterion $\sum_{k=1}^{\infty}(10\delta\theta_{50}(k)^2 + \delta u(k)^2)$ is minimized. The resulting regulator is composed of two lag compensators and one pole and zero that nearly cancel and is thus reduced to one lag compensator without any appreciable change in the magnitude and phase for all frequencies of the closed loop system. The lag compensator stabilizes the system and to obtain zero steady-state error integral action is introduced by Eq. (6.2), which did not have a significant influence on the transient response. The final controller is

$$C(z) = -1.13\frac{(z-1.04)(z+0.054)}{(z-1)(z-0.49)}. \tag{6.3}$$

Analogous to Fig. 6.2, the closed loop dynamics of the controller for cylinder 1 (the other cylinders exhibit similar behavior) are shown in Fig. 6.3 for varying $\bar{x}_r$. The eigenvalue locations translate to oscillatory responses that are more damped than with proportional control if $\bar{x}_r$ is 50% or above.

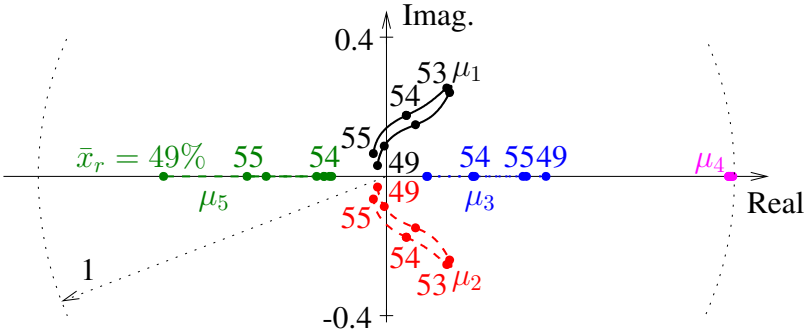

Figure 6.3: The root locus with state feedback control for a range of residual gas fraction $\bar{x}_r$. The open-loop eigenvalues in this range are shown in Tab. 5.1

6.3.1 Comparison of Controllers

Each controller was run at three different EVC positions, the result being three values of residual gas fraction and CV. The residual gas fractions span a range of approximately 1% and correspond to eigenvalues which are oscillatory in nature. A summary of the results can be found in Table 6.1. This table presents the mean combustion

phasing for open and closed loop, $\bar{\theta}_{50}^{\mathrm{OL}}$, $\bar{\theta}_{50}^{\mathrm{CL}}$, as well as the open loop standard deviation, $\sigma_{50}^{\mathrm{OL}}$, and the percent reduction of this standard deviation in closed loop, Δ_{σ}^{50}. For example, Table 6.1 for cylinder 1 and EVC=102.5° indicates that the percent reduction in standard deviation of θ_{50} from open loop using proportional control was Δ_{σ}^{50} =21.4%.

Table 6.1: Summary of proportional control (left) and state feedback control (right) of four cylinders with three levels of CV.

	Proportional				**State Feedback**			
	EVC = 102.5° aTDC							
Cyl	$\bar{\theta}_{50}^{\mathbf{OL}}$	$\bar{\theta}_{50}^{\mathbf{CL}}$	$\sigma_{50}^{\mathbf{OL}}$	$\Delta_{\sigma}^{\mathbf{50}}$	$\bar{\theta}_{50}^{\mathbf{OL}}$	$\bar{\theta}_{50}^{\mathbf{CL}}$	$\sigma_{50}^{\mathbf{OL}}$	$\Delta_{\sigma}^{\mathbf{50}}$
1	11.0	10.5	1.9	-21.4	10.5	10.5	1.7	-4.7
2	10.8	10.5	2.1	-24.8	10.2	10.5	1.6	-0.3
3	10.8	10.5	1.9	-10.6	10.4	10.5	1.7	-0.5
4	10.3	10.5	1.6	-7.0	9.8	10.5	1.4	-12.1
	EVC = 101.5° aTDC							
1	11.6	11.0	2.1	-19.5	11.8	11.0	2.1	-11.9
2	11.1	11.0	2.2	-22.3	11.2	11.0	2.3	-19.4
3	11.2	11.0	2.2	-16.8	11.5	11.0	2.2	-17.3
4	11.1	11.0	2.0	-15.3	11.3	11.0	2.1	-20.2
	EVC = 100.5° aTDC							
1	12.2	11.8	2.6	-24.0	11.9	11.8	2.4	-16.4
2	11.7	11.8	3.2	-17.6	11.8	11.8	3.0	-15.8
3	11.8	11.8	2.6	-13.6	11.8	11.8	2.6	-1.2
4	11.6	11.8	2.4	-12.5	11.3	11.8	2.1	-4.3

Figure 6.4 shows the results of cylinders 1 and 2 in Table 6.1 through the use of return maps and probability densities. Specifically, the return map is divided up into bins (similar to pixels), each bin contains a certain amount of cycles depending on the return map and bin position. From this information we can find the probability distribution function in the x and y directions for each bin and assign a color value which is proportional to the probability that a sequence of cycles will occur in that particular bin. The result is a return map which shows us not only cycle-by-cycle couplings but the probability (color) for a transition from $\theta_{50}(k)$ to $\theta_{50}(k+1)$. One can observe that the controlled cycles have less dispersion in early and late events indicating that the control was effective. In addition, the controlled tests show that

the most dense points lie on the diagonal, this further demonstrates the control's effectiveness to reduce the CV as well as the dispersion. The results for cylinders 3 and 4 were similar and are provided in Fig. 6.5.

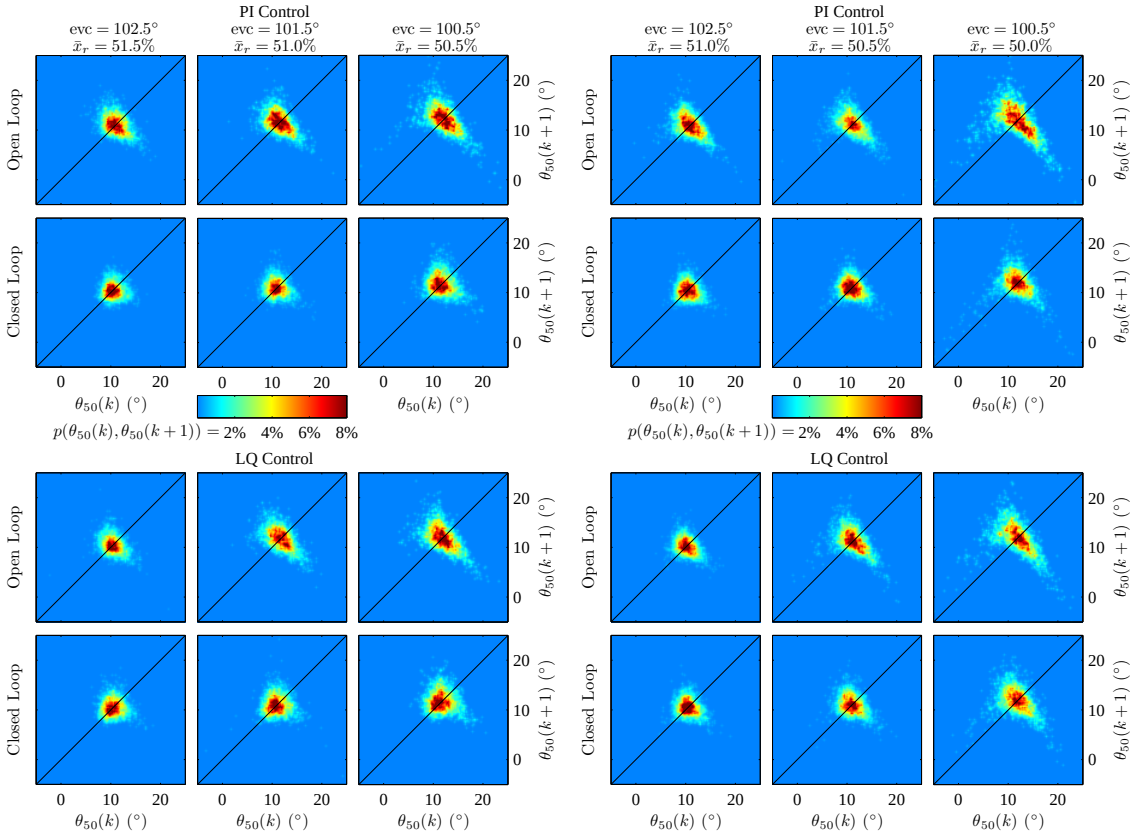

Figure 6.4: Comparison of return maps of combustion phasing for proportional and state feedback control for cylinder number 1 (left) and cylinder number 2 (right). From left to right the tests have a progressively smaller x_r resulting in an increasing level of CV. Cylinder 1 was the least variable while cylinder 2 was the most variable.

The model was parameterized for the middle case, corresponding to a residual gas fraction of 51% and as expected the controllers perform best when at this operating point. Proportional control is more robust to deviations from this point, this can be seen in the reduction in standard deviation in Table 6.1. One can also observe that the integrator has effectively controlled the mean combustion phasing to a set point and that the difference from open loop is small. The results of Table 6.1 show that both control methods were effective in reducing the CV in all cases. However, some were better than others. The small reductions at low CV are most likely due to the fact that there is little room for improvement, the process is not exhibiting a large increase in combustion phasing dispersion. In the high CV case there is more potential

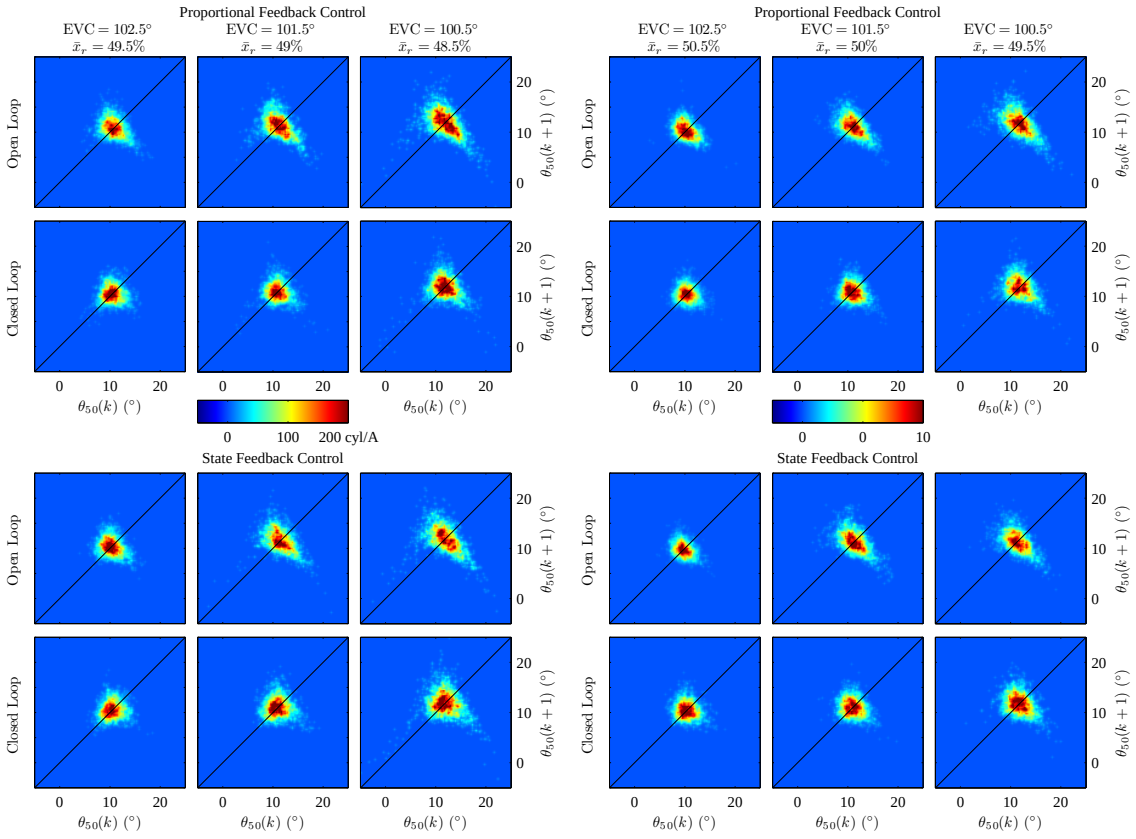

Figure 6.5: Comparison of return maps of combustion phasing for proportional and state feedback control for cylinder number 3 (left) and cylinder number 4 (right). From left to right the tests have a progressively smaller x_r resulting in an increasing level of CV.

for a decrease in dispersion, however as the CV increases the process becomes more complex. Since linear control is used it is reasonable that performance is limited in narrow regions around the linearization.

6.3.2 Evaluation of Control Effectiveness

Since mean combustion phasing from open loop has been maintained in closed loop the effectiveness of the control is easily observed through a percent reduction of standard deviation. Figure 6.6 shows this through the time series data of combustion phasing and the control signal, SOI, for all four cylinders, for the PI control case. Figure. 6.7 displays the same information for the LQ control. The results shown here are for the state feedback control on the medium level of CV. One can see that there is a visible reduction in the variability of the combustion when transitioning from open

loop (grey) to closed loop (black). In addition the SOI perturbations are small, less than $\pm 5°$, and the reduction is achieved while maintaining the perturbation around the open loop SOI value.

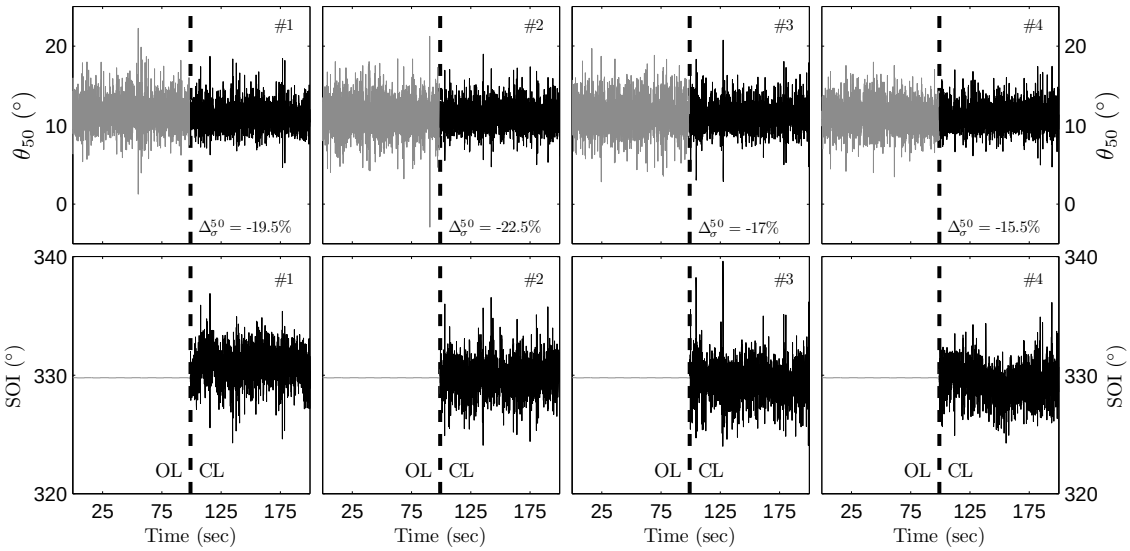

Figure 6.6: Time series data of PI control at medium CV. Open loop results in grey and closed loop in black show the reduction in combustion phasing variability (top) and the SOI control signal (bottom).

Return maps and symbolic statistics for this same data are displayed in Fig. 6.8. Symbolic statistics is a non-linear time series technique used to quantify the probability that specific sequences of cycles may occur, for a detailed explanation of this tool see [70, 93]. Here the sequence length is set to 3 and the time series data is divided into 5 equally probable bins. Since the bins are divided to be equally probable any combination of bins is equally probable if there are no couplings between cycles, as is the case for highly stable combustion. The result of this would be a flat relative frequency spectrum. However, as we transition into high variability we observe spikes in the frequency spectrum indicating that some sequences are more likely to occur than others and that the dynamics are deterministic, which are predicted by the model as shown in [84]. It is therefore desired to not only contract the return map close to the diagonal using control but to also flatten the spectrum in the symbolic statistics. In addition if the return maps and symbolic statistics were featureless then all that would be left in the system is noise, no deterministic coupling between cycles. In this instance further reduction in variability wouldn't be possible with deterministic control.

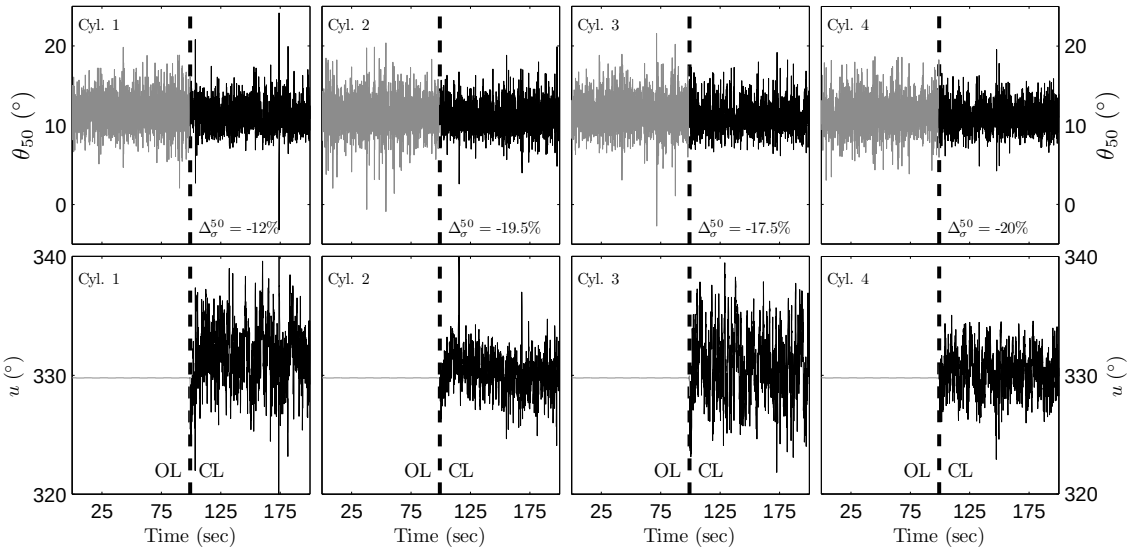

Figure 6.7: Time series data of LQ control at medium CV. Open loop results in gray and closed loop in black show the reduction in combustion phasing variability (top) and the SOI control signal (bottom).

Figure 6.8 clearly shows that control achieves both of these goals for all four cylinders despite the noted difference in residual gas fraction in each cylinder. Results for other cases were similar.

6.4 Summary

This chapter has developed two controllers which are effective at reducing the cyclic variability associated with late combustion phasing in lean HCCI. The controllers were tested for three different levels of CV and on all 4 cylinders, in all cases the variability was reduced. One key component of the control is the slow integrator, which helps to maintain the combustion phasing at a particulare operating condition. This is important to fairly evaluate the control against open loop data.

While this control is useful for reducing the CV at steady state, a more important condition would be regulating the CV which may occur during a transient. In Chapter 8 the knowledge obtained here for CV control at steady state is applied to a midranging controller with adaptive feedforward to help make large load transition in HCCI. Without the understanding of the cyclic variability dynamics and how to control it, these transition would not be possible. In the following chapter, the adaptive model used for the controlled load transitions in Chapter 8 is developed.

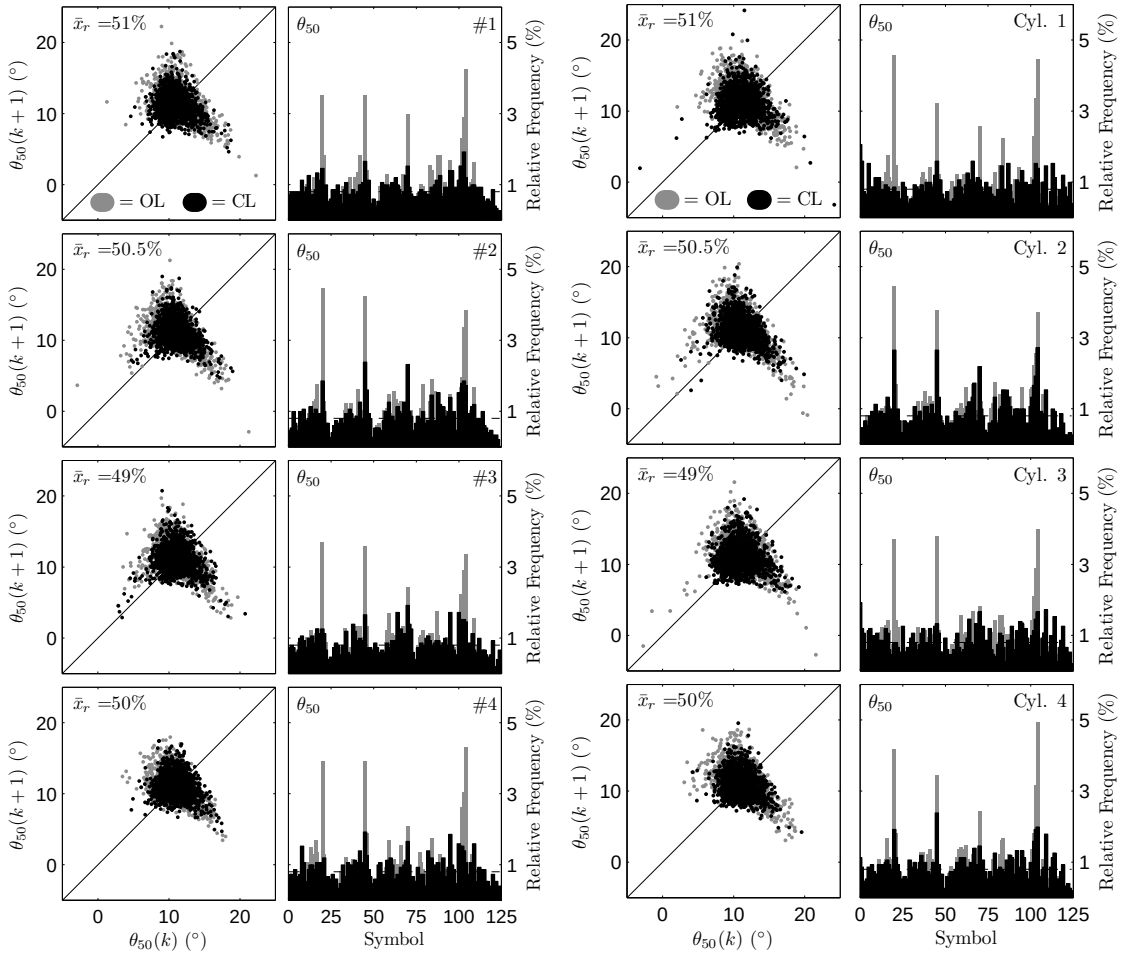

Figure 6.8: Return maps and symbolic statistics of PI control (left) and LQ control (right) at medium CV. Open loop results in grey and closed loop in black. The contraction of the return maps and flattening of the symbolic statistics indicate effective control.

Chapter 7

Adaptive HCCI Model

7.1 Introduction

In this chapter the model in App. A is augmented with the online residual mass estimation from Chapter 4 as an additional state. An adaptive parameter estimation scheme is developed and used to increase the model fidelity in terms of its ability to reject disturbances and modeling error. Adaptive parameter estimation has been used in literature to improve the fidelity of SI engine models in [94] and for control purposes in [95, 96, 97, 98, 99, 100, 101]. Additionally, adaptive control was applied to an HCCI engine model in [102]. The current HCCI model requires parameterization which is non-trivial and time intensive. It will be shown through experiments that a parameterization for a single cylinder is sufficient when the adaptive parameter estimation is used, this reduces model calibration effort. Other advantages of using adaptation include reducing sensitivity to engine aging, cylinder-to-cylinder variation and unmodeled dynamics as well as rejecting actuator bias.

7.2 Model of Combustion Phasing and Exhaust Gas Temperature

The model from [38, 39] is used here for the prediction of combustion phasing and for a model of the exhaust gas temperature. The model is summarized in App. A and consists of two dynamic states used to capture cycle to cycle interactions which are:

1. T_{bd}: The temperature of the blowdown gases, which is used to represent the recycled thermal energy.
2. b_{bd}: The burned gas fraction of the blowdown process, which represents the composition dynamics.

The blowdown process is a rapid expansion of exhaust gases during the exhaust stroke where the pressures of the cylinder and exhaust system equalize quickly.

The states are defined immediately after the blowdown process and are given by Eqs. (7.1) and (7.2) which represent the temperature and composition dynamics respectively.

$$\begin{aligned} T_{bd}(k) =& T_{ivc}(k-1)\left(\frac{p_{ivc}(k-1)}{p_{em}}\right)^{\frac{1-n}{n}} \\ & \left[1+\frac{\eta_m(k-1)q_{lhv}R{V_{50}}^{n-1}}{c_v p_{ivc}{V_{ivc}}^{n}}m_f(k-1)\right]^{\frac{1}{n}} \end{aligned} \tag{7.1}$$

$$b_{bd}(k) = \frac{(AFR_s+1)\,m_f(k-1)}{m_c(k-1)} + \Theta\hat{x}_r(k-1)b_{bd}(k-1). \tag{7.2}$$

The full set model equations is given in the appendix. The value of T_y, V_y and p_y are the temperature, volume and pressure at the indicated valve. Specifically the temperature at the time of IVC is given by:

$$\begin{aligned} T_{ivc}(k-1) =& \Theta\hat{x}_r(k-1)T_{res}(k-1)+ \\ & (1-\Theta\hat{x}_r(k-1))\,T_{im}, \end{aligned} \tag{7.3}$$

where T_{res} is defined as in Eq. (A.15), T_{im} is the intake manifold temperature and Θ is the adaptive parameter presented in the following sections. When no adaptation is in place, $\Theta = 1$. The residual gas fraction estimate, $\hat{x}_r$, is:

$$\begin{aligned} \hat{x}_r(k-1) = & 1-(c_0+c_1\theta_{evc}(k-1)) \\ & \left(\frac{p_{im}(k-1)}{p_{em}(k-1)}\right)^{c_2} T_{bd}(k-1)^{c_3}\omega(k-1)^{c_4} \end{aligned} \tag{7.4}$$

where $c_{0,1,2,3,4}$ are coefficients tuned to steady state data, θ_{evc} is the angle of exhaust valve closing and ω is the engine speed. The values of p_{im} and p_{em} are the intake and exhaust manifold pressures respectively. The combustion efficiency, η_m, is defined by Eq. (A.7) and is a function of estimated $\hat{\theta}_{50}$. The model is dependent on several constants: The lower heating value of the fuel q_{lhv}, the gas constant R, polytropic coefficient n, specific heat c_v and the stoichiometric air-fuel ratio AFR_s. The total charge mass is defined by $m_c = m_{air} + m_f + m_{res}$.

The model has three inputs: the mass of fuel injected (m_f), the injection timing (SOI), and the timing of the exhaust valve closing (EVC). The EVC timing controls the amount of NVO, the crank angle difference between EVC and intake valve open-

ing (IVO), with which the engine operates. This has a direct impact on the charge composition and temperature. The model has two outputs, the combustion phasing of 50% burn ($\hat{\theta}_{50}$) and the engine torque (IMEP).

Exhaust gas temperature can be measured with relative ease in steady state, however in transients the measurement suffers from significant time delays. Due to the residual estimation's sensitivity to the exhaust gas temperature as shown in Chapter 4 it can be beneficial to replace this measurement with a model capable of capturing transients. Because the temperature is defined right after blowdown it can be used as a replacement to the measured exhaust gas temperature in Eq. (4.5). A further coupling of the two state model and the residual mass estimation is achieved by using the transient residual estimation of Eq. (4.5) as a replacement to the static regression of residual gas fraction in Eq. (A.12). The residual estimation then becomes an additional state, creating a three state model. The full model is summarized by:

$$T_{bd}(k+1) = f_1(T_{bd}(k), \Theta(k)\hat{x}_r(k), u(k)) \tag{7.5}$$

$$b_{bd}(k+1) = f_2(T_{bd}(k), b_{bd}(k), \Theta(k)\hat{x}_r(k), u(k)) \tag{7.6}$$

$$m_{res}(k+1) = f_3(T_{bd}(k), m_{res}(k), u(k)) \tag{7.7}$$

$$\text{where } \hat{x}_r(k) = \frac{m_{res}(k)}{m_c(k)} = \frac{m_{res}(k)}{m_{res}(k) + m_{air}(k) + m_f(k)} \tag{7.8}$$

7.3 Adaptive Parameter Estimation

The use of the two state model for the prediction of exhaust gas temperature allows the online residual estimation to better perform in transients. However, the model is still control-oriented and as such it is susceptible to modeling errors and parameter drift. Additionally it requires a transient air mass as an input. The model is also non-linear and requires parameterization which is non-trivial and time consuming, it is therefore desirable to minimize this effort. One method to reduce parameterization effort and minimize modeling errors is to include adaptive parameters which can adjust the model online to make compensations appropriately. The selection of an adaptive parameter or parameters is challenging due to the models non-linearities, ideally one would want to achieve a large authority over the model's output with a small number of adaptive parameters.

7.3.1 Defining the Parametric Model

Since the combustion phasing in HCCI is most significantly influenced by T_{ivc}, and the value of T_{ivc} as shown in Eq. (A.17) has a high sensitivity to the residual gas fraction, it was concluded that the adaptive parameter would scale the model's estimate of the residual gas fraction, $\Theta\hat{x}_r$, where Θ is the unknown adaptive parameter. To determine the parameter Θ an error term is required,

$$\epsilon(k-1) = \bar{x}_r(k-1) - \Theta(k-1)\hat{x}_r(k-1) \tag{7.9}$$

where $\bar{x}_r$ would ideally be the measured value of the residual gas fraction, x_r. It is however extremely difficult to measure the residual gas fraction of an engine, especially online. We therefore employ the measurement of the combustion phasing, $\bar{\theta}_{50}$, provided by the ECU through the use of the in-cylinder pressure sensors and online heat release analysis.

The combustion phasing model, see Eq. (A.1) in the appendix, can be well approximated by the quadratic expression:

$$\bar{\theta}_{50}(k-1) = \alpha_{\theta 1}T_{ivc}^2(k-1) + \alpha_{\theta 2}T_{ivc}(k-1) + \alpha_{\theta 3} \tag{7.10}$$

where $\alpha_{\theta 1,2,3}$ are functions of the injection timing. Through inversion of this model the value of T_{ivc} which was necessary for the measured combustion phasing ($\bar{T}_{ivc}$) of the previous cycle is given by:

$$\bar{T}_{ivc}(k-1) = \frac{-\alpha_{\theta 2} - \sqrt{\alpha_{\theta 2}^2 - 4\alpha_{\theta 1}(\alpha_{\theta 3} - \bar{\theta}_{50}(k-1))}}{2\alpha_{\theta 1}}. \tag{7.11}$$

The other solution to the quadratic is always a non-physical solution. If we then employ a mass balance at IVC as shown in:

$$\bar{T}_{ivc}(k-1) = \bar{x}_r(k-1)T_{res}(k-1) + (1 - \bar{x}_r(k-1))T_{im}, \tag{7.12}$$

where T_{im} is the measured intake manifold temperature and T_{res} is given by Eq. (A.15) of the model, then the value of $\bar{x}_r$ is simply:

$$\bar{x}_r(k-1) = \frac{\bar{T}_{ivc}(k-1) - T_{im}}{T_{res}(k-1) - T_{im}}. \tag{7.13}$$

Equation (7.13) along with Eq. (7.8) can then be used in Eq. (7.9) to find the parameter error.

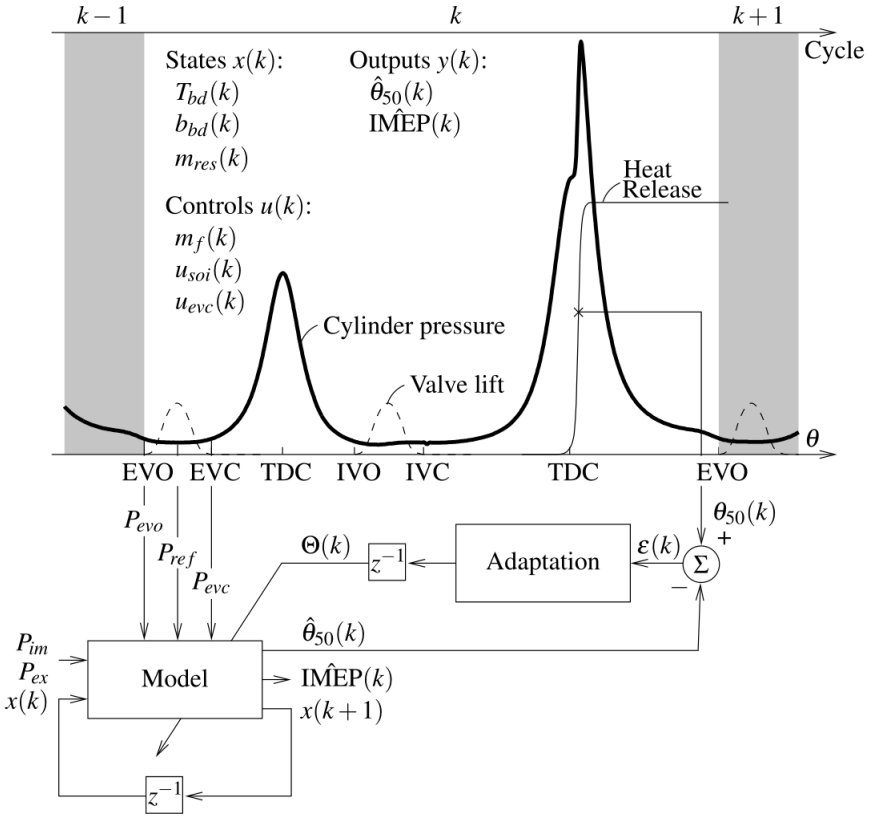

Figure 7.1: Graphical representation of model structure. The figure indicates when the time series data is broken into discrete elements, the model inputs and outputs as well as the states. Also shown is the basic block diagram of the model indicated what measurements are used.

Adaptive law

The discrete gradient parameter estimation law given in Eq. (7.14) is used to determine the value of Θ on each cycle. The equation and its stability properties are derived in [103, 104]. The speed at which the algorithm converges is controlled by the constant gain κ, the gain should be to make convergence slow and prevent the adaptive controller from changing the transient response of the system.

$$\Theta(k) = \frac{\kappa x_r(i)\epsilon(i)}{x_r(i)^2 + c_\Theta} + \Theta(k-1), \text{ where } \kappa, c_\Theta = \text{constants} \tag{7.14}$$

There are two conditions with this formulation which can cause convergence issues: $x_r^2 + c_\Theta = 0$ and either $x_r\epsilon, x_r^2 + c_\Theta \to \infty$. Since $x_r \in [0,1]$ then x_r^2 will stay positive provided it starts positive, the addition of c_Θ ensures this as it is a small but positive constant, x_r^2 additionally it cannot grow unboundedly. The value of $x_r\epsilon$ will stay bounded provided the error is bounded. To avoid unwanted behavior however,

the value of Θ is also restricted to be within $\Theta \in [0.9,\ 1.2]$, this is a physically justified restriction as it is unlikely the actual in cylinder residual gas fraction will change by more than 10-20%.

A diagram of the adaptive model structure can be found in Fig. 7.1. The figure indicates the model inputs and outputs as well as the states and crankangle at which the states are defined.

7.3.2 Authority of Adaptive Parameter

In order to observe the effect that the adaptive parameter has on the model, simulations where run for the range of possible Θ values. At each point the model was allowed to come to steady state and the values of T_{bd}, b_{bd} and the predicted combustion phasing were observed, see Fig. 7.2. The sweep was performed at both 1800 and 1600RPM. This simulation was done with 10.8mg of fuel, an SOI of 330° and an EVC of -106°. The effect on the model's states and output was approximately affine with high authority over the output, θ_{50}. Additionally, at each operating point a linearization of the model was done and the eigenvalues were found to lie on the real positive axis within the unit circle indicated the model remains stable for this range of residual gas fractions.

7.3.3 Stability

To understand the stability of the adaptive parameter estimation scheme the simplified system in Fig. 7.3 can be analyzed. The two state model was used in this analysis with a static regression of the model prediction of residual gas fraction given by Eq. (A.12). This is done to simplify the analysis. The estimated residual gas fraction from an actual measurement of combustion phasing, $\bar{x}_r$, is treated as an input to the system. With these assumption a linearized state update equation for Θ can then be derived by combining equations Eqs. (7.14) and (7.9) to get:

$$\begin{aligned}\Theta(k) =& \frac{\kappa \bar{x}_r^2(k-1)}{\bar{x}_r^2(k-1) + c_\Theta} + \\ & \Theta(k-1)\left(1 - \frac{\kappa \bar{x}_r(k-1)\hat{x}_r(k-1)}{\bar{x}_r^2(k-1) + c_\Theta}\right).\end{aligned} \tag{7.15}$$

To show that the system is stable we must demonstrate that at steady state Θ converges to a value which causes the error, ϵ, in Eq. (7.9) to go to zero. If we solve

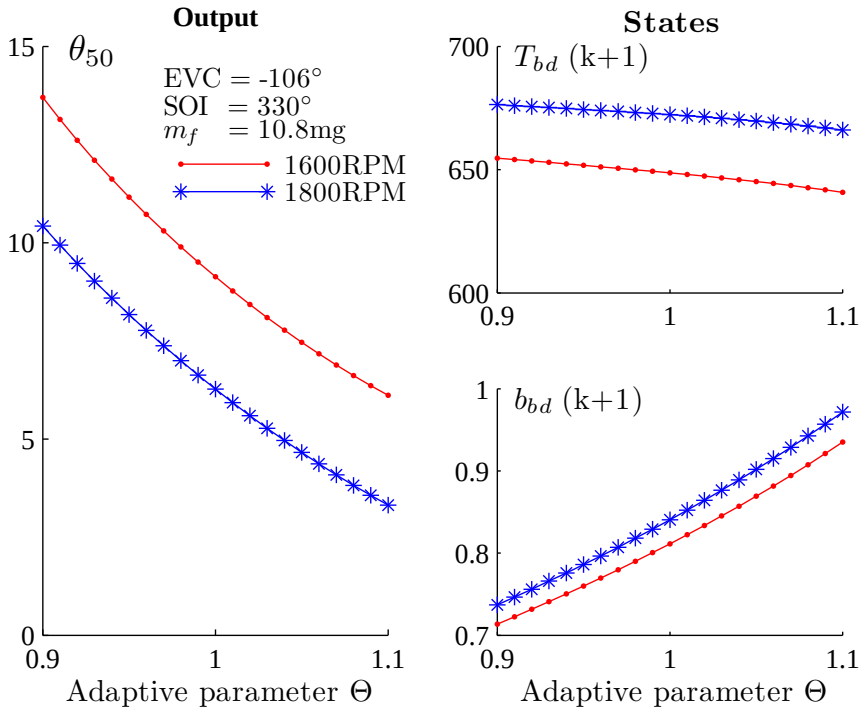

Figure 7.2: A sweep of the adaptive parameter Θ shows its effect on the model states T_{bd} and b_{bd} (right), and the model output θ_{50} (left). The effect on θ_{50} is approximately affine.

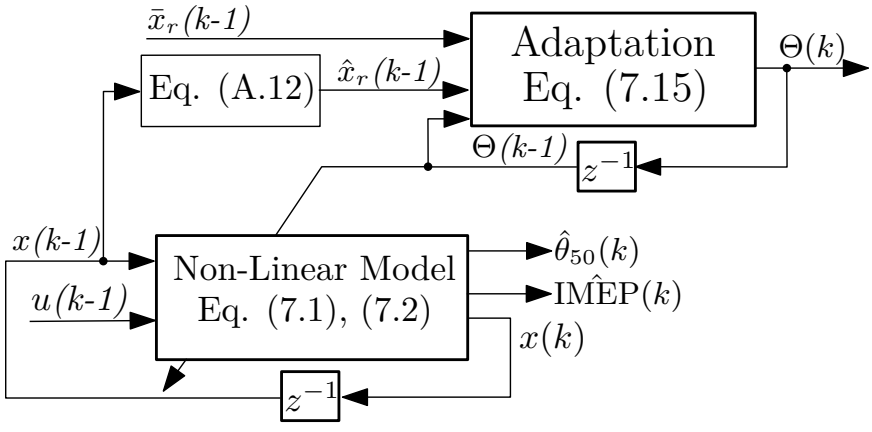

Figure 7.3: System used for analysing the stability of the estimation scheme. The value of $\bar{x}_r$ is treated as an input to the system.

Eq. (7.9) for Θ when $\epsilon = 0$ we can see that $\Theta^* = \bar{x}_r^*/\hat{x}_r^*$ where * indicates the steady state value of the parameter.

Equation (7.15) can be linearized about Θ^* as well as the steady state values of the states T_{bd} and b_{bd} in Eqs. (7.1) and (7.2).

$$\begin{aligned}\Delta\Theta(k) = &\left(1 - \frac{\kappa \bar{x}_r^* \hat{x}_r^*}{\bar{x}_r^{*2} + c_\Theta}\right) \Delta\Theta(k-1) + \\ &\left(\frac{\kappa \alpha c_3 \bar{x}_r^{*2} T_{bd}^{*(c_3-1)}}{\hat{x}_r^*(\bar{x}_r^{*2} + c_\Theta)}\right) \Delta T_{bd}(k-1) + \\ &\left(\frac{\kappa \bar{x}_r^*}{\bar{x}_r^{*2} + c_\Theta}\right) \Delta \bar{x}_r(k-1) \\ \text{Where } \alpha = &\,\Pi^{c_2}(c_0 + c_1\theta_{evc})\omega^{c_4}\end{aligned} \tag{7.16}$$

This equation can be augmented with a linearization of the system in Eqs. (7.1) and (7.2) where Θ is added as a multiplicative modification to the residual gas fraction, as in Eq. (A.17), to yield:

$$\begin{aligned}\begin{bmatrix} T_{bd}(k) \\ b_{bd}(k) \\ \Theta(k) \end{bmatrix} = &\begin{bmatrix} 0.4871 & -93.2017 & 84.1512 \\ -0.0001 & 0.5176 & 0.5494 \\ \left(\frac{\kappa \alpha c_3 \bar{x}_r^{*2} T_{bd}^{*(c_3-1)}}{\hat{x}_r^*(\bar{x}_r^{*2} + c_\Theta)}\right) & 0 & \left(1 - \frac{\kappa \bar{x}_r^* \hat{x}_r^*}{\bar{x}_r^{*2} + c_\Theta}\right) \end{bmatrix} \cdot \\ &\begin{bmatrix} T_{bd}(k-1) \\ b_{bd}(k-1) \\ \Theta(k-1) \end{bmatrix} + \begin{bmatrix} B_{11} & 0 \\ B_{21} & 0 \\ 0 & \left(\frac{\kappa \bar{x}_r^*}{\bar{x}_r^{*2} + c_\Theta}\right) \end{bmatrix} \begin{bmatrix} u_{ss}(k-1) \\ \bar{x}_r(k-1) \end{bmatrix}. \\ \text{Where } B_{11} = &[-1.6, 33.2, -0.02, 0.08], \\ B_{21} = &[-0.004, 0.04, 0, 0] \text{ and } u_{ss} = [u_{evc}, m_f, u_{soi}, \omega]\end{aligned} \tag{7.17}$$

This augmented system allows us to observe the effect the adaptive parameter has on the dynamics of the temperature and composition states as well as the eigenvalue of the adaptive parameter state itself. This is shown through the root locus plot of Fig. 7.4. Here we can see that when the adaptive gain κ is 0 the eigenvalues of the temperature and composition dynamics are the same as the system with no adaptation, both are on the positive real axis. Additionally the eigenvalue of Θ is one. As κ is increased the eigenvalues of the system approach each other and eventually break off into the imaginary plane. At approximately $\kappa = 1$ the system becomes unstable. The eigenvalue associated with the adaptive parameter is pulled inward while κ in-

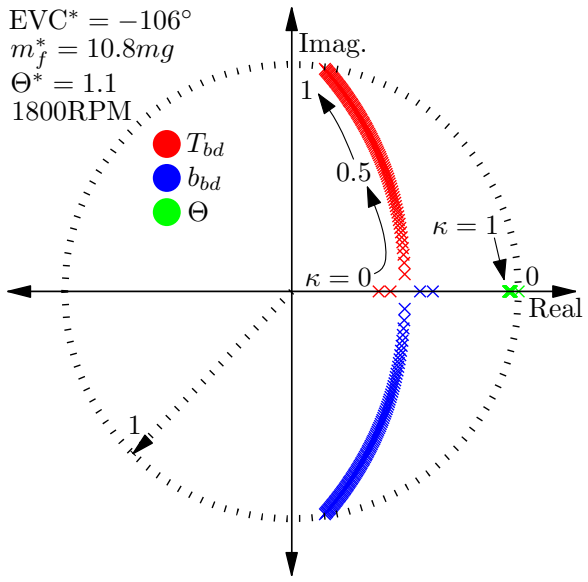

Figure 7.4: Root Locus of the eigenvalues associated with the system in Eq. (7.17). As κ is increased the adaptation occures more quickly but the underlying system eventually becomes unstable.

creasing indicating that the parameter will converge faster with a higher gain as is expected. For small gains the system is stable, which indicates that ϵ will converge to 0.

To demonstrate how the adaptive parameter converges, the system in Fig. 7.3, as summarized by Eq. (7.17), was simulated with a value of $\bar{x}_r$ which corresponded to $\Theta^* = 0.9$ and $\bar{\theta}_{50} = 8.2$. Three different adaptive gains were tested. The results are shown in Fig. 7.5 and it can be seen that the system successfully converges to the unknown parameter Θ^* and the desired combustion phasing $\bar{\theta}_{50}$. A gain of $\kappa = 0.005$ was used for the tests presented in the following sections because it offers good convergence time without pulling the temperature and composition eigenvalues off of the real axis.

7.4 Experimental Transient Results

The adaptive model was implemented on the rapid prototyping hardware as described in Chapter 2 to evaluate is capabilities. For these tests the engine was run in open loop except for closed loop control of the engines coolant, oil temperature and speed.

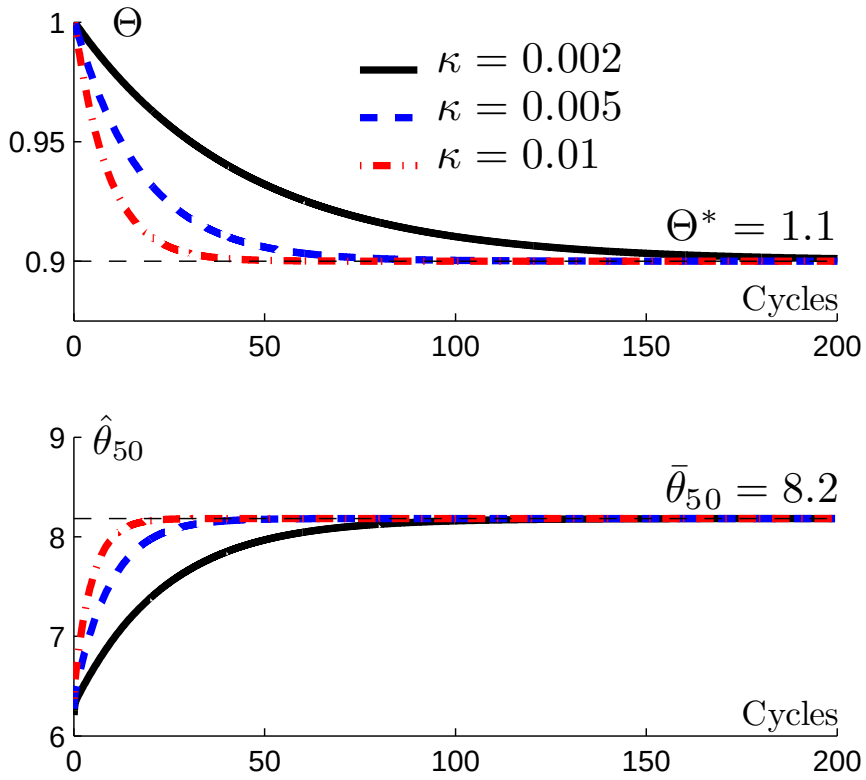

Figure 7.5: Convergence of the adaptive parameter to a set point with different gains, the prediction of combustion phasing, $\hat{\theta}_{50}$ also converges to the measured combustion phasing $\bar{\theta}_{50}$

7.4.1 Multicylinder Results

To test the adaptive model's capability to correct for modeling and parameterization errors it was run in real time at steady state conditions with and without adaptation. The response in predicted combustion phasing was observed. The results can be found in Fig. 7.6. The model was parameterized for only cylinder 1 and then propagated to the other cylinders. Day-to-day drift and uncontrollable changes in environmental conditions cause there to be a difference in the predicted versus calculated values for the various cylinders. Cylinder number 2 had large errors while cylinders 3 and 4 appeared to fit the parameterization relatively well. Regardless, when adaptation is turned on at approximately cycle number 200, the adaptive parameter makes adjustments to the model and the prediction of combustion phasing becomes more accurate. As expected, the adaptive parameter deviates from unity further when the error is larger, as is the case for cylinders 1 and 2. The root mean square (RMS) error, averaged over all four cylinders, between the predicted and actual values of combustion phasing with no adaptation was 2.51 cad while the RMS error with adaptation was 1.73 cad. Similar reductions in error were observed on all experimental results presented.

It should be noted that when the prediction of residual gas fraction, $\hat{x}_r$, causes the model to predict a combustion phasing that is earlier than that of the ECU, then $\Theta < 1$ due to the monotonic relationship between x_r and θ_{50}. For the results presented here, the value of Θ was always less than one. This is due to the model always predicting a combustion phasing which is earlier than that of the actual value, an over prediction of the residual gas fraction. For a different parameterization of the model or a different operating condition the prediction could have been later than the actual phasing, this would cause the adaptive parameter to be greater than 1. This was explored in simulations but did not present itself in these experiments. The controlled experiments in the following chapter exhibit this behavior.

7.4.2 Single Actuator Steps

To evaluate the effectiveness of the adaptive model and residual gas fraction estimation in transients, actuator steps of the model inputs were performed in open loop. Sensor measurements were obtained in real time from the engine's ECU and used by the model for real time prediction of θ_{50}. The actuator steps were repeated for both the adaptive and non–adaptive model.

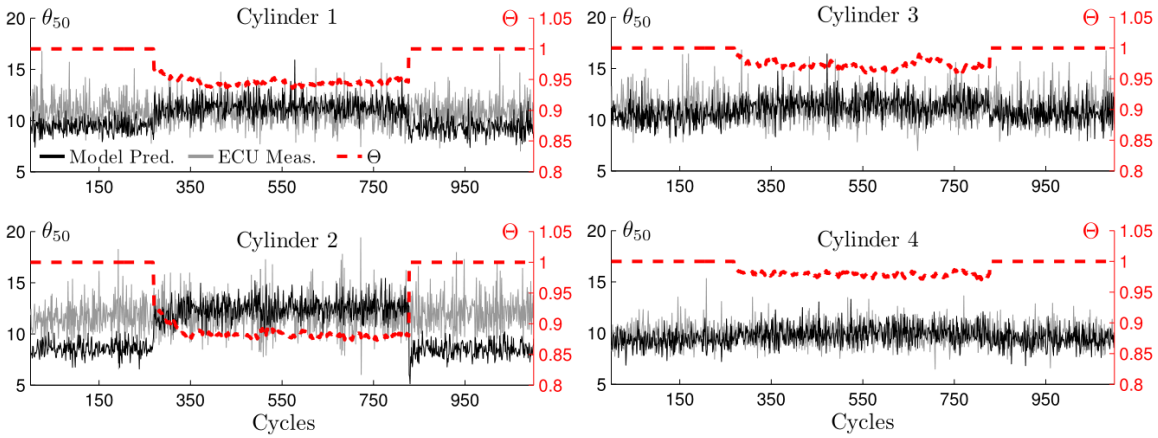

Figure 7.6: Combustion phasing prediction versus ECU calculation for the adaptive and non-adaptive versions of the model. It can be seen that with adaptation the error in combustion phasing is reduced.

A step in EVC is shown in Fig. 7.7 for cylinder 1. The step is from 256 to 253°$aTDC$ (degrees after top dead center) and back again and causes the amount of NVO to increase as a result. Intuitively, the amount of residual mass trapped in the cylinder should also increase, this is reflected in the prediction of the residual gas fraction as shown in Fig. 7.7. Also shown is the result of an offline analysis of the residual gas fraction derived from an iterative method described in [64, 23] and in Chap. 3, Sec. 3.3. While the absolute difference between the two results is slightly different, the magnitude and direction of the transient response is similar. As described in previous sections, it is expected that the absolute values may not be equal due to the difference in the value of the exhaust gas temperature and that of the state T_{bd}. As a consequence, the model prediction of θ_{50} differs from that of the ECU. However, when the adaptive parameter is introduced at approximately 1400 cycles, and the step is repeated, it is clear that the residual gas fraction drops to that of the offline analysis and the model prediction of θ_{50} becomes much more accurate on an absolute scale. It is not expected that the value of x_r always be equivalent to that of the offline processing except in the case of minimal modeling errors and environmental disturbances.

The model's response to steps in SOI and mass of fuel can be found in Fig. 7.8. The prediction of θ_{50} is improved in both responses. It should be noted that while the value of Θ stayed relatively constant during the EVC step, it has a visible response to the steps in SOI and fuel at steady state.

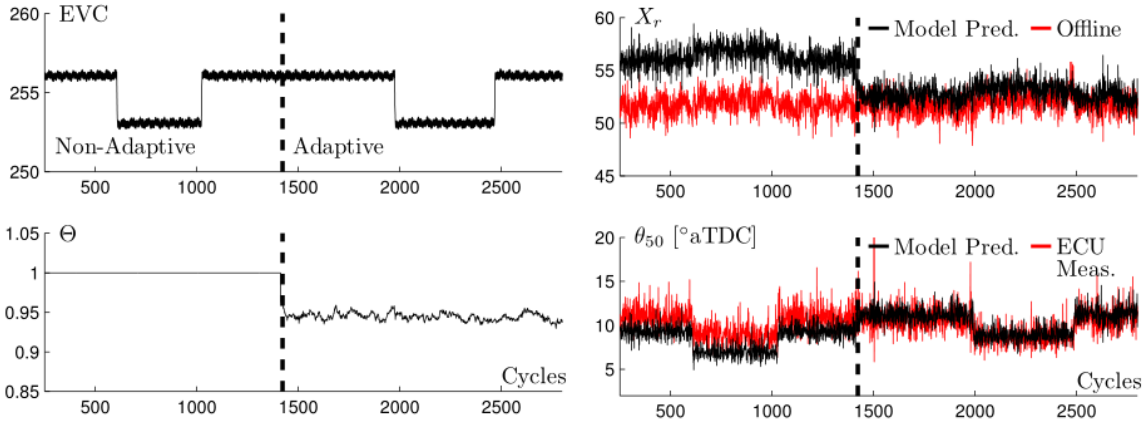

Figure 7.7: An EVC step for cylinder 1 with and without an adaptive model. It can be observed that the model prediction is more accurate when adaptation is applied.

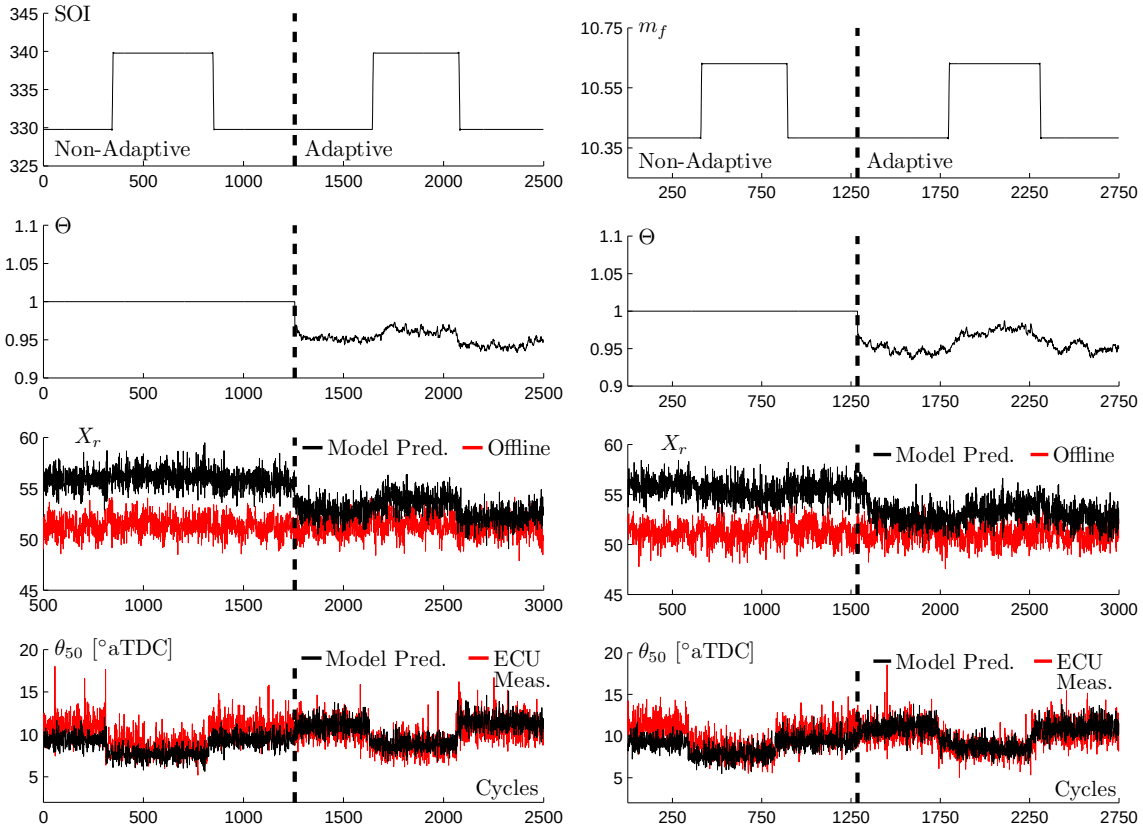

Figure 7.8: Model response to an SOI step (left) and a fuel mass step (right) with and without adaptation. When adaptation is applied the prediction of θ_{50} is more accurate.

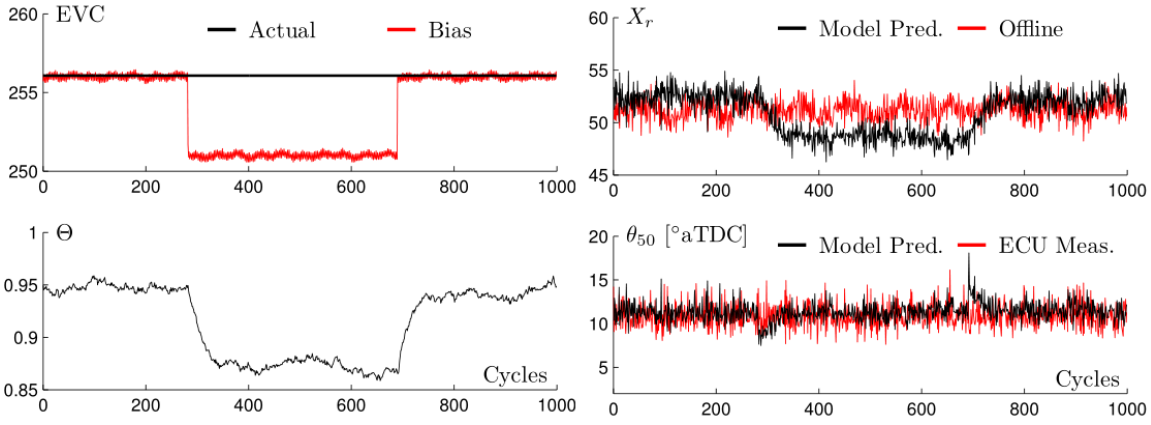

Figure 7.9: Adaptive model response to an injection of bias in EVC. The model quickly catches the bias and make corrections to minimize error in combustion phasing prediction.

7.4.3 Actuator Bias

It is common for engine components to wear and sensors to become more noisy with time, this can present a problem for online models which may not have knowledge about these changes. It is therefore desired that the adaptive model be able to reject such disturbances. To test this the model was run online with the engine operating at steady state, all actuators fixed. The measurement of EVC used by the model was then replaced with one with a bias for a short period of time as seen in Fig. 7.9. This bias represents camshaft wear over time. One can see that when the bias is applied at 250 cycles that the combustion phasing prediction starts to deviate quickly from the calculated value. However, the adaptive parameter makes adjustments to the residual gas fraction in order to minimize the error. A similar response can be seen at 750 cycles when the bias is removed. In a more realistic scenario this bias will be slowly occurring over a long period of time as the cam is mechanically worn due to friction. Another example of this could be a parameter could drift over time, for instance engine temperature changing based on weather conditions. This experiment considers the worst case situation of the bias being applied instantaneously.

7.5 Summary

This chapter presents a modification of the model from [38, 39] to include the additional state of trapped residual mass from Chapter 4. This compliments the two state model by adding a more physical representation of the residual gas fraction. Addi-

tionally, this also helps the residual mass estimation by replacing the measurement of the exhaust gas temperature with a model.

To further improve the model's accuracy, an adaptive parameter estimation routine is developed which can adjust the estimate of residual gas fraction online. This helps to mitigate modeling errors and alleviate some effort in parameterizing for multiple cylinders. Experimental results are provided which support this. The adaptive parameter estimation scheme is evaluated for its authority to manipulate the model's output as well as for stability and convergence. This same parameter estimation scheme is used in the following chapter to adjust the feedforward component of a mid-ranging controller used for large load transients.

Chapter 8

Adaptive Control of HCCI Load Transitions

8.1 Introduction

The adaptive parameter estimation scheme presented in Chapter 7 is used in this chapter to develop an adaptive controller for regulating combustion phasing. The stability properties of the adaptive state from Chapter 7 are still valid here however in this case the adaptive parameter is used to modify the feedforward control component in real-time. The midranging control structure adapted from [38, 39, 47] is used in conjunction with the adaptive feedforward to control load transitions. Midranging control is a method used primarily in process control applications [43, 44], however it has been utilized successfully in engines for combustion control where similar coarse and fine trim actuators are often available, [45, 46]. The midranging controller uses model-based feedforward to help speed up load transitions and better regulate combustion phasing. An overview of the adaptive control structure is given in Fig. 8.1.

8.2 Controller

The midranging controller with linear feedforward developed in [58] is used here as a baseline controller for regulation of combustion phasing (θ_{50}). Regulation of combustion phasing in an HCCI engine is critical due to its sensitivity to cyclic variability at late combustion phasing and the excessive pressure rise rates for early θ_{50}. As such, the controller objective is to regulate θ_{50} to a desired reference set-point during load transitions. This set-point is typically determined offline or provided by a supervisory controller.

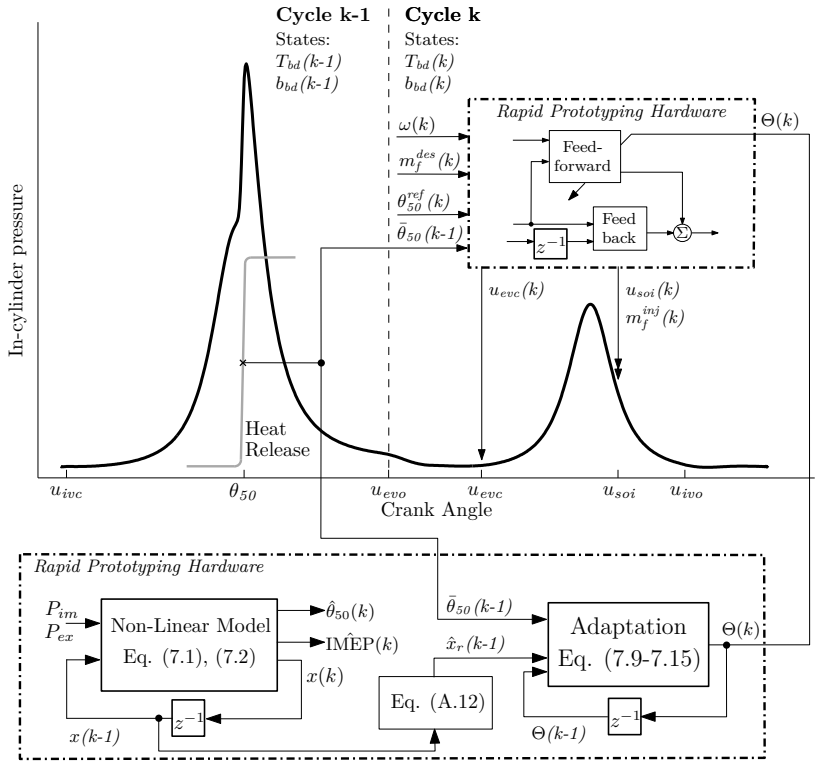

Figure 8.1: Graphical representation of the adaptive control structure. The figure indicates the cycle definition, the model inputs and outputs as well as the states. Also shown is the basic block diagram of the adaptive parameter estimation and how the adaptive parameter changes the feedforward control.

The baseline controller uses the u_{evc} and u_{soi} actuators to regulate θ_{50} in a mid-ranging configuration where the coarse and fine actuators are u_{evc} and u_{soi} respectively. This architecture is demonstrated graphically in Fig. 8.2 which has been adapted from [58]. The u_{evc} actuator has a large range and high authority however the hydraulic cam phasers are slow and there is a single intake and exhaust camshaft for all four cylinders, a single value of EVC must be applied for all cylinders. The u_{soi} actuator can be changed on a cycle-by-cycle and cylinder-by-cylinder basis however its authority is small and it can saturate quickly depending on the operating condition. Therefore the actuator u_{evc} strives to mid-range u_{soi} back to a set-point which is chosen to be in its region of greatest authority. The θ_{50} tracking error signal drives the controller for u_{soi}. Using the adaptive scheme we can mitigate errors and adjust the SOI control based on the adaptation of Θ and the θ_{50} tracking error.

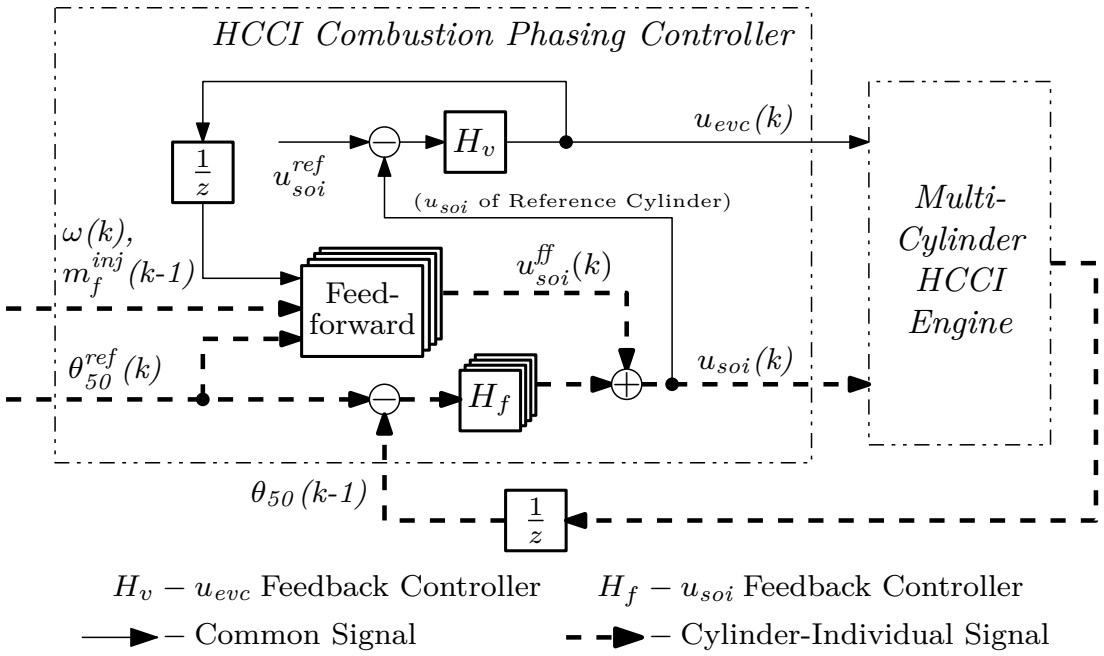

Figure 8.2: Midranging control architecture for a multicylinder engine. Here the coarse and fine trim actuators are u_{evc} and u_{soi} respectively.

8.2.1 Feedback Controller

During large load transitions the system can sometimes enter a region of high cyclic variability. This variability often causes incomplete combustion and unburned fuel [19]. The proportional control gain needed to regulate oscillatory combustion is different than that of non-oscillatory combustion [14, 70, 85, 90]. Specifically the gain is of opposite signs for the two cases. This is because an eigenvalue crosses over from the right half plane to the left half plane when a CV region is encountered. The onset of oscillatory combustion is observed after sufficiently late combustion, when the combustion phasing passes a threshold the efficiency is low enough that unburned fuel is left to burn during the recompression region. This behavior can be characterized by observing the combustion efficiency as a function of combustion phasing and peak cylinder temperature as shown in Fig. 8.3. It was observed that for combustion phasings later than $\theta_{50}^{thresh} \approx 10^{\circ}$ after top dead center the efficiency drops off sharply and the peak cylinder temperatures fall. If the peak cylinder temperatures fall too far, the cutoff for CO to CO_2 conversion can be reached. Therefore, a combustion phasing which exhibits stable combustion at one load, could be unstable at a lower load. The peak temperature are insufficient for complete combustion.

To compensate for this behavior a gain scheduled feedback is implemented. If the controller observed a combustion cycle which had a phasing later than the threshold

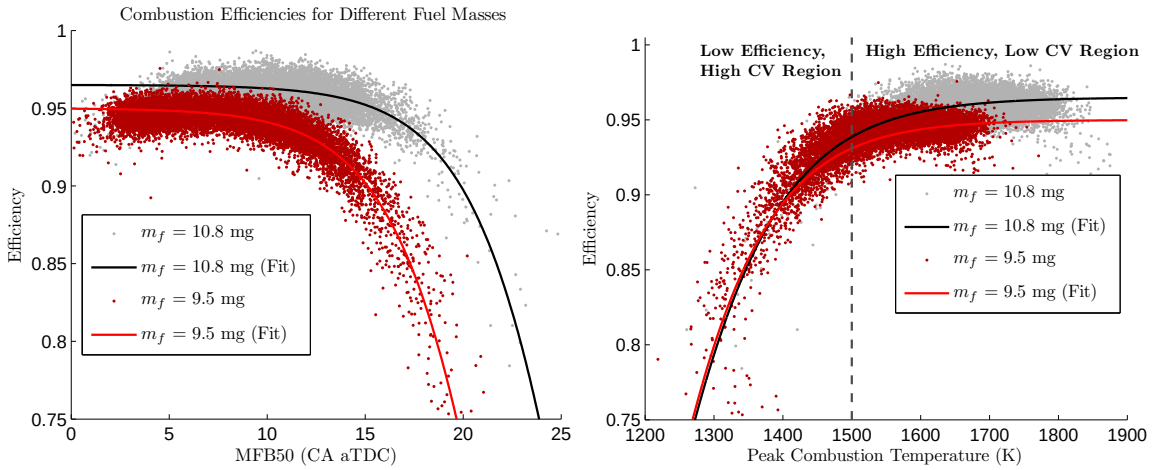

Figure 8.3: Effect of combustion phasing (left) and peak cylinder temperature (right) on combustion phasing. For certain regions a noticeable drop in efficiency is observed indicating thresholds for the onset of high cyclic variability.

for possible CV then the high CV gain was applied for the subsequent cycle. In summary, $K_p^{soi} = K_{p,lowcv}^{soi}$ if $\theta_{50} \leq \theta_{50}^{thresh}(m_f)$ and $K_p^{soi} = K_{p,highcv}^{soi}$ if $\theta_{50} > \theta_{50}^{thresh}(m_f)$ where $K_{p,lowcv}$ and $K_{p,lowcv}$ are of opposite signs. This gain scheduling based on knowledge of the onset of CV greatly improves the controllers ability to handle large transients as indicated in Fig. 8.4.

In this test the midranging controller is used without the adaptive feedforward and a load step down is performed with and without the gain scheduled feedback control. Before the transition the combustion phasing is stable. However when the load step down is commanded the non-switching case misfires. It recovers from this misfire, but large oscillations are observed in the combustion phasing and there are significant torque fluctuations. When the switching control is enabled we can see that at the time the load step occurs the gain flips sign momentarily. It continues to do this several times during the test. Specifically when the controller detects a late combustion phasing and the possibility of the onset of CV. The result is that the load step is achieved quickly and without misfire. Additionally the fluctuations in combustion phasing have been reduced significantly.

8.2.2 Feedforward Controller

The feedforward component of u_{soi} from [58] is modified here to incorporate the adaptive parameter, which is taken as an input. The feedforward control is found by linearizing the non-linear model summarized by Eqs. (7.1) and (7.2) about a typical

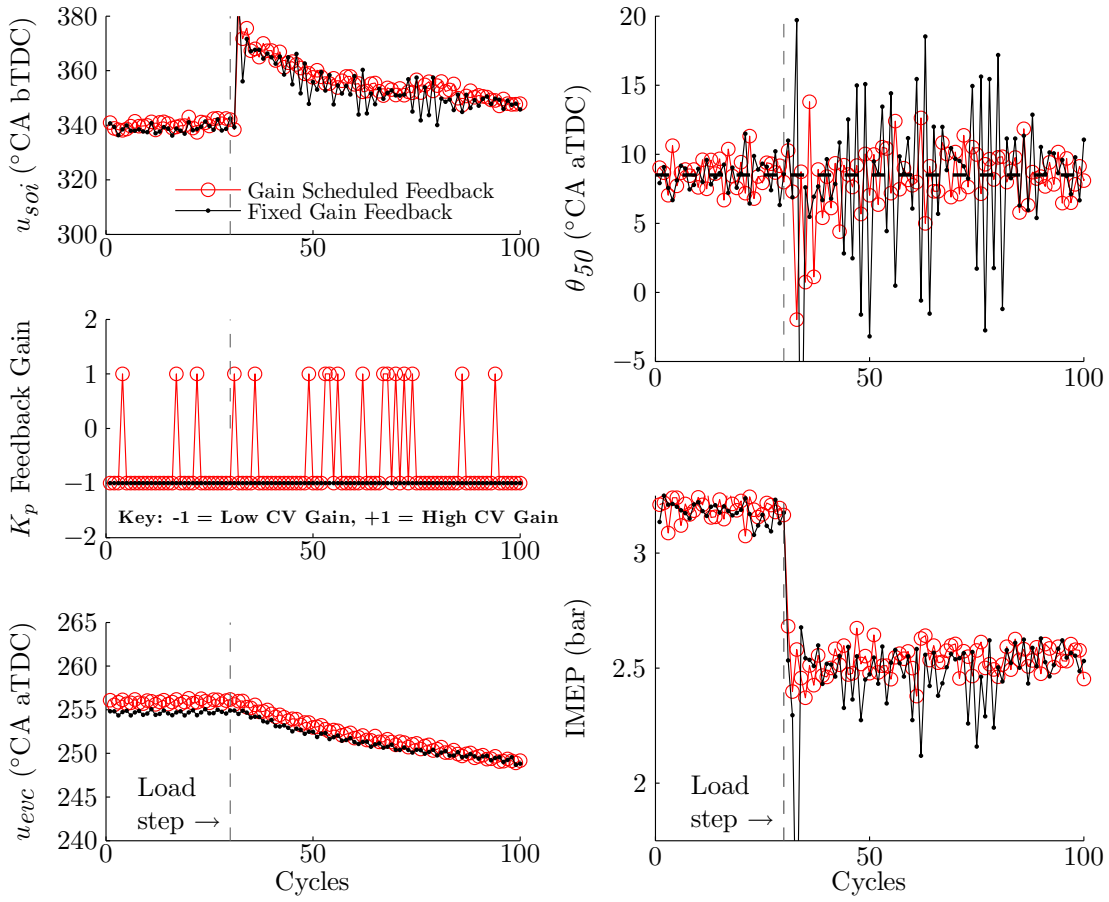

Figure 8.4: Comparison of load transitions for a controller equipped to deal with cyclic variability on and one that is not. When the control detects that CV may be presented the gain fo the feedback signal is flipped for the consequent cycle. This prevents the misfire and also reduces oscillations at steady state.

HCCI operating point. Specifically, u_{evc}=-106° aTDC, SOI=330° bTDC, m_f=10.8mg and an engine speed of 1800RPM. The linearized model inverted at steady state is:

$$x_{ss} = Ax_{ss} + B_{soi}u_{soi}^{ss} + B_{evc}u_{evc} + B_f m_f^{inj} + B_\omega \omega + B_\Theta \Theta$$

$$\theta_{50}^{ref} = Cx_{ss} + D_{soi}u_{soi}^{ss} + D_{evc}u_{evc} + D_f m_f^{inj} + D_\omega \omega + D_\Theta \Theta$$

$$\therefore u_{soi}^{ss} = \begin{bmatrix} 0 \\ 1 \end{bmatrix}^T \begin{bmatrix} (A-I) & B_{soi} \\ C & D_{soi} \end{bmatrix}^{-1} \begin{bmatrix} -B & 0 \\ -D & 1 \end{bmatrix} \left[u_{evc}, m_f^{inj}, \omega, \Theta, \theta_{50}^{ref} \right]^T \tag{8.1}$$

$$\text{where } B = \begin{bmatrix} B_{evc} & B_f & B_\omega & B_\Theta \end{bmatrix}$$
$$\text{and } D = \begin{bmatrix} D_{evc} & D_f & D_\omega & D_\Theta \end{bmatrix}.$$

The feedforward injection timing, u_{soi}^{ss}, is the timing necessary for a given reference combustion phasing assuming all other inputs are at steady state.The reference combustion phasing was set to 8.5° aTDC for these tests. It can also be seen that the equations have been appropriately modified to incorporate the adaptive gain Θ which presents itself in the B and D matrices. The feedforward block is then a fixed gain for a given cycle. Since each cylinder can have a different fuel mass and combustion phasing reference and because u_{evc}, ω and Θ are constantly varying parameters, the controller generates a gain for each cylinder on each cycle. The eigenvalues for this system are real and lie on the positive axis, they are less than 1 and are therefore stable. For significantly later values of u_{evc} the model predicts the onset of high cyclic variability in the form of oscillatory dynamics.

The value of Θ pushes the steady state value of the states closer to that of the actual engine based on the measured combustion phasing. This in turn yields a control u_{soi} which is more accurate.

A graphical representation of the complete system is provided in Fig. 8.1. Here it can be seen how the continuous time system is separated into discrete cycles, where measurements are taken and where inputs are applied. The adaptive algorithm and non-linear model run alongside the midranging controller on the rapid prototyping hardware.

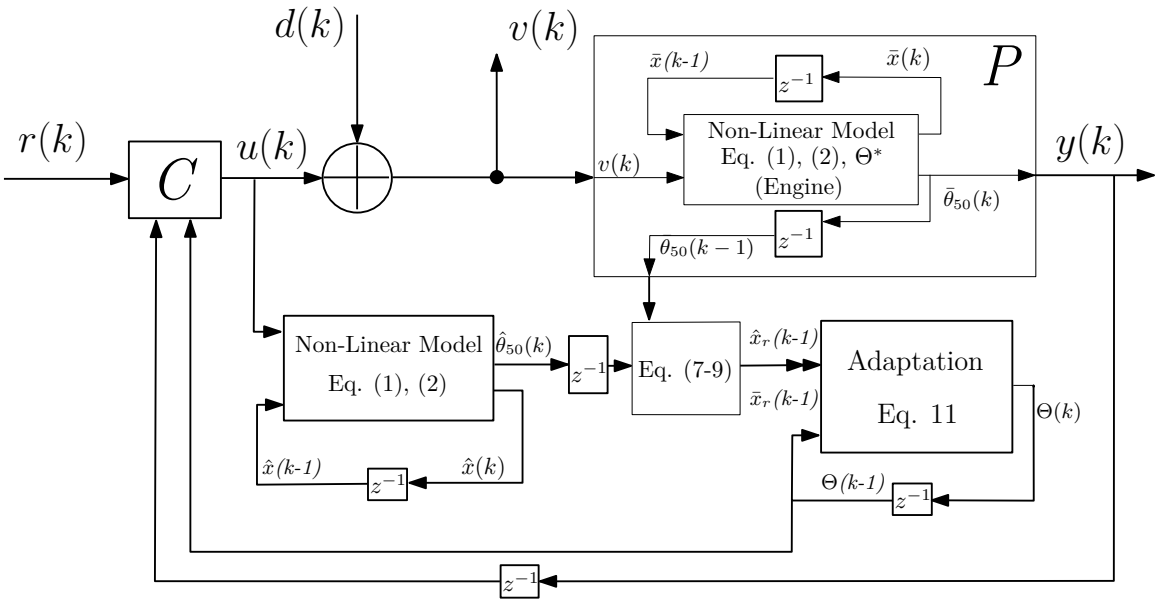

Figure 8.5: Block diagram of complete system as implemented for simulation. The engine is replaced by a linearized model.

8.2.3 Closed Loop System

The system of Fig. 8.1 can be represented in simulation by the block diagram of Fig. 8.5. The signals introduced in the figure are:

$$\text{Reference: } r(k) = \left[\theta_{50}^{ref}(k), \quad m_f^{inj}(k), \quad \omega(k), \quad u_{soi}^{ref}(k)\right]^T \tag{8.2}$$

$$\text{Input: } u(k) = \left[u_{soi}(k), \quad u_{evc}(k), \quad m_f^{inj}(k), \quad \omega(k)\right]^T \tag{8.3}$$

$$\text{Disturbance: } d(k) = \left[\Delta u_{soi}(k), \quad \Delta u_{evc}(k), \quad \Delta m_f^{inj}(k), \quad \Delta\omega(k)\right]^T \tag{8.4}$$

$$\text{Input to Plant: } v(k) = u(k) + d(k) \tag{8.5}$$

$$\text{Output: } y(k) = \theta_{50}(k). \tag{8.6}$$

The plant (P) is the nonlinear model from App. A and the controller (C) is comprised of two parts. One component is the EVC control and the other is the SOI control.

The controllers given in transfer function form as:

$$U_{soi}(z) = \frac{z(z-1)}{z(z-1) + K_{ff}^{evc} K_i^{evc}} \begin{bmatrix} K_p^{soi} + K_{ff}^{50} + \frac{K_i^{soi}}{z-1} \\ -K_p^{soi} - \frac{K_i^{soi}}{z-1} \\ \frac{K_{ff}^{m_f}}{z} \\ K_{ff}^{\omega} \\ 1 \\ \frac{K_{ff}^{evc} K_i^{evc}}{z(z-1)} \end{bmatrix}^T \begin{bmatrix} \Theta_{50}^{ref}(z) \\ \Theta_{50}^{fb}(z) \\ M_f^{inj}(z) \\ \Omega(z) \\ \Theta_{adap}(z) \\ U_{soi}^{ref}(z) \end{bmatrix} \tag{8.7}$$

$$U_{evc}(z) = \frac{K_i^{evc} z}{z(z-1) + K_{ff}^{evc} K_i^{evc}} \begin{bmatrix} -K_p^{soi} - K_{ff}^{50} - \frac{K_i^{soi}}{z-1} \\ K_p^{soi} + \frac{K_i^{soi}}{z-1} \\ -\frac{K_{ff}^{m_f}}{z} \\ -K_{ff}^{\omega} \\ 0 \\ 1 \end{bmatrix}^T \begin{bmatrix} \Theta_{50}^{ref}(z) \\ \Theta_{50}^{fb}(z) \\ M_f^{inj}(z) \\ \Omega(z) \\ \Theta_{adap}(z) \\ U_{soi}^{ref}(z) \end{bmatrix} \tag{8.8}$$

where

$$K_p^{soi} = \begin{cases} K_{p,lowcv}^{soi} & \text{if } \theta_{50}(k) \leq \theta_{50}^{thresh}(m_f^{inj}) \\ K_{p,highcv}^{soi} & \text{if } \theta_{50}(k) > \theta_{50}^{thresh}(m_f^{inj}). \end{cases} \tag{8.9}$$

The values of $\Theta_{50}^{ref}(z)$, $\Theta_{50}^{fb}(z)$, $M_f^{inj}(z)$, $\Omega(z)$, $\Theta_{adap}(z)$ and $U_{soi}^{ref}(z)$ are the z-transforms of $\theta_{50}^{ref}(k)$, $\theta_{50}^{fb}(k)$, $m_f^{inj}(k)$, $\omega(k)$, $\Theta(k)$ and $u_{soi}^{ref}(k)$ respectively.

8.3 Closed Loop Stability

To analyze the internal stability of the system, the four transfer function matrix theorem [105] is applied from inputs r and d to outputs y and v as indicated in Fig. 8.5. The system is given by:

$$\begin{bmatrix} Y \\ V \end{bmatrix} = T_{4TF} \begin{bmatrix} R \\ D \end{bmatrix}, \tag{8.10}$$

where Y, V, R, D are the z-transform representation of the y, v, r, d signals respectively, Eqs (8.2)–(8.6). The four transfer functions can be summarized by:

$$T_{4TF} = \begin{bmatrix} T_O & PS_I \\ S_I C & S_I \end{bmatrix}. \tag{8.11}$$

T_O is the output complementary sensitivity function (from r to y). The closed loop transfer function from input to output ($r(k)$ to $y(k)$) in Fig. 8.5 has poles at

$\{0.997, 0.970, 0.855, 0.664,\ 0.622, 0.383, 0.250, -0.001\}$ which all lie within the unit circle and are therefore stable. The poles which are close to 1 are from the adaptive state and integrators in the controllers. They are being pulled away from 1 by the adaptive gain and closed loop zeros and are therefore not on the edge of instability.

S_I is the input sensitivity function (from d to v). The plant and controller are P and C, respectively, the plant has poles at $\{0.38\ 0.62\}$. Since the plant and controller have no unstable poles, and all poles of the four transfer functions in T_{4TF} are also stable, the four transfer function theorem for multi-variable systems indicates that the closed-loop system is internally stable.

8.4 Experimental results

The adaptive controller was implemented in real-time on the experimental setup from Chapter 2. The model inverted for feedforward control was parameterized with data from one cylinder and then duplicated for the remaining three. Cylinder-to-cylinder variations are large enough to warrant cylinder individual parameterizations however it will be shown through steady state tests that the adaptive controller alleviates this need. Additionally, transient tests will show the controllers ability to perform load steps and correct for modeling errors before and after transitions.

8.4.1 Feedback Effort Reduction

To demonstrate the adaptive controller's ability to correct for modeling errors and uncertainty, a test was run in which the engine was allowed to come to steady state with the baseline controller active, at which point the adaptive gain was applied to the feedforward control. The test was run as close to the linearization point as possible however there are clear cylinder-to-cylinder variations. The effect on the feedforward control can be found in Fig. 8.6, here one can see that at approximately 20 seconds the adaptive gain pushes the feedforward part of the control closer to the set point of 330° indicating that the model is more correctly representing the physical system. Additionally, the total SOI (feedforward plus feedback) remains the same for both the adaptive and non-adaptive.

The effect on the feedforward SOI is further demonstrated in Fig. 8.7 where the feedback effort is observed. It is clear here that feedback effort after the adaptive parameter is activated is reduced and that it tends towards zero. The amount by

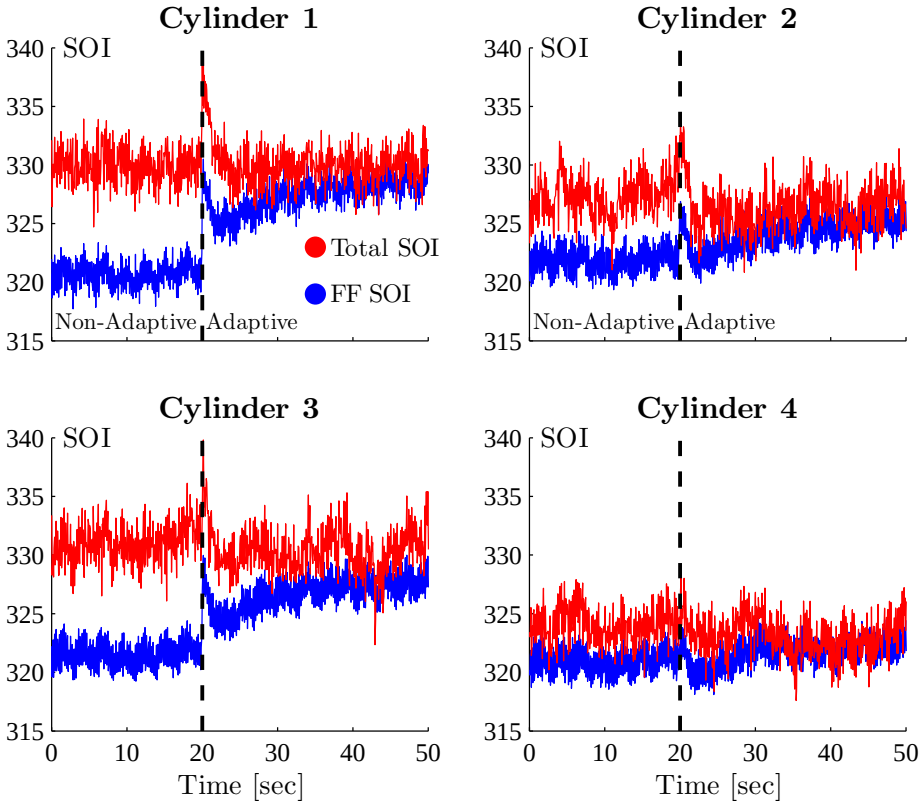

Figure 8.6: The adaptive control makes the model-based feedforward control more accurate when activated at 20 seconds. The result is similar for all 4 cylinders even though they all are at slightly different operating conditions and have the same parameterization.

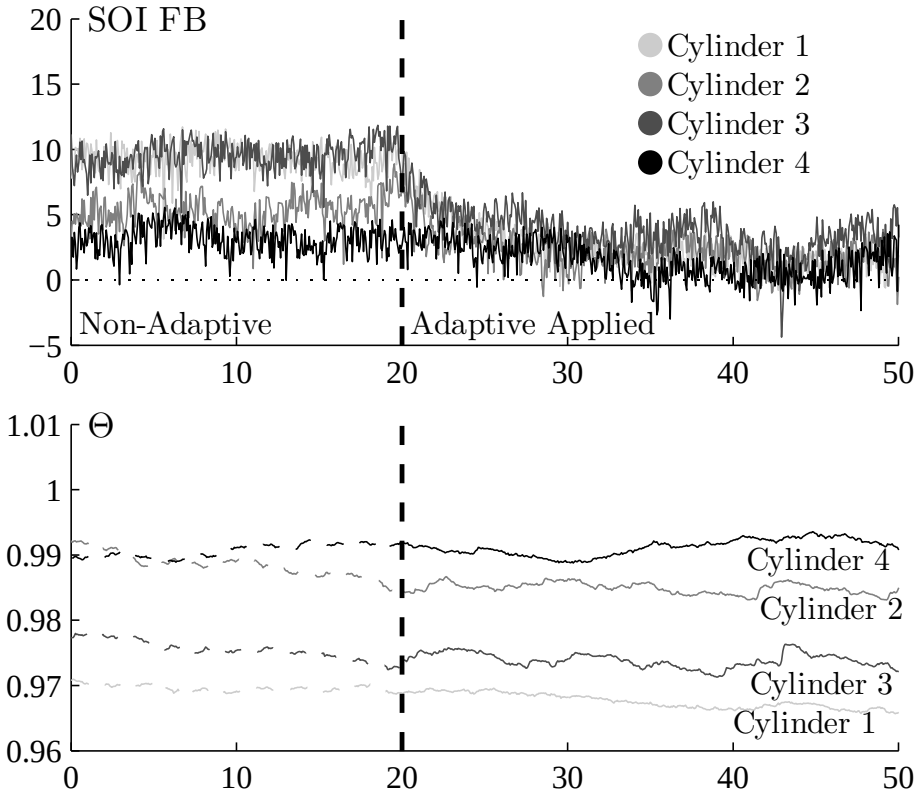

Figure 8.7: The feedback control is minimized by the adaptive gain making the feedforward control more accurate as shown in Fig. 8.6. In addition, the adaptive parameter Θ is shown to go to different values for each cylinder.

which the adaptive gain Θ must modify the model inversion is shown the second plot of Fig. 8.7. The difference in Θ for the 4 cylinders indicates that the model's parameterization for some cylinders was better than for others, deviation from unity indicates more correction by the adaptive parameter. Here the adaptive parameter had already converged prior to the start of the test, however the gain is only applied when indicated. While the gain is applied instantaneously, the control moves slowly because it is dependent on the slow EVC actuator.

8.4.2 Load Steps

Since the feedforward control is linear, deviation from the linearization point can cause errors in the feedforward component of the control. It is the objective of the adaptive controller to mitigate these errors in steady state. To explore this effect fuel steps (load steps) were performed in closed loop with and without the adaptive

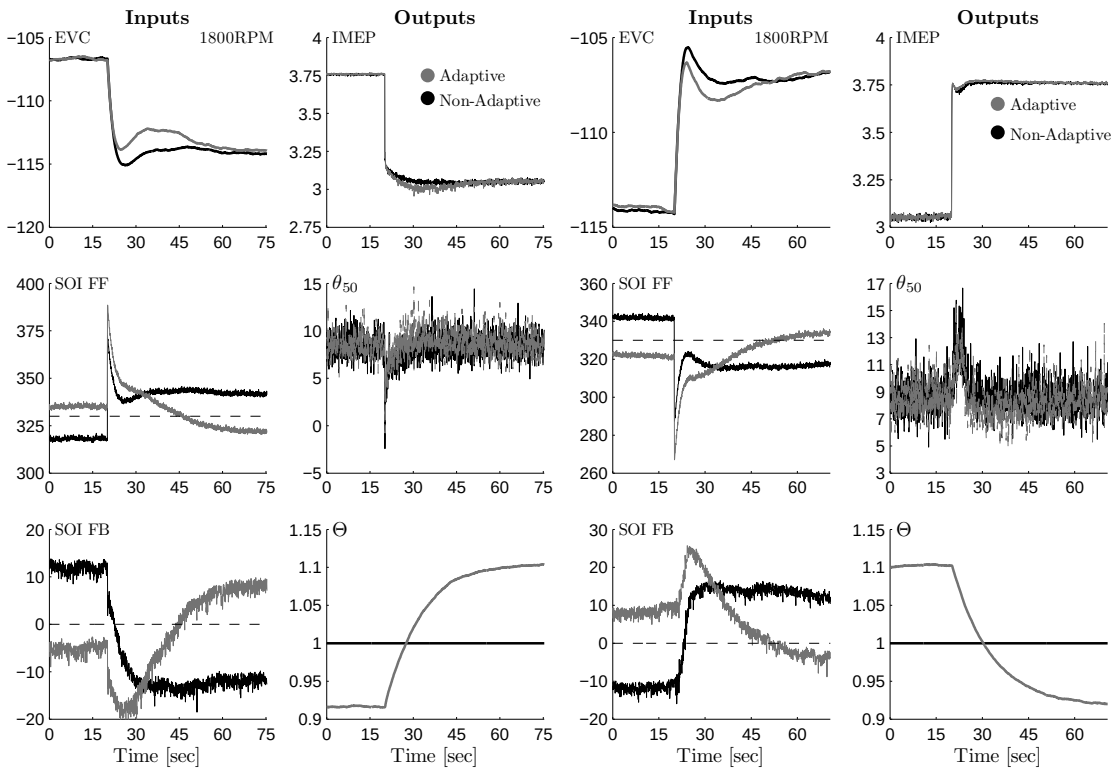

Figure 8.8: A load step from 3.75bar to 3bar IMEP at 1800RPM (left) and a load step from 3bar to 3.75bar IMEP at 1800RPM (right) . Feedforward is more accurate with adaptive control and the transient effort required by EVC is reduced.

controller active. The adaptive controller was designed to be slow, since it is not the objective of the adaptive parameter to change the transient response of the system. The result of a load step down from 3.75bar to 3bar IMEP is found in Fig. 8.8, this is the result for cylinder 1. The transient response with and without the adaptive active is comparable in terms of both torque output and regulation of combustion phasing. However, it can be seen that the controller's feedback effort has been reduced at steady state and because of this the EVC control does less work during the transient.

Similarly, a load step up is observed in Fig. 8.8 where the adaptive control provides a similar result. It should also be noted that for both load steps the adaptive parameter stays within the region where the effect on the system is approximately linear. In an ideal scenario, the adaptive parameter should push the feedback control component to zero, however small changes to the system, such as in the temperature and pressure of the intake manifold, can cause errors. The inclusion of non-linear feedforward could help compensate for these small differences however the adaptive linear inversion is already very accurate at these operating conditions.

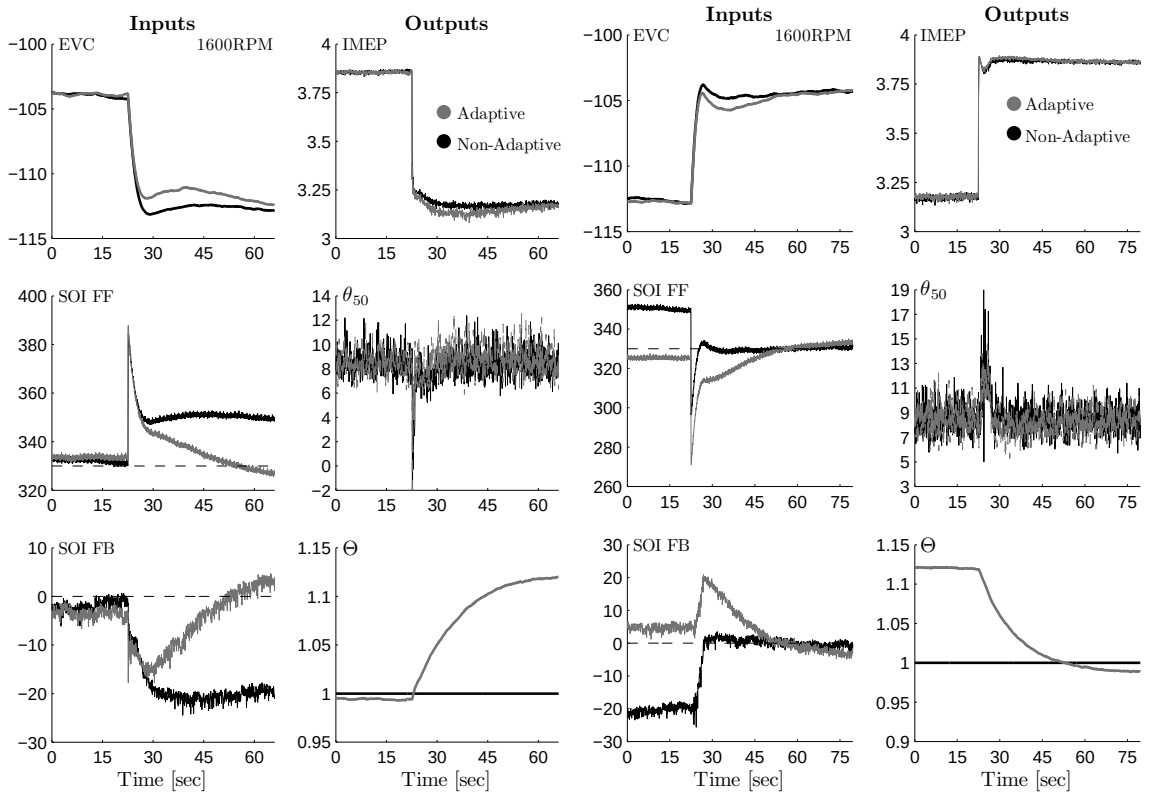

Figure 8.9: A load step from 3.8bar to 3.25bar IMEP (left) and a load step from 3.8bar to 3.25bar IMEP at 1600RPM. A significant improvement in the feedforward component of SOI control is seen at 3.25bar. The transient effort of EVC is also reduced during the transition. The feedforward is accurate at 3.8bar and the adaptive parameter Θ is close to 1.

8.4.3 Speed Variation

To quantify the controllers performance away from the linearization point similar load steps to that of Sec. 8.4.2 were run at 1600RPM, a load step down is shown in Fig. 8.9. The feedforward controller has knowledge that the speed has changed to 1600RPM and the model inversion is accurate at approximately 3.8bar IMEP. Specifically, the feedforward SOI is close to the set point and Θ is close to unity. However, when the load is stepped down to 3.25bar the feedforward in steady state is very far from the set point and the slow EVC controller is required to do more work. This is despite the fact that engine speed enters into the inversion of the model in the B matrix of Eq. (8.1). When the same transition is made with the adaptive control active, the SOI feedforward quickly returns to the set point and the feedback tends to zero resulting in less EVC effort during the transition. A load step up in Fig. 8.9 shows similar behavior, the feedforward controller's performance is improved at 3.25bar.

8.4.4 Experimental Conclusions

Table 8.1 presents a quantitative summary of the adaptive control results through the absolute value of the steady state feedback SOI. Specifically, it can be seen that the feedback required for nearly all test is significantly reduced when using the adaptive control. The exception is before the load step down at 1600RPM, however at this point the feedforward control is already very good without adaptation and so there is little room for improvement. Over all tests, the average reduction in the absolute value SOI feedback at steady state was 41%.

Table 8.1: Steady state SOI feedback effort before and after load steps. Results shown as $^{Non-Adaptive}/_{\mathbf{Adaptive}}$ in crankangle degrees.

	1800RPM		**1600RPM**	
Step	Down	Up	Down	Up
Before	$^{11.82}/_{\mathbf{-5.27}}$	$^{-11.85}/_{\mathbf{7.83}}$	$^{-2.48}/_{\mathbf{-3.24}}$	$^{-17.92}/_{\mathbf{5.07}}$
After	$^{-11.59}/_{\mathbf{8.06}}$	$^{12.26}/_{\mathbf{-3.72}}$	$^{-19.50}/_{\mathbf{2.70}}$	$^{-3.12}/_{\mathbf{-2.79}}$

8.5 Summary

An adaptive control scheme has been developed and evaluated through simulations and experiments. The use of an adaptive parameter in the feedforward control helps to improve the accuracy of the controller at steady state. An average reduction in steady state SOI feedback effort of 41% was achieved. This allows the system to make transitions using mostly feedforward control, which reduces the effort required by the slow EVC actuator. This is particularly useful when using linear model inversion because any transition will deviate from the linearization point. The adaptive control could also be used to correct feedforward tables or non-linear model inversions.

Additionally, a stability analysis has been performed for both the adaptive parameter estimation scheme and the full closed loop system. It has been shown that for small gains the adaptive state is stable and that the closed loop system is internally stable for typical engine operating conditions. Future work includes extending the feedforward controller to a non-linear model inversion and using adaptive parameter estimation to further improve the control for the onset of cyclic variability in load transitions.

Chapter 9

Conclusions and Future Work

9.1 Conclusions and Results

Stringent caps on automotive emissions and an increasing demand for high fuel efficiency engines has generated many challenges and opportunities to the automotive industry. The prospect of low-temperature combustion, specifically homogeneous charge compression ignition (HCCI), presents a promising solution to some of these issues. HCCI is characterized by high thermal efficiency and low engine-out emissions, however it is restricted in the speed-load operating space due to high variability and ringing and can be difficult to control because it lacks a direct method of ignition. The work presented in this dissertation provides several advancements in the understanding of high variability dynamics in HCCI as well as methods for control of cyclic variability (CV) and load transitions. A summary of the contributions is as follows:

1. Cycle-by-Cycle Data Analysis and Real-Time Residual Estimation:

   Standard pressure based combustion analysis methods have been extended for use with highly variable data sets. Additionally, the analysis is applied during the negative valve overlap (NVO) period. This analysis is key to the understanding of the dynamics of high variability. Tracking of the amount of unburned fuel mass and heat release during NVO sheds light on the deterministic features which dominate the seemingly chaotic combustion.

   A method of determining the trapped residual gas in recompression combustion in real time has been developed and analyzed. The algorithm is capable of handling highly variable data which is important because the residual gas fraction has a profound effect on the combustion. If too much residual mass is trapped the combustion can occur very early causing potential engine damage and a loss in efficiency. If too little mass is trapped the combustion can become highly oscillatory and misfires may occur.

2. Cyclic Variability Analysis, Modeling and Control:

   Experiments were performed to explore three modes of instability in HCCI: throttled stoichiometric, thermal run-away and lean-late phasing combustion. For each test performed, 3000 consecutive engine cycles were

recorded. This is an order of magnitude more data than is typically collected in literature. Large data sets are necessary to observe the evolution of some dynamic patterns and to establish statistical relevance. The experiments were evaluated using the cycle resolved combustion analysis tools presented in Chapter 3 and the results demonstrate that each mode has different dynamic behavior. Despite the high level of cyclic dispersion observed at each mode, it is clear that each is dictated by dominate deterministic couplings. This understanding has lead to the formation of a model for the lean-late phasing combustion which is parameterized and validated against actual engine data.

The lean-late phasing model captures both recycled thermal and chemical energy dynamics. It contains two states which are control oriented, and physics based. In Chapter 6 the model is used to develop controllers to reduce CV at steady state. Two controllers are designed: a simple proportional controller and an optimal Linear Quadratic Gaussian (LQG) regulator. Both controllers are augmented with slow integral control so that late phasing can be maintained. The controllers were tuned using the model and then implemented on the 4 cylinder engine. To test their abilities they were run a three levels of CV. The controllers performed well, reducing the variability in all cases for all cylinders. However, the PI control proved to be more robust than the LQG due to the fact that it is difficult to maintain the engine at the particular point for which the LQG controller was designed.

3. Adaptive Model and Control:

   In Chapters 7 and 8 the knowledge obtained by reducing the CV in steady state is used to help control large load transients. This is achieved through a mid-ranging controller with an adaptive feedforward component. The online residual mass estimation state from Chapter 4 and the model from App. A are combined to create a three state model for the prediction of combustion phasing. An adaptive parameter estimation scheme is developed and implemented in real time on the engine. It is demonstrated that the adaptive model can correct for modeling errors and parameter drift. Additionally, a stability analysis of the adaptive state is done along with simulations to explore its authority over the model's states and output.

   This model is then inverted for feedforward control and coupled with a baseline midranging controller for use on load transitions. The feedback component of the controller is gain scheduled based on the detection of CV through a measurement of combustion phasing. One feedback gain is used for stable combustion and another is for high CV combustion. The gains must be of opposite sign because of the position of the eigenvalues for stable versus oscillatory combustion. A stabilizing gain for one system is a destabilizing gain for another.

Experimental results show that the controller is capable of navigating large load transients while avoiding excessive amounts of variability. The adaptive component makes the feedforward control more accurate when away from the linearization point. This allows the actuators to spend more time in a region of greatest authority so that they may be better prepared for future transients. This is critical for useful implementation of a combustion concept since an engine is rarely at steady state but rather making constant transitions. The adaptive routine has the added benefit that it can reduce the parameterization effort required by a multi-cylinder engine.

9.2 Future Work and Open Problems

The combustion analysis techniques could be extended to include a two zone heat release analysis. This could be useful for analysis of more complicated combustion modes such as spark assisted compression ignition (SACI) where there are portions of the charge which are burned and unburned simultaneously due to the propagation of a flame front. Additionally, a study could be performed as to the effect of early combustion phasing on heat transfer. Currently the analysis yields slightly low combustion efficiencies for early phasings. However this could be caused by increased turbulence and heat transfer since the piston is near TDC. There is currently now way for these effects to be captured.

Further analysis should be done to understand and model the onset of CV for lower loads. It is a well know fact that when operating at lower loads the combustion efficiency can decrease due to insufficient peak temperatures and the inability to convert CO to CO_2 as shown in [106]. Characterization of this would require adding a second dimension of peak cylinder temperature to the parameterization of combustion efficiency, which is currently only a function of the combustion phasing. Increasing our understanding about the onset of CV could allow one to better map this threshold for the onset of CV and prevent poor combustion. This can allow for faster and smoother load transitions.

In the future, knowledge about the onset of CV should help to form a more comprehensive model. The goal would be to have a CV model which is capable of predicting the stable combustion dynamics in addition to the lean late phasing and thermal runaway events, the full range of possible HCCI combustion phasings. This model could then be exploited for predictive control of the combustion to perhaps extend the load range of HCCI and make larger and faster load transitions possible, better enabling HCCI for commercial implementation. The adaptive feedforward controller could

also be improved through this global model. The use of a non-linear model inversion with the adaptive parameter estimation could make transitions achievable with little feedback effort, this would allow for large and fast speed and load transitions within the HCCI operating space.

Appendices

Appendix A

Control Oriented Two State Model

The following sections provide an overview of the two state model from [38, 39, 58]. The model can be summarized by Eqs. (7.1) and (7.2) in Sec. 5.5.

Combustion Phasing

Autoignition is predicted using the integrated Arrhenius rate threshold model using a fixed activation temperature ($B = \frac{E_a}{R_u}$) and pre-exponential factor A. The integration is carried out until the threshold (K_{th}) is hit at the start of combustion (θ_{soc}). The model can be expressed as follows:

$$\begin{aligned} K_{th}(\theta_{soi}) &= k_0 - u_{soi} \\ &= \int_{\theta_{ivc}}^{\theta_{soc}(k-1)} \frac{A}{\omega} p_c(\theta)^{n_p} \exp\left(\frac{B}{T_c(\theta)}\right) \mathrm{d}\theta \end{aligned} \tag{A.1}$$

The pressure (p_c) and temperature (T_c) of the charge in the cylinder are given by a polytropic compression:

$$\begin{aligned} p_c(\theta) &= p_{ivc}(k-1)\left(\frac{V_{ivc}}{V(\theta)}\right)^n, \\ T_c(\theta) &= T_{ivc}(k-1)\left(\frac{V_{ivc}}{V(\theta)}\right)^{n-1}. \end{aligned} \tag{A.2}$$

The output θ_{50} is modeled as a linear function of θ_{soc}:

$$\theta_{50}(k-1) = b_1 \theta_{soc}(k-1) + b_0. \tag{A.3}$$

For a restricted range of operating conditions, the prediction of combustion phasing can be well approximated by a quadratic whose coefficients vary as linear functions

of injection timing:

$$\begin{aligned}\theta_{50}(k-1) =& \alpha_{\theta 1}(soi)T_{ivc}^2(k-1)+ \\ & \alpha_{\theta 2}(soi)T_{ivc}(k-1) + \alpha_{\theta 3}(soi)\end{aligned} \tag{A.4}$$

In-cylinder Temperature

Combustion is thermally modeled as an instantaneous heat release at θ_{50} concatenated with a polytropic compression from θ_{ivc} and a polytropic expansion to θ_{evo}. The charge temperature after combustion (T_{ac}) and the temperature rise due to combustion (ΔT) are given by:

$$T_{ac}(k-1) = T_{ivc}(k-1)\left(\frac{V_{ivc}}{V_c}\right)^{n-1} + \Delta T(k-1) \tag{A.5}$$

$$\begin{aligned}\Delta T(k-1) &= \eta_m(k-1)\frac{q_{lhv}m_f(k-1)}{c_v(k-1)m_c(k-1)} \\ &= \frac{\eta_m(k-1)q_{lhv}R}{c_v(k-1)p_{ivc}V_{ivc}}m_f(k-1)T_{ivc}(k-1).\end{aligned} \tag{A.6}$$

Here η_m is the combustion efficiency, and n is the polytropic exponent. The specific heat of combustion c_v varies as a function of composition (b_c) to capture variations in mixture properties.

$$\eta_m(k-1) = \frac{a_0}{1+\exp\left\{\frac{\theta_{50}(k-1)-a_1}{a_2}\right\}}\left(1+a_3\omega(k-1)\right) \tag{A.7}$$

$$c_v(k-1) = 1 + a_5 b_c(k-1) \tag{A.8}$$

Polytropic expansion after combustion gives the charge temperature at θ_{evo}, (T_{evo}), to be:

$$\begin{aligned}T_{evo}(k-1) &= T_{ac}(k-1)\left(\frac{V_c}{V_{evo}}\right)^{n-1} \\ &= T_{ivc}(k-1)\left(\frac{V_{ivc}}{V_{evo}}\right)^{n-1} \\ &\quad \left[1+\frac{\eta_m(k-1)q_{lhv}R{V_c}^{n-1}}{c_v p_{ivc}{V_{ivc}}^n}m_f(k-1)\right].\end{aligned} \tag{A.9}$$

Using the ideal gas law, the pressure at θ_{evo} is:

$$\begin{aligned} p_{evo}(k-1) = & p_{ivc}(k-1)\frac{V_{ivc}}{V_{evo}}\frac{T_{evo}(k-1)}{T_{ivc}(k-1)} \\ = & p_{ivc}(k-1)\left(\frac{V_{ivc}}{V_{evo}}\right)^{n} \\ & \left[1+\frac{\eta_m(k-1)q_{lhv}RV_c{}^{n-1}}{c_v p_{ivc}V_{ivc}{}^{n}}m_f(k-1)\right]. \end{aligned} \tag{A.10}$$

Expansion is followed by the blowdown process, which is modeled as a polytropic expansion from the pressure at θ_{evo}, (p_{evo}), to the exhaust manifold pressure (p_{em}), with the polytropic exponent n. The temperature at blowdown (T_{bd}) is:

$$\begin{aligned} T_{bd}(k) = & T_{evo}(k-1)\left(\frac{p_{evo}(k-1)}{p_{em}}\right)^{\frac{1-n}{n}} \\ = & T_{ivc}(k-1)\left(\frac{p_{ivc}(k-1)}{p_{em}}\right)^{\frac{1-n}{n}} \\ & \left[1+\frac{\eta_m(k-1)q_{lhv}RV_c{}^{n-1}}{c_v p_{ivc}(k-1)V_{ivc}{}^{n}}m_f(k-1)\right]^{\frac{1}{n}}. \end{aligned} \tag{A.11}$$

Coupling between Cycles

In recompression HCCI a large fraction of the in-cylinder charge is trapped before it can be exhausted. The hot residual gases retained between engine cycles have a significant impact on the temperature and composition of the in-cylinder charge of the subsequent cycle. This internal coupling between cycles is quantified by the residual gas fraction (x_r). In the model presented in [38, 39] the residual gas fraction was a static function for a given exhaust valve closing timing θ_{evc}, temperature of blowdown gases T_{bd}, engine speed ω, and pressure ratio across the engine Π:

$$\begin{aligned} x_r(k-1) = & 1-(c_0+c_1\theta_{evc}) \\ & \Pi^{c_2}T_{bd}(k-1)^{c_3}\omega(k-1)^{c_4} \\ & \text{where } \Pi = \frac{p_{im}(k-1)}{p_{em}(k-1)}. \end{aligned} \tag{A.12}$$

Thermal Coupling

The cooling of the charge from θ_{evo} to θ_{evc} is modeled by a scaling constant c_e. This cooled charge is polytropically compressed and expanded during the NVO region to

obtain the residual gas temperature.

$$T_{evc}(k) = c_e T_{bd}(k) \tag{A.13}$$

$$T_{soi}(k) = T_{evc}(k)\left(\frac{V_{evc}}{V_{soi}}\right)^{n-1} - a_4 m_f(k-1) \tag{A.14}$$

$$T_{res}(k) = T_{soi}(k)\left(\frac{V_{soi}}{V_{ivo}}\right)^{n-1} \tag{A.15}$$

$$T_{res}(k) = \left[c_e T_{bd}(k)\left(\frac{V_{evc}}{V_{soi}}\right)^{n-1} - a_4 m_f(k-1)\right]\left(\frac{V_{soi}}{V_{ivo}}\right)^{n-1} \tag{A.16}$$

The thermal coupling between cycles is modeled by an energy balance equation at θ_{ivc}. The temperature of the hot residuals is assumed to be T_{res} while the rest of the charge is considered to be at the intake manifold temperature (T_{im}). Assuming constant specific heats, an energy balance leads to:

$$\begin{aligned} T_{ivc}(k-1) =& x_r(k-1)T_{res}(k-1)+ \\ & (1 - x_r(k-1))\, T_{im}. \end{aligned} \tag{A.17}$$

Composition Coupling

The burned gas fraction before (b_c) and after (b_{bd}) combustion can be related by simple equations that assume that the fuel combines with a stoichiometric mass of air to form an equal mass of burned gases. Further, an x_r portion of the burned gases is trapped between cycles:

$$b_c(k-1) = x_r(k-1)b_{bd}(k-1) \tag{A.18}$$

$$\begin{aligned} b_{bd}(k+1) &= \frac{(AFR_s + 1)\, m_f(k-1)}{m_c(k-1)} + b_c(k-1) \\ &= \frac{(AFR_s + 1)\, R}{p_{ivc}V_{ivc}} T_{ivc}(k-1)m_f(k-1) + b_c(k-1). \end{aligned} \tag{A.19}$$

Appendix B
Model Coefficients

B.1 HCCI Model Coefficients

The two-state HCCI model for low CV conditions is presented in Chap. 7. The numerical values of the parameters and constants used in this model are listed in Tab. B.1 and Tab. B.2 respectively.

Table B.1: HCCI Combustion Model Coefficients

Symbol	Value	Description	References
c_0	-0.21277	x_r regression: constant u_{evc} term	Eq. (A.12), (7.4), (7.16)
c_1	0.002180	x_r regression: linear u_{evc} term	Eq. (A.12), (7.4), (7.16)
c_2	-0.61611	x_r regression: pressure ratio exponent	Eq. (A.12), (7.4), (7.16)
c_3	0.80054	x_r regression: T_{bd} exponent	Eq. (A.12), (7.4), (7.16)
c_4	-0.25650	x_r regression: ω exponent	Eq. (A.12), (7.4), (7.16)
c_e	0.6886	Scaling constant for temperature drop during exhaust	Eq. (A.13)
a_0	0.89	Combustion efficiency sigmoid: scaling term	Eq. (A.7)
a_1	34.9	Combustion efficiency sigmoid: offset term	Eq. (A.7)

Continued on next page

Table B.1 – continued from previous page

Symbol	Value	Description	References
a_2	4.9	Combustion efficiency sigmoid: shape term	Eq. (A.7)
a_3	1.997	Combustion efficiency sigmoid: speed term (constant)	Eq. (A.7)
a_4	3.457×10^{-4}	Combustion efficiency sigmoid: speed term (linear)	Eq. (A.7)
a_5	2.6563	Specific heat correction term	Eq. (A.8)
A	1286	Arrhenius pre-exponential factor	Eq. (A.1)
B	-11280	Arrhenius pre-exponential factor	Eq. (A.1)
n_p	4.51	Arrhenius pressure exponent	Eq. (A.1)
k_0	408	Arrhenius threshold offset term	Eq. (A.1)
b_0	2.908	Combustion duration offset term	Eq. (A.2)
b_1	1.306	Combustion duration linear term	Eq. (A.3)

Table B.2: HCCI Combustion Model Constants

Symbol	Value	Description	References
n	1.3	Polytropic exponent	Eq. (A.2), (A.5), (A.9), (A.10), (A.11), (A.14), (A.15), (A.16), (7.1)
q_{lhv}	44×10^3	Lower heating value of fuel	Eq. (A.6), (A.9), (A.11), (7.1)
R	288.3	Gas constant	Eq. (A.6), (A.9), (A.10), (A.11), (A.14), (7.1)
AFR_s	14.7	Stoichiometric air-fuel mass ratio	Eq. (A.18), (A.19), (7.2)

Appendix C

List of Abbreviations

HCCI	Homogeneous charge compression ignition
PM	Particulate matter
NO_x	Nitrous oxide emissions
CV	Cyclic variability
ACCESS	Advanced combustion control – enabling systems and solutions
SULEV	Super ultra low emission vehicle
SI	Spark ignited
TDC	Top dead center
BDC	Bottom dead center
ECU	Engine control unit
IMEP	Indicated mean effective pressure
CoV	Coefficient of variation
m_f	Fuel mass per cycle
m_{res}	Trapped residual mass
m_c	Mass of total charge
x_r	Residual gas fraction
$\eta_{m/n}$	Main/NVO combustion efficiency
c_v	Specific heat for a given composition
R	Gas constant for a given composition
q_{lhv}	Heating value of the fuel
AFR_s	Stoichiometric air-fuel ratio
SOI	Start of injection
EVO/C	Exhaust valve open/close
IVO/C	Intake valve open/close
NVO	Negative valve overlap
ω	Engine speed
V	Cylinder volume

θ_x	Crank angle of position x
θ_{50}	Measured crank angle of 50% burned
$\hat{\theta}_{50}$	Model prediction of θ_{50}
T	Temperature
P	Pressure
λ	Air-fuel ratio
κ	Adaptive gain
Θ	Adaptive parameter
$T_{ivc,e}$	An estimate of T_{ivc} based on model inversion
cad	Crank angle degrees
RMS	Root mean square

Appendix D
Publications

D.1 Journal Publications

1. E. Hellström, J. Larimore, J. Sterniak, L. Jiang, and A. Stefanopoulou, "Quantifying Cyclic Variability in a Multi–Cylinder HCCI Engine with High Residuals," *Journal of Engineering for Gas Turbines and Power, 2012–81107* [70]
2. E. Hellström, J. Larimore, S. Jade, A. Stefanopoulou, and L. Jiang, "Reducing cyclic variability while regulating combustion phasing in a four-cylinder HCCI engine," *IEEE Transactions on Control Systems Technology*, 2013, To Appear [90].
3. S. Jade, E. Hellström, J. Larimore, L. Jiang, and A. Stefanopoulou, "Reference Governor for Load Control in a Multi-Cylinder Recompression HCCI Engine," *IEEE Transactions on Control Systems Technology*, 2013, To Appear [58].
4. S. Jade, J. Larimore, E. Hellström, L. Jiang, and A. Stefanopoulou, "Controlled Load and Speed Transitions in a Multi-Cylinder Recompression HCCI Engine," *IEEE Transactions on Control Systems Technology*, 2014, To Appear. [107].
5. J. Larimore, S. Jade, E. Hellström, L. Jiang, and A. Stefanopoulou, "Adaptive Control of a Recompression 4-Cylinder HCCI Engine," *IEEE Transactions on Control Systems Technology*, 2013, Submitted for Review [108].

D.2 Conference Publications

6. J. Larimore, E. Hellström, J. Sterniak, L. Jiang, and A. Stefanopoulou, "Experiments and Analysis of High Cyclic Variability at the Operational Limits of Spark–Assisted HCCI Combustion," *In Proc. American Controls Conference, 2012* [23]
7. E. Hellström, J. Larimore, J. Sterniak, L. Jiang, and A. Stefanopoulou, "Quantifying Cyclic Variability in a Multi–Cylinder HCCI Engine with High Residuals," *In Proc. ASME Internal Combustion Engine Division Spring Technical Conference, 2012* [70]
8. J. Larimore, S. Jade, E. Hellström, L. Jiang, and A. Stefanopoulou, "Controlling Combustion Phasing Variability with Fuel Injection Timing in a Multi–Cylinder

HCCI Engine," *In Proc. American Controls Conference, 2013* [85]

9. S. Jade, J. Larimore, E. Hellström, L. Jiang, and A. Stefanopoulou, "Enabling Large Load Transitions on Multicylinder Recompression HCCI Engines using Fuel Governors," *In Proc. American Controls Conference, 2013* [39]
10. J. Larimore, S. Jade, E. Hellström, L. Jiang, and A. Stefanopoulou, "Online Adaptive Residual Mass Estimation in a Multicylinder Recompression HCCI Engine," *In Proc., Dynamic Systems and Control Conference, 2013* [109]

D.3 Patent Applications

11. E. Hellstrom, J. Larimore, L. Jiang, and A. Stefanopoulou, "Predictive Modeling and Reducing Cyclic Variability in Autoignition Engines." 2013, Application filed, Patent App. No.: 13/624539 [110]
12. E. Hellstrom, J. Larimore, L. Jiang, and A. Stefanopoulou, "Dynamic Estimator for Determining Operating Conditions in an Internal Combustion Engine." 2013, Application filed, Patent App. No.: 13/621527 [111]
13. J. Larimore, S. Jade, L. Jiang, E. Hellstrom, A. Stefanopoulou, and J. Vanier, "Device and method for real-time residual gas estimation," 2013, Application filed, Patent App. No.: 61/766754 [112].

Bibliography

[1] T. Wallington, J. Sullivan, and M. Hurley, "Emission of CO_2, CO, NO_x, HC, PM, HFC-134a, N_2O and CH_4 from the Global Light Duty Vehicle Fleet," *Meteorologische Zeitschrift*, vol. 17, no. 2, pp. 109–116, 2008. [Online]. Available: http://www.ingentaconnect.com/content/schweiz/mz/2008/00000017/00000002/art00002 x, 2

[2] F. An and A. Sauer, "Comparison of Actual and Projected Fuel Economy for New Passenger Vehicles," *Centre for Climate and Energy Solutions*, 2012. [Online]. Available: [Accessed12-Jan-2014];http://www.c2es.org/federal/executive/vehicle-standards/fuel-economy-comparison x, 1, 3

[3] W. U. Guzzella, L. and R. Martin, "IC-Engine Downsizing and Pressure-Wave Supercharging for Fuel Economy," *SAE Tech. Paper*, no. 2000-01-1019, 2000. 1

[4] P. Soltic, "Part-Load Optimized SI Engine Systems," Ph.D. dissertation, Swiss Federal Institute of Technology, Zuřich, 2000. 1

[5] S. Onishi, S. Hong Jo, K. Shoda, P. Do Jo, and S. Kato, "Active thermo atmospheric combustion (atac) - a new combustion process for internal combustion engines," *SAE Paper*, vol. 790501, 1979. 2

[6] M. Noguchi, Y. Tanaka, T. Tanaka, and Y. Takeuchi, "A study on gasoline engine combustion by observation of intermediate reactive products during combustion," *SAE Paper*, vol. 790840, 1979. 2

[7] P. Najt and D. Foster, "Compression-ignited homogeneous charge combustion," *SAE paper*, vol. 830264, 1983. 2, 11

[8] R. Thring, "Homogeneous-charge compression-ignition (HCCI) engines," *SAE Paper*, vol. 892068, 1989. 2

[9] "Honda readies activated radical combustion two-stroke engine for production motorcycle," *Automotive Engineer*, pp. 90–92, Jan 1997. 2

[10] M. Yao, Z. Zheng, and H. Liu, "Progress and recent trends in HCCI engines," *Prog. in Ener. and Comb. Sci.*, vol. 35, no. 5, pp. 398–437, Oct. 2009. 3, 27

[11] J. Willand, R. Nieberding, G. Vent, and C. Enderle, "The knocking syndrom – its cure and its potential," *SAE Technical Papers*, vol. 982483, 1998. 3, 11, 27

[12] K. L. Knierim, S. Park, J. Ahmed, A. Kojic, I. Orlandini, and A. Kulzer, "Simulation of misfire and strategies for misfire recovery of gasoline HCCI," *American Control Conf.*, pp. 3947–3952, Jun. 2008. 4

[13] C. G. Mayhew, K. L. Knierim, N. A. Chaturvedi, S. Park, J. Ahmed, and A. Kojic, "Reduced-order modeling for studying and controlling misfire in four-stroke HCCI engines," *48th IEEE Conference on Decision and Control*, pp. 5194–5199, 2009. 4

[14] C. Chiang and A. G. Stefanopoulou, "Stability analysis in homogeneous charge compression ignition (HCCI) engines with high dilution," *IEEE Trans. on Cont. Sys. Tech.*, vol. 15, no. 2, pp. 209–219, March 2007. 5, 46, 56, 97

[15] K. Knierim, S. Park, J. Ahmed, A. Kojic, I. Orlandini, and A. Kulzer, "Simulation of Misfire and Strategies for Misfire Recovery of Gasoline HCCI," *2008 American Control Conference*, pp. 3947–3952, 2008. 5, 56

[16] C. Mayhew, K. Knierim, N. Chaturvedi, S. Park, J. Ahmen, and A. Kojic, "Reduced-order Modeling for Studying and Controlling Misfire in Four-Stroke HCCI Engines," *Proc. of the 48th IEEE Conference on Decision and Control*, pp. 5194–5199, 2009. 5, 56

[17] N. Ravi, H. Liao, A. Jungkunz, and J. Gerdes, "Modeling and control of exhaust recompression HCCI using split injection," *2010 American Control Conference*, 2010. 5, 56

[18] E. Hellström and A. Stefanopoulou, "Modeling cyclic dispersion in autoignition combustion," in *Proc. 50th IEEE Conference on Decision and Control*, Orlando, FL, USA, 2011, pp. 6834–6839. 5, 27, 46, 53, 56, 66, 70

[19] E. Hellström, A. G. Stefanopoulou, J. Vávra, A. Babajimopoulos, D. Assanis, L. Jiang, and H. Yilmaz, "Understanding the dynamic evolution of cyclic variability at the operating limits of HCCI engines with negative valve overlap," *SAE Int. J. Engines*, vol. 5, no. 3, 2012. 5, 20, 25, 46, 53, 56, 97

[20] C. S. Daw, R. M. Wagner, K. D. Edwards, and J. B. G. Jr., "Understanding the transition between conventional spark-ignited combustion and HCCI in a gasoline engine," *Proc. of the Combustion Institute*, vol. 31, no. 2, pp. 2887–2894, 2007. 5, 46

[21] C. Daw, K. Edwards, R. Wagner, and J. J.B. Green, "Modeling cyclic variability in spark-assisted HCCI," *J. Eng. Gas Turbines Powe*, vol. 130, no. 5, p. 052801, 2008. 5, 46, 52

[22] M. Havstad, S. Aceves, M. McNenly, W. Piggott, D. Edwards, R. Wagner, C. Daw, and C. Finney, "Detailed chemical kinetic modeling of iso-octane SI-HCCI transition," in *SAE World Congress*, 2010, 10PFL-0840. 5, 52

[23] J. Larimore, E. Hellström, J. Sterniak, L. Jiang, and A. Stefanopoulou, "Experiments and analysis of high cyclic variability at the operational limits of spark-assisted HCCI combustion," in *Proc. ACC*, Montréal, Canada, 2012, pp. 2072–2077. 5, 91, 122

[24] B. T. Zigler, P. E. Keros, K. B. Helleberg, M. Fatouraie, D. Assanis, and M. S. Wooldridge, "An experimental investigation of the sensitivity of the ignition and combustion properties of a single-cylinder research engine to spark-assisted HCCI," *International Journal of Engine Research*, vol. 12, no. 4, pp. 353–375,

2011. [Online]. Available: http://jer.sagepub.com/content/12/4/353.abstract 5

[25] F. Agrell, H.-e. Ångström, B. Eriksson, J. Wikander, and J. Linderyd, "Integrated Simulation and Engine Test of Closed Loop HCCI Control by Aid of Variable Valve Timings," *SAE paper*, no. 2003-01-0748, 2003. 6

[26] F. Agrell, H. Ångström, B. Eriksson, J. Wilkander, and J. Linderyd, "Transient Control of HCCI Through Combined Intake and Exhaust Valve Actuation," *SAE paper*, no. 2003-01-3172, 2003. 6

[27] G. M. Shaver and J. C. Gerdes, "Cycle to Cycle Control of HCCI Engines," *IMECE*, no. IMECE2003-41966, 2003. 6

[28] J. Bengtsson, P. Strandh, R. Johansson, P. Tunestål, and B. Johansson, "Closed-loop combustion control of Homogeneous Charge Compression Ignition (HCCI) engine dynamics," *International Journal of Adaptive Control and Signal Processing*, vol. 18, no. 2, pp. 167–179, 2004. 6

[29] G. M. Shaver, J. C. Gerdes, and M. Roelle, "Physics-Based Closed-Loop Control of Phasing, Peak Pressure and Work Output in HCCI Engines Utilizing Variable Valve Actuation," *American Control Conf.*, 2004. 6

[30] J.-O. Olsson, P. Tunestål, and B. Johansson, "Closed-Loop Control of an HCCI Engine," *SAE paper*, no. 2001-01-1031, 2001. 6

[31] J. S. Souder, J. K. Hedrick, J. H. Mack, and R. W. Dibble, "Microphones and Knock Sensors for Feedback Control of HCCI Engines," *ICEF*, no. ICEF2004-960, 2004. 6

[32] J.-M. Kang and M. Druzhinina, "Hcci engine control strategy with external egr," in *American Control Conf.*, 30 2010-july 2 2010, pp. 3783 –3790. 6

[33] G. Shaver and J. Gerdes, "Cycle-to-cycle control of HCCI engines," *ASME International Mechanical Engineering Congress and Exposition*, no. IMECE 2003-41966, 2003. 6

[34] D. Rausen, A. Stefanopoulou, J.-M. Kang, J. Eng, and T.-W. Kuo, "A mean value model for control of HCCI engines," *J. of Dyn. Sys., Meas., and Cont.*, vol. 127, no. 3, pp. 355–362, 2005. 6

[35] D. Blom, M. Karlsson, K. Ekholm, P. Tunestål, and R. Johansson, "HCCI engine modeling and control using conservation principles," *SAE paper*, no. 2008-01-0789, 2008. 6

[36] M. Shahbakhti and C. R. Koch, "Physics Based Control Oriented Model for HCCI Combustion Timing," *J. Dyn. Syst. Meas. Control*, vol. 132, no. 2, p. 021010, 2010. 6

[37] N. Ravi, H. Liao, A. Jungkunz, C. Chang, H. Song, and J. Gerdes, "Modeling and Control of an Exhaust Recompression HCCI Engine Using Split Injection," *J. Dyn. Syst. Meas. Cont.*, vol. 134, pp. 011 016–1–12, 2012. 6, 15

[38] S. Jade, E. Hellström, A. Stefanopoulou, and L. Jiang, "On the influence of composition on the thermally-dominant recompression HCCI combustion dynamics," in *ASME Dynamic Systems and Control Conference*, 2011. 6, 7, 80, 93, 95, 114, 116

[39] S. Jade, J. Larimore, E. Hellström, L. Jiang, and A. G. Stefanopoulou, "Enabling large load transitions on multicylinder recompression HCCI engines using fuel governors," in *Proc. American Control Conference*, Washington, DC, USA, 2013, pp. 4429–4434. 6, 7, 80, 93, 95, 114, 116, 123

[40] J. Bengtsson, P. Strandh, P. Tunestål, and B. Johansson, "Model predictive control of HCCI engine dynamics," *IEEE Int. Conf. Cont. App.*, pp. 1675–1680, 2006. 6

[41] C. Chiang and C. Chen, "Constrained control of HCCI engines," *5th IEEE Conf. Indust. Elec. and App.*, 2010. 6

[42] N. Ravi, H. Liao, A. Jungkunz, A. Widd, and J. Gerdes, "Model predictive control of HCCI using variable valve actuation and fuel injection," *Cont. Eng. Prac.*, vol. 20, pp. 421–430, 2012. 6

[43] B. Allison and A. Isaksson, "Design and performance of mid-ranging controllers," *Journal of Process Control*, vol. 8, no. 5-6, pp. 469–474, Dec. 1998. [Online]. Available: http://linkinghub.elsevier.com/retrieve/pii/S0959152498000122 6, 95

[44] B. Allison and S. Ogawa, "Design and tuning of valve position controllers with industrial applications," *Trans. Inst. Meas. Control*, vol. 25, no. 1, pp. 3–16, Mar. 2003. 6, 95

[45] M. Karlsson, K. Ekholm, P. Strandh, R. Johansson, P. Tunestål, and B. Johansson, "Closed-loop control of combustion phasing in an HCCI engine using VVA and variable EGR," in *5th IFAC Symp. Advances in Auto. Contr.*, 2007. 6, 95

[46] N. Ravi, H.-H. Liao, A. F. Jungkunz, and J. C. Gerdes, "Mid-ranging control of a multi-cylinder HCCI engine using split fuel injection and valve timings," *IFAC*, 2010. 6, 95

[47] S. Jade, E. Hellström, L. Jiang, and A. Stefanopoulou, "Fuel governor augmented control of recompression HCCI combustion during large load transients," in *American Control Conf.*, 2012. 6, 7, 95

[48] P. Kapasouris, M. Athans, and G. Stein, "Design of Feedback Control Systems for Stable Plants with Saturating Actuators'," *IEEE Conf. Decision and Control*, 1988. 6

[49] ——, "Design of Feedback Control Systems for Unstable Plants with Saturating Actuators," *IFAC Symposium on Nonlinear Control System Design*, 1990. 6

[50] E. G. Gilbert and K. T. Tan, "Linear Systems with State and Control Constraints: The Theory and Application of Maximal Output Admissible Sets," *IEEE Trans. Autom. Control*, vol. 36, pp. 1008–1020, 1991. 6

[51] E. Gilbert, I. Kolmanovsky, and K. Tan, "Discrete-time reference governors and the nonlinear control of systems with state and control constraints," *Int. J. Robust Nonlin. Control*, vol. 5, pp. 487–504, 1995. 6

[52] E. G. Gilbert and I. Kolmanovsky, "Fast reference governors for systems with state and control constraints and disturbance inputs," *Int. J. Robust Nonlinear Control*, vol. 9, pp. 1117–1141, 1999. 6

[53] ——, "Set-point control of nonlinear systems with state and control constraints : a Lyapunov function reference governor approach," *Conf. Decision and Control*, pp. 2507–2512, 1999. 6

[54] E. Gilbert and I. Kolmanovsky, "Nonlinear tracking control in the presence of state and control constraints: a generalized reference governor," *Automatica*, vol. 38, no. 12, pp. 2063–2073, Dec. 2002. [Online]. Available: http://linkinghub.elsevier.com/retrieve/pii/S0005109802001358 6

[55] I. Kolmanovsky, E. Gilbert, and J. Cook, "Reference governors for supplemental torque source control in turbocharged diesel engines," in *American Control Conf.*, 1997. 6

[56] V. Tsourapas, J. Sun, and A. Stefanopoulou, "Incremental step reference governor for load conditioning of hybrid fuel cell and gas turbine power plants," *American Control Conf.*, pp. 2184–2189, Jun. 2008. 6

[57] ——, "Incremental Step Reference Governor for Load Conditioning of Hybrid Fuel Cell and Gas Turbine Power Plants," *IEEE Transactions on Control Systems Technology*, vol. 17, no. 4, pp. 756–767, Jul. 2009. [Online]. Available: http://ieeexplore.ieee.org/lpdocs/epic03/wrapper.htm?arnumber=4815395 6

[58] S. Jade, E. Hellström, J. Larimore, A. Stefanopoulou, and L. Jiang, "Reference governor for load control in a multicylinder recompression HCCI engine," *To Appear. IEEE Trans. Control Syst. Technol.*, 2013. 6, 95, 96, 98, 114, 122

[59] M. Yao, Z. Zheng, and H. Liu, "Progress and recent trends in HCCI engines," *Prog. in Ener. and Comb. Sci.*, vol. 35, no. 5, pp. 398 – 437, 2009. [Online]. Available: http://www.sciencedirect.com/science/article/pii/S0360128509000197 11

[60] M. Christensen, A. Hltqvist, and B. Johansson, "Demonstrating the multi–fuel capability of a homogeneous charge compression ignition engine with variable compression ratio," *SAE paper*, vol. 1999-01-3679, 1999. 11

[61] G. Haraldsson, P. Tunestal, B. Johansson, and J. Hyvönen, "HCCI combustion phasing in a multi–cylinder engine using variable compression ratio," *SAE paper*, vol. 2002-01-2858, 2002. 11

[62] A. Babajimopoulos, P. V. Challa, G. A. Lavoie, and D. Assanis, "Model-based Assessment of Two Variable Cam Timing Strategies for HCCI Engines: Recompression vs. Rebreathing," *ASME Internal Combustion Engine Division Spring Technical Conf.*, 2009, ICES2009-76103. 11

[63] A. Kulzer, D. Lejsek, A. Kiefer, and A. Hettinger, "Pressure trace analysis methods to analyze combustion features and cyclic variability of different gasoline combustion concepts," *SAE International*, no. 2009-01-0501, 2009. 13

[64] R. Fitzgerald, R. Steeper, J. Snyder, R. Hanson, and R. Hessel, "Determination of cycle temperature and residual gas fraction for HCCI negative valve overlap operation," *SAE Int. J. Eng.*, vol. 3, no. 2010-01-0343, pp. 124–141, April. 15, 20, 27, 35, 91

[65] C. Marriott and R. Reitz, "Experimental investigation of direct injection-gasoline for premixed compression ignited combustion phasing control," *SAE Paper*, no. 2002-01-0418, 2002. 15

[66] A. Gazis, D. Panousakis, J. Patterson, H. Chen, R. Chen, and J. Turner, "Using in-cylinder gas internal energy balance to calibrate cylinder pressure data and estimate residual gas amount in gasoline HCCI combustion," *Experimental Heat Transfer*, vol. 21, no. 4, pp. 275–280, 2008. 21, 27

[67] N. Ivansson, "Estimation of the residual gas fraction in an HCCI engine using cylinder pressure," Master's thesis, Linköping University, May 2003. 21

[68] J. Heywood, *Internal Combustion Engine Fundamentals*. McGraw-Hill Science/Engineering/Math, 1988. 22

[69] J. Chang, O. Güralp, Z. Filipi, D. Assanis, T. Kuo, P. Najt, and R. Rask, "New heat transfer correlation for an HCCI engine derived from measurements of instantaneous surface heat flux," *SAE*, vol. 1, no. 2004-01-2996, pp. 1–18, 2004. 23, 61

[70] E. Hellström, J. Larimore, J. Sterniak, L. Jiang, and A. Stefanopoulou, "Quantifying Cyclic Variability in a Multi-Cylinder HCCI Engine with High Residuals," in *Journal of Engineering for Gas Turbines and Power*, vol. 134, no. 11, 2012, p. 112803. 25, 27, 38, 70, 77, 97, 122

[71] M. Mladek and C. Onder, "A model for the estimation of inducted air mass and the residual gas fraction using cylinder pressure measurements," *SAE Int.*, no. 23000-01-0958, 2000. 27

[72] E. Ortiz-Soto, J. Vavra, and A. Babajimopoulos, "Assessment of residual mass estimation methods for cylinder pressure heat release analysis of HCCI engines with negative valve overlap," 2011, submitted to ASME Internal Combustion Engine Division Fall Technical Conference, 2011. 27

[73] M. Kulenović and G. Ladas, *Dynamics of Second Order Rational Difference Equations with Open Problems and Conjectures*. Chapman and Hall/CRC, 2002. 31, 32, 35

[74] E. Grove, G. Ladas, L. McGrath, and C. Teixeira, "Existence and behavior of solutions of a rational system," *Comm. on App. Nonlinear Analysis*, vol. 8, no. 1, pp. 1–25, 2001. 35

[75] G. Sedaghat, "Existence of solutions of certain singular difference equations," *Journal of Applied Difference Equations*, vol. 6, no. 5, pp. 535–561, 2000. 35

[76] L. Koopmans, H. Ström, and S. L. et. al, "Demonstrating a SI-HCCI-SI mode change on a Volvo 5-cylinder electronic valve control engine," in *SAE World Cong.*, 2003, 2003-01-0753. 44, 70

[77] N. Wermuth, H. Yun, and P. Najt, "Enhancing light load HCCI combustion in a direct injection gasoline engine by fuel reforming during recompression," *SAE Int. J. Engines*, vol. 2, pp. 823–836, 2009. 46

[78] H. Song, A. Padmanabhan, N. Kaahaaina, and C. Edwards, "Experimental study of recompression reaction for low-load operation in direct-injected HCCI engines with n-heptane and i-octane fuels," *Int. J. Eng. Res.*, vol. 10(4):215-229, 2009. 46

[79] M. Shahbakhti and C. Koch, "Characterizing the cyclic variability of ignition timing in a HCCI engine fueled with n-heptane/iso-octane blend fuels," *Int. J. of Eng. Res.*, vol. 9, no. 5, pp. 361–397, 2008. 46

[80] R. Wagner, K. Edwards, C. Daw, J. Green Jr., and B. Bunting, "On the nature of cyclic dispersion in spark assisted HCCI combustion," *SAE World Cong.*, vol. 2006-01-0418, 2006. 46, 52

[81] Y. Mo, "HCCI heat release rate and combustion efficiency: A coupled KIVA multi-zone modeling study," Ph.D. dissertation, University of Michigan, 2008. 50

[82] "Maximizing power output in an automotive scale multi-cylinder homogeneous charge compression ignition (HCCI) engine," in *SAE World Congr.*, 2011, sAE 2011-01-0907. 50

[83] S. Strogatz, *Nonlinear Dynamics and Chaos*. Perseus Books Publishing, LLC, 1994. 51

[84] E. Hellström, A. G. Stefanopoulou, and L. Jiang, "Reducing cyclic dispersion in autoignition combustion by controlling fuel injection timing," in *Proc. 51st IEEE Conference on Decision and Control*, Maui, HI, USA, 2012, pp. 3747–3752. 62, 64, 70, 72, 77

[85] J. Larimore, E. Hellström, S. Jade, L. Jiang, and A. G. Stefanopoulou, "Controlling combustion phasing variability with fuel injection timing in a multicylinder HCCI engine," in *Proc. American Control Conference*, Washington, DC, USA, 2013, pp. 4441–4446. 70, 97, 123

[86] T. Urushihara, K. Hiraya, A. Kakuhou, and T. Itoh, "Expansion of HCCI operating region by the combination of direct fuel injection, degative valve overlap and internal fuel reformation," *SAE World Cong.*, vol. 2003-01-0749, 2003. 70

[87] A. F. Jungkunz, H.-H. Liao, N. Ravi, and J. C. Gerdes, "Combustion phasing variation reduction for late-phasing HCCI through cycle-to-cycle pilot injection timing control," in *Proc. ASME Dyn. Sys. and Cont. Conf.*, 2011, 6091. 70

[88] N. Ravi, M. J. Roelle, H.-H. Liao, A. F. Jungkunz, C.-F. Chang, S. Park, and J. C. Gerdes, "Model-Based Control of HCCI Engines Using Exhaust Recompression," *IEEE Trans. on Cont. Sys. Tech.*, vol. 18, no. 6, pp. 1289–1302, Nov. 2010. 70

[89] A. Jungkunz, H. Liao, N. Ravi, and J. Gerdes, "Reducing combustion variation of late-phasing HCCI with cycle-to-cycle exhaust valve timing control," *IFAC Symp. on Adv. in Automotive Cont.*, 2010. 70

[90] E. Hellström, J. Larimore, S. Jade, A. Stefanopoulou, and L. Jiang, "Reducing cyclic variability while regulating combustion phasing in a 4-cylinder hcci engine," *To Appear. IEEE Trans. Control Syst. Technol.*, 2013. 71, 97, 122

[91] E. Ott, C. Grebogi, and Yorke, "Controlling chaos," *Phys. Rev. Lett.*, vol. 64, no. 11, pp. 1196–1200, 1990. 71

[92] E. Hellström, A. Stefanopoulou, and L. Jiang, "Cyclic variability and dynamical instabilities in autoignition engines with high residuals," *IEEE Transactions on Control System Technology*, vol. 21, no. 5, pp. 1527–1536, 2013. 71

[93] C. Finney, J. Green, Jr., and C. Daw, "Symbolic time-series analysis of engine combustion measurements," *SAE Tech. Paper*, no. 980624, 1998. 77

[94] C. Nesbit and J. Hedrick, "Adaptive engine control," in *American Control Conference, 1991*, 1991, pp. 2072–2076. 80

[95] H. Inagaki, A. Ohata, and T. Inoue, "An adaptive fuel injection control with internal model in automotive engines," in *Industrial Electronics Society, 1990. IECON '90., 16th Annual Conference of IEEE*, 1990, pp. 78–83 vol.1. 80

[96] K. Muske, J. Jones, and E. M. Franceschi, "Adaptive analytical model-based control for si engine air–fuel ratio," *Control Systems Technology, IEEE Transactions on*, vol. 16, no. 4, pp. 763–768, 2008. 80

[97] H. Tang, L. Weng, Z.-Y. Dong, and R. Yan, "Adaptive and learning control for si engine model with uncertainties," *Mechatronics, IEEE/ASME Transactions on*, vol. 14, no. 1, pp. 93–104, 2009. 80

[98] R. Turin and H. Geering, "Model-reference adaptive a/f-ratio control in an si engine based on kalman-filtering techniques," in *American Control Conference, Proceedings of the 1995*, vol. 6, 1995, pp. 4082–4090 vol.6. 80

[99] J. Xiaohong and S. Tielong, "Lyapunov-design of adaptive air-fuel ratio control for gasoline engines based on mean-value model," in *Control Conference (CCC), 2011 30th Chinese*, 2011, pp. 6146–6150. 80

[100] S. Sugihira and H. Ohmori, "Model based starting control of si engines via adaptive feedback linearization," in *SICE Annual Conference, 2008*, 2008, pp. 842–847. 80

[101] A. M. Frith, C. R. Gent, and A. J. Beaumont, "Adaptive control of gasoline engine air-fuel ratio using artificial neural networks," in *Artificial Neural Networks, 1995., Fourth International Conference on*, 1995, pp. 274–278. 80

[102] C.-J. Chiang, C.-C. Chou, and J.-H. Lin, "Adaptive control of homogeneous charge compression ignition (hcci) engines," in *American Control Conference (ACC), 2012*, 2012, pp. 2066–2071. 80

[103] G. Goodwin and K. Sin, *Adaptive Filtering Prediction and Control*. Prentice-Hall Inf. and Sys. Sci. Ser., 1984. 84

[104] P. Ioannou and J. Sun, *Robust Adaptive Control*. Prentice Hall Englewood Cliffs, NJ, 1996. 84

[105] M. Voicu, *Advances in Automatic Control*. The Kluwer International Series in Engineering and Computer Science, 2004. 102

[106] J. Dec, "A computational study of the effects of low fuel loading," *SAE Paper*, no. 2002-01-1309, 2002. 111

[107] S. Jade, J. Larimore, E. Hellström, L. Jiang, and A. Stefanopoulou, "Controlled Load and Speed Transitions in a Multi-Cylinder Recompression HCCI Engine," *IEEE Transactions on Control Systems Technology*, 2013, submitted for review. 122

[108] J. Larimore, S. Jade, E. Hellström, A. G. Stefanopoulou, and L. Jiang, "Adaptive Control of a Recompression 4-Cylinder HCCI Engine," *IEEE Transactions on Control Systems Technology*, 2013, submitted for review. 122

[109] J. Larimore, S. Jade, E. Hellström, A. G. Stefanopoulou, J. Vanier, and L. Jiang, "Online adaptive residual mass estimation in a multicylinder recompression HCCI engine," in *Proc. ASME Dynamic Systems and Control Conference*, Palo Alto, CA, USA, 2013. 123

[110] E. Hellstrom, J. Larimore, L. Jiang, , and A. Stefanopoulou, "Predictive modeling and reducing cyclic variability in autoignition engines," 2013, Application filed, Patent App. No.: 13/624539. 123

[111] ——, "Dynamic estimator for determining operating condition in an internal combustion engine," 2013, Application filed, Patent App. No.: 13/621527. 123

[112] J. Larimore, S. Jade, L. Jiang, E. Hellstrom, A. Stefanopoulou, and J. Vanier, "Device and method for real-time residual gas estimation," 2013, Application filed, Patent App. No.: 61/766754. 123